Mechanics of Marginal Solids

Length, Strain, and Time Scales

Mechanics of Marginal Solids

Length, Strain, and Time Scales

Proefschrift

door

Karsten BAUMGARTEN

Master of Science in Physics,
Georg-August-Universität, Göttingen, Duitsland,
geboren te Einbeck, Duitsland.

Dit proefschrift is goedgekeurd door de

promotor: prof. dr. ir. T.J.H. Vlugt
copromotor: dr. B.P. Tighe

Samenstelling promotiecommissie:

Rector Magnificus,	voorzitter
Prof.dr.ir. T.J.H. Vlugt,	Technische Universiteit Delft
Dr. B.P. Tighe,	Technische Universiteit Delft

Onafhankelijke leden:

Dr. L. Rossi,	Technische Universiteit Delft
Dr. E. Lerner,	Universiteit van Amsterdam
Prof.dr.ir J.T. Padding,	Technische Universiteit Delft
Prof.dr.ir M.T. Kreutzer,	Technische Universiteit Delft
Prof.dr.ir C. Storm,	Technische Universiteit Eindhoven

An electronic version of this dissertation is available at
`http://repository.tudelft.nl/`.

For my parents

Contents

Summary

Network materials, foams, and emulsions are ubiquitous in our daily life. We have a good intuition about how they respond as we handle them, but our theoretical understanding is poor. One of their most interesting features is that they are unusually fragile and appear to switch between solid and liquid state seamlessly.

In fact, foams and emulsions undergo a non-equilibrium phase transition as their packing fraction increases - this is the jamming transition. Networks show a similar transition as their connectivity increases, where the matrial switches from floppy to rigid.

The fact that these materials undergo a phase transition, opens up the theoretical toolset of statistical mechanics. An important part of current research is therefore dedicated to finding diverging length and time scales and investigating the critical behavior of the systems in detail.

Because the systems in question are highly disordered, analytical modelling is challenging. At the same time there are significant experimental obstacles to approaching the critical point closely. For this reason, the development of simulation software plays an important role - all data presented in this thesis is generated through simulations. As the subtitle of this dissertation suggests, our findings concern length, strain, and time scales.

In Chapter 3 the linear response of foams and emulsions on various length scales is probed. Classical continuum mechanics is a long wavelength theory - it is a local theory. This means that in order to determine strain at a certain position x, it is sufficient to know the stress at the same position. A method is introduced which enables to directly measure the moduli on different length scales. The simulations show that the linear response of soft sphere packings close to jamming becomes increasingly nonlocal. Using the results a so-called nonlocal length scale is introduced, which diverges at the transition. Additionally, a strain-stress-relation is derived, which gives improved predictions of the linear response to a spatially varying stress field.

Chapter 4 and 5 consider the nonlinear behavior of networks below and above their critical connectivity.

Chapter 4 shows that sub-critical networks can be rigidified by a pre-stress, and that the shear response has surprising similarities to networks with bending interactions. In addition to shear response, the density of states is measured. Variational arguments can explain its form, and show how the density of states can be used to predict the response to shear. This theoretical approach is quite general, suggesting that other systems

could be described with the same methods. An example for such a system could be a soft sphere packing which consists of a mixture of soft and hard particles.

Chapter 5 considers networks above their critical connectivity. In general, when a shear strain is applied to a system it shows a build-up of normal stresses. Equivalently, it contracts/expands as a shear stress is applied. This nonlinear effect is called the Poynting effect. Two network structures are tested for this effect, and both systems are found to feature a negative sign in the effect (systems build-up negative normal stresses/contract when sheared). Furthermore, the results show that the amplitude of the effect scales differently in both networks.

A theoretical framework is developed which explains the sign and the amplitude. This framework relates these two quantities to the properties of the linear response to shear stress. Finally, the Poynting effect is related to the shear stiffening behavior of the networks.

Chapter 6 shows that the linear viscoelastic response of foams and emulsions depends strongly on the details of the force law of the viscous interaction. Soft sphere packings, in which transverse relative motion is not damped, do not show critical behavior. Only if both tangential and normal relative motion is damped, one captures the essential physics of soft sphere packings close to jamming. The widely used Stokes drag model also correctly captures the shear response of the packings, but still has qualitative influence on the two point correlation function of the linear response.

Samenvatting

Netwerkmaterialen, schuimen en emulsies zijn alom aanwezig in ons dagelijks leven. Wanneer we deze materialen gebruiken hebben we intuïtief een gevoel hoe ze zullen reageren op hun gebruik, maar ons theoretisch begrip hiervan is beperkt. Één van de belangrijkste kenmerken is dat deze materialen ongewoon kwetsbaar zijn en naadloos lijken te veranderen van een vaste naar een vloeibare toestand.

Schuim en emulsies ondergaan een uit-evenwicht faseovergang bij toenemende pakkingsfractie. Dit wordt de jamming overgang genoemd. Netwerken laten een vergelijkbare transitie zien als hun coördinatiegetal toeneemt – waar netwerken veranderen van slap naar stijf.

Het feit dat deze materialen een faseovergang laten zien betekent dat statistische mechanica gebruikt kan worden. Een belangrijk deel van het huidige onderzoek is daarom toegewijd aan het vinden van divergerende lengte- en tijdschalen en het in detail onderzoeken van het kritische gedrag van deze systemen.

Omdat de onderzochte systemen sterk ongeordend zijn is het een uitdaging om deze systemen analytisch te modelleren. Tevens zijn er grote experimentele obstakels om het kritieke punt te benaderen. Daarom speelt het ontwikkelen van simulatie software een belangrijke rol – alle data gepresenteerd in dit proefschrift is gegenereerd door middel van computer simulaties. Zoals de ondertitel van dit proefschrift suggereert, betreffen de in dit proefschrift beschreven resultaten lengte-, vervormings- en tijdschalen.

Hoofdstuk 3 onderzoekt de lineaire reactie op een ruimtelijk variërend spanningsveld van schuimen en emulsies voor verscheidene lengte schalen. Klassieke continuummechanica is een lange golflengte theorie, anders gezegd het is een lokale theorie. Dit betekent dat voor het bepalen van de vervorming op een zekere positie x in het materiaal, het voldoende is als de mechanische spanning op deze positie bekend is. Een methode wordt geintroduceerd om direct de modulus van verschillende lengteschalen te bepalen. De simulaties laten zien dat de lineaire reactie van de zachte bolpakkingen dichtbij het jamming punt steeds meer niet-lokaal wordt. Door de resultaten is het mogelijk om een zogenaamde niet-lokale lengteschaal te definieren, welke divergeert bij de jamming overgang. Gebruikmakend van de simulaties wordt een vervorming-spanningsrelatie voorgesteld die betere voorspellingen geeft voor lineaire reacties op een ruimtelijk variërend spanningsveld.

Hoofdstuk 4 en 5 betreffen het niet-lineaire gedrag van netwerken onder en boven hun kritische coördinatiegetal.

Hoofdstuk 4 laat zien dat sub-kritische netwerken verstijfd kunnen worden door een voorspanning en dat hun afschuifreactie verrassende overeenkomsten heeft met netwerken met buigingsinteractie. Naast de afschuifreactie, wordt ook de toestandsdichtheid bepaald. Met hulp van argumenten gebaseerd op het variatieprincipe, wordt de vorm verklaard en wordt laten gezien hoe de toestandsdichtheid gebruikt kan worden voor het voorspellen van de afschuifreactie. Onze theoretische aanpak is redelijk algemeen, hetgeen suggereert dat andere systemen mogelijk beschreven kunnen worden met dezelfde methoden. Een voorbeeld voor zo een systeem is een bolpakking die bestaat uit zachte en harde partikelen.

Hoofdstuk 5 behandelt netwerken boven hun kritische coördinatiegetal. Wanneer een systeem word blootgesteld aan een schuifvervorming laat deze normaliter een opbouw van normaalspanningen zien. Deze zal samentrekken/uitzetten als er een schuifspanning wordt aangebracht. Dit non-lineaire effect wordt het Poynting effect genoemd en wordt in twee netwerkstructuren onderzocht. De twee systemen laten zien dat het teken van dit effect negatief is (systemen bouwen negatieve normaalspanningen op/trekken zich samen wanneer er afschuiving plaatsvind). Daarnaast wordt gevonden dat de amplitude van het effect verschillend schaalt voor beide netwerken.

Een theoretisch kader wordt ontwikkeld die het teken en amplitude verklaart door deze te verbinden met de eigenschappen van de lineaire reactie op een afschuiving. Uiteindelijk wordt het Poynting effect gerelateerd aan het afschuif verstijvend gedrag van netwerken.

Hoofdstuk 6 laat zien dat de lineaire viscoelastische reactie van schuimen en emulsies sterk afhankelijk is van de details van de in het model gebruikte dempingswet. De resultaten laten zien dat zachte bolpakkingen waarin transversale relatieve bewegingen niet worden gedempt, geen kritisch gedrag laten zien. Alleen wanneer tangentiële en normale relatieve bewegingen worden gedempt is het mogelijk de essentiële fysica van zachte bolpakkingen dichtbij het jamming punt te beschrijven. Het veelgebruikte Stokes drag model beschrijft ook de afschuifreactie van pakkingen, maar heeft nog steeds invloed op de two point correlation function van de lineaire reactie.

1

Introduction

1

When we are doing the dishes, shaving, eating mayonnaise or drinking beer or cappuccino, it is natural for us to come in contact with foams and emulsions in our every day life. In fact, we are quite used to handling them and have a good intuition on how they react as we handle them. However, often we do not appreciate that we have poor theoretical understanding of them. For instance, is a foam a gas, a liquid, or a solid? Shaving foam is made of gas and a small fraction of liquid but that does not bring us anywhere closer to an answer. In fact the answer depends on the situation in which the foam is considered. While we apply shaving foam to our skin it behaves like a liquid. However, as soon as we stop applying a force with our hands it ceases to flow and keeps its shape. Gravity is not enough to make it flow. It behaves like a solid. Another situation in which both liquid and solid behavior are found, occurs while doing the dishes. The foam flows as long as it is mixed with enough water, but as the foam sits in the sink for a while it will become drier and also forms a solid.

Similar behavior also occurs in other materials. Sand flows through our hands like liquid, but at the same time it forms piles on a surface and acts like a solid. Ketchup is stuck in its bottle but as we shake it, the ketchup flows out rapidly leaving us with far more than we actually wanted. In some materials we can use the sudden change between solid and liquid to our advantage. If one wants to paint a wall it is handy if the paint flows nicely so that it is easy to distribute, but it should act like a solid when we stop painting, because it should stay on the wall where we left it.

Most of what we know about systems like shaving foam, sand, paint, or mayonnaise is from experience and phenomenological considerations. We lack a deep theoretical and predictive understanding comparable to our knowledge of crystals. Such a deep understanding would be useful, because soft amorphous materials are not only ubiquitous in our daily life but also in industry. It would be of great help to predict whether sand will easily flow through a hopper or will get stuck regularily. When extinguishing a fire the foam needs to flow out of the hose easily but needs to become solid when it hits a surface. Typically materials and their transport processes are designed only through trial and error. A more theoretical understanding would simplify the design.

The examples above are reminiscent of melting and freezing and are in fact considered to be a phase transition - the jamming transition. However the jamming transition takes place in systems which are not in thermodynamic equilibrium so it has important properties which distinguishes it from a classical equilibrium phase transition. We will comment on these differences in the next section.

A similar non-equilibrium phase transition can be found in network materials. When the nodes in a network are highly connected the network behaves like a solid while it can be deformed without energy cost when the connectivity is low. Networks can be found in biological cells and materials like wood and rubber have network structures. Furthermore, the structure

liquid-like   marginal   solid-like

ϕ_c

jamming   rigidity loss
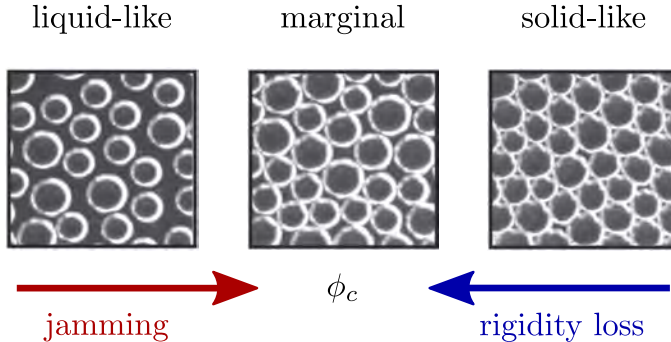
Figure 1.1: Top view on two dimensional foams [1]. The three panels show a foam above (right), below (left), and at the jamming transition.

of the contact network in foams and emulsions is of theoretical interest because its linear response is similar to linear response in jammed systems. Additionally, it is a model that can be used to investigate the response of solid foams where the contact network does not change even when applied stresses are high.

1.1. *The Jamming Transition*

Figure 1.1 shows the top view of a quasi two-dimensional foam made of two and three millimeter bubbles. It is constrained from below by a liquid and trapped underneath a glass plate [1]. As the packing fraction ϕ of air bubbles in the water is low, the water dominates the response to external forces - the foam flows like a liquid. The bubbles are mechanically in a vacuum state. If the foam contains a high fraction of air the bubbles are pressed together and form a rigid network. This network can resist a deformation - the foam behaves like an elastic solid. In between the two states at a packing fraction of $\phi_c \approx 0.84$ in two dimensions and $\phi \approx 0.64$ [2] in three dimensions, there are configurations in which the bubbles just touch but do not exert a force on each other. This marginal state marks the jamming transition.

Through an external pressure the particles in a system are jammed together and become stuck in a local energy minimum. Because the particles are large enough so that thermal effects can be neglected [3], they are not able to explore the phase space and find the global minimum of the energy landscape. For that reason systems that undergo a jamming transition are not in thermodynamic equilibrium. In this sense the jamming transition is a non-equilibrium phase transition of second order and the full toolkit of statistical mechanics cannot be applied. Nevertheless, it turns out that many features of the phase transition resemble an equilibrium phase transition. Therefore, some of the theoretical tools used in equilibrium phase

1
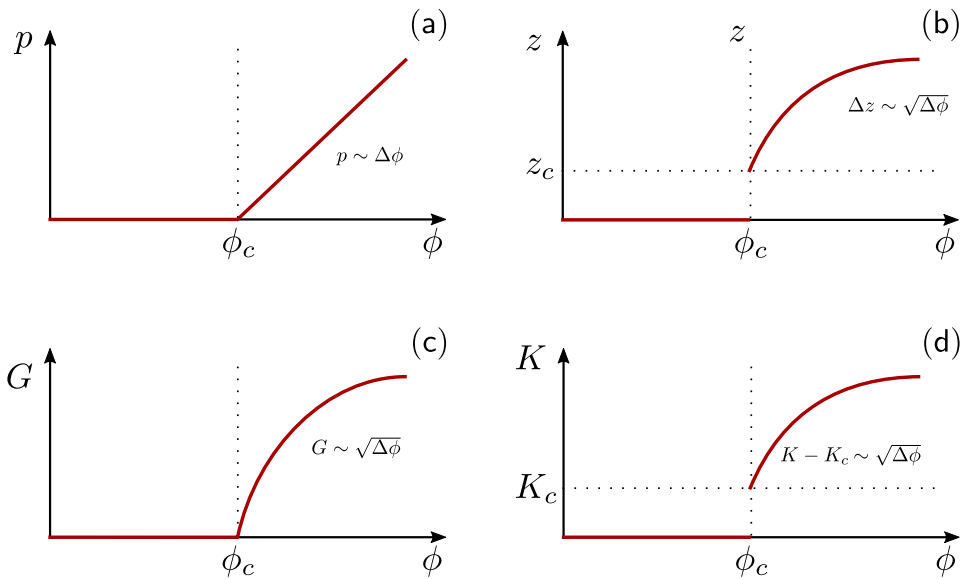
Figure 1.2: (a) The scaling of the mechanical pressure p. It vanishes continuously at the transition. (b) The average number of contacts per particle z jumps to $z_c = 4$. One finds a similar situation for the shear G and bulk modulus K. While the shear modulus vanishes continuously the bulk modulus shows a jump.

transitions can also be used to analyze the properties of systems close to the jamming transition [3, 4].

One of those theoretical tools is the idea of universality. As the "distance" to the critical point becomes smaller - here measured for example in terms of the excess packing fraction $\Delta\phi = \phi - \phi_c$ - the material property A scales with this distance

$$A \sim \Delta\phi^{\alpha} \tag{1.1}$$

with some exponent α. Furthermore, the dependence of the order parameter on details of the system like interaction potential vanishes. The critical point is then described by a set of critical exponents. It has been found that a great variety of systems often share the same set of exponents. All these systems are considered to be part of the same universality class.

In general the scaling exponents are also a function of the dimension of the system, however, any phase transition becomes more mean field-like in higher dimensions until the scaling exponents cease to change. This so called "upper critical dimension" was argued and numerically found to be 2 in jammed systems [5, 6]. One can therefore run simulations in 2 dimensions and make quantitative predictions for scaling exponents in higher dimensions.

The value of ϕ_c is not sharp in finite systems. Each realisation has a unique value which fluctuates around the value given above [3]. For that
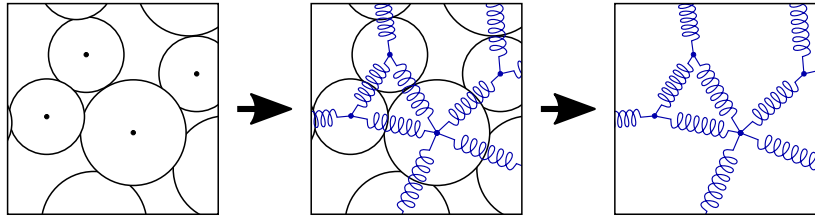
Figure 1.3: A soft sphere packing is turned into a network. The center of each disk is turned into a node and the contacts into springs.

reason, it is easier to use the mechanical pressure p or the average number of contacts per particle z as order parameters because the transition point is sharp for these two properties of the system. These two quantities and numerous other quantities [3, 7, 8] like moduli, length scales [9–12] and time scales [3, 13] scale with $\Delta\phi$ like stated above .

The scaling of p and z with $\Delta\phi$ are shown in Figure 1.2a and 1.2b, respectively. The mechanical pressure is zero below the ϕ_c and increases linearly afterwards. The contact number z jumps to a critical value z_c at the transition. In two dimensions this critical value is $z_c = 4$ and in three dimensions it is $z_c = 6$. Due to the jump it is common to define the access contact number $\Delta z = z - z_c$ which scales with the square root of $\Delta\phi$. Using Δz as an order parameter is especially helpful in networks where the packing fraction is not defined.

To determine whether a system is jammed or unjammed one can use the shear or bulk modulus. If the packing fraction is $\phi < \phi_c$ both moduli are zero. At the jamming transition the shear modulus still remains zero but it starts to increase with the square root of $\Delta\phi$ (see Figure 1.2c). The behavior of the bulk modulus is similar to the connectivity - it has a finite jump [14] and then increases with $\Delta\phi^{0.5}$ (see Figure 1.2d). If one measures a finite bulk and shear modulus the system is jammed while it is unjammed when both vanish.

1.2. *Isostaticity and the Coordination Number*

To get a better understanding why an average number of four contacts per particle is necessary for a soft sphere packing to become solid it is helpful to think of the system as a network. Figure 1.3 depicts how the packing is mapped onto a network. The centers of the disks become the nodes of the network while each contact is turned into a spring. While the resulting network itself is used as a model, this section uses it to go into more detail concerning the jamming transition. The section explains the threshold of z_c and describes the response of a floppy network to an external force.

The average number of contacts per particle, or coordination number, z jumps at the jamming transition to a critical value. This value can be

1
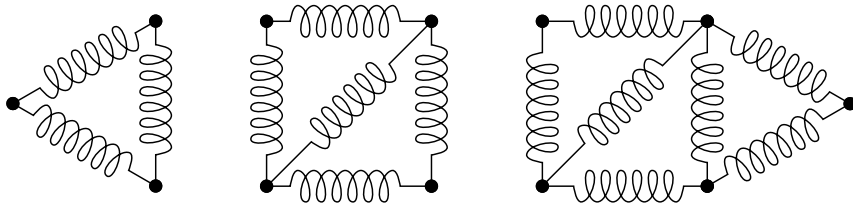
Figure 1.4: Networks with 3,4, and 5 nodes which have just enough contacts to become rigid

understood following arguments from Maxwell [15].

If a system is rigid it means that no particles are able to move without energy cost - so all motion in the system is constrained. Such constraints are contacts between particles because motion that stretches or compresses springs changes the potential energy in the system. See Figure 1.4 for a depiction of the problem. For a simple system just containing $N = 3$ particles in $D = 2$ dimensions there are DN degrees of freedom. However, there are also $D(D+1)/2$ solid body translations/rotations which do not cost energy - translations in D spatial directions and $D(D-1)/2$ rotations. The remaining three degrees of freedom, which consist of relative motions between the particles that do not shift the center of mass, are constrained by three springs. The same arguments do not change for the larger systems also depicted in Figure 1.4. As there are N particles in D dimensions there are $DN - D(D+1)/2$ degrees of freedom that each have to be constrained by one contact in order to obtain a rigid network. If the coordination number of a packing is z there are $Nz/2$ contacts which means that a coordination number of

$$z > z_c = 2D - \frac{D(D+1)}{N} \approx 2D \quad \text{if } N \text{ is large} \tag{1.2}$$

is necessary for a packing to be rigid. In general z_c also depends on whether there are other degrees of freedom. For instance, if the box containing the system is not fixed, there can be shear or expansion/compression degrees of freedom [16]. However the fraction of extra degrees of freedom, which are not associated with particles, vanishes in case of large systems such that the critical coordination number approaches $z = 2D$. Above this critical coordination number any deformation applied costs energy because purely
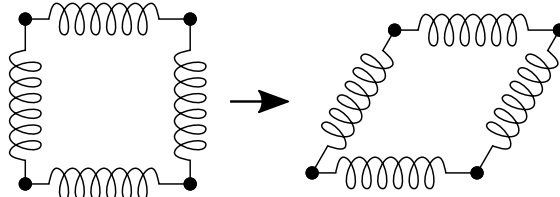
Figure 1.5: Underconstrained network which can move without energy cost
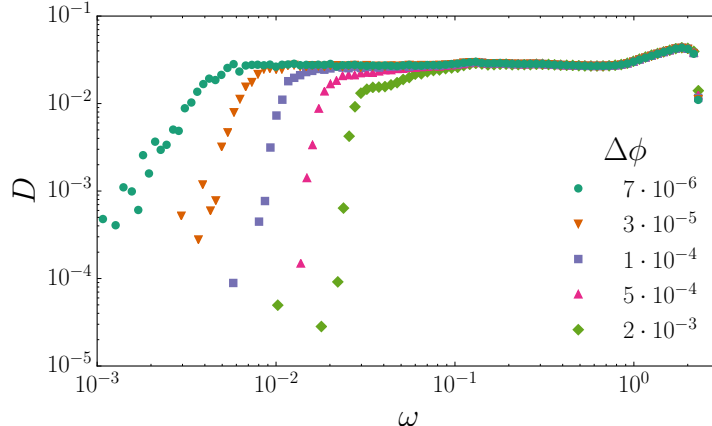
Figure 1.6: The density of states for a foam as depicted in 1.1. The curve has a plateau and a crossover at a characteristic frequency ω^*. This frequency scales with the distance to the jamming transition.

tangential motion is not possible - the system is a solid. A system that has an average coordination number of exactly $z = z_c$ is at the isostatic point.

Note that the Maxwell stability criterion mentioned above is more restrictive than what one would assume from considering only one particle locally. To keep a particle locally stable $D+1$ contacts are necessary if there is no friction. If a particle has less contacts it is considered to be a "rattler". These particles do not participate in linear response of the system.

If a system is underconstrained the particles can move without energy cost. A simple example is shown in 1.5. The nodes of the network move without changing the length of any springs. That means that the relative motion between particles, which are in contact, has to be perpendicular to the direction of the contact. A rearrangement that fulfills this requirement is a floppy mode.

In a solid there are no floppy modes that couple to compression or shear. (The meaning of "coupling" will be made precise in Chapter 2.) However, as the following section will show, they are still important to understand the linear response of "marginal" systems which are close to isostaticity yet still solid.

1.3. *The Density of States*

The density of states $\mathcal{D}(E)$ gives the number of states within a certain energy interval $[E, E + \Delta E]$ and is frequently used in solid state physics [17]. In the jamming community the density of states is also refered to as the density of vibrational states $\mathcal{D}(\omega)$. It gives the number of eigenmodes with an eigenfrequency within an interval $[\omega, \omega + \Delta\omega]$. The density of states can
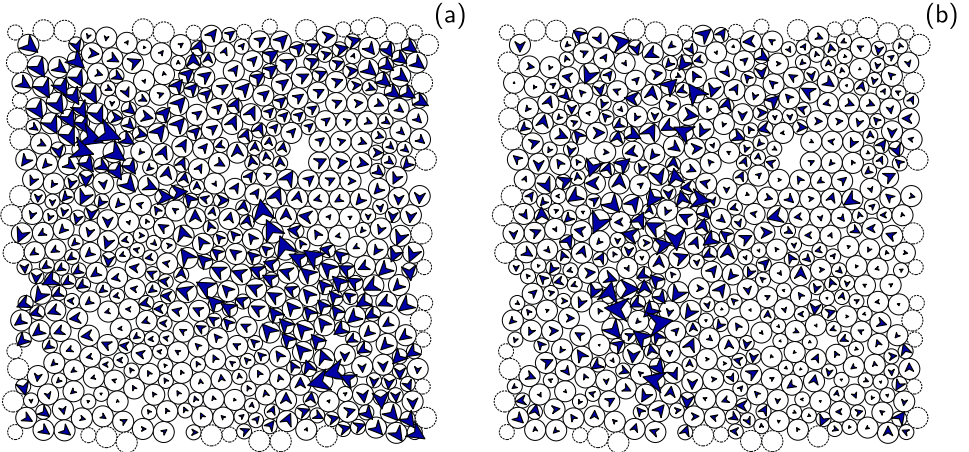
Figure 1.7: Two normal modes of a soft sphere packing with 512 discs. Dashed circles indicate particles which appear due to periodic boundary conditions. The size of the arrows indicates the amplitude of the displacements. The normal mode in (a) has low eigenfrequency and in (b) high eigenfrequency.

be calculated by linearizing the equation of motion (see Chapter 2).

An important feature of the disordered systems in this thesis is an anomalous behavior in the density of states [3]. Figure 1.6 shows that $\mathcal{D}$ is constant for several orders of magnitude in the frequency ω. For low ω it has a crossover. This crossover depends on the distance to the jamming point. It defines a time scale $\tau^* = 1/\omega^* \sim \Delta\phi^{-0.5}$ which diverges at the transition.

In a crystal the density of states looks different. Here one finds that for low frequencies $\mathcal{D} \sim \omega^{D-1}$. That means that disordered systems like foams and emulsions - close to the jamming transition - have an excess of low frequency modes. Why are they present in disordered solids but not crystals?

The answer lies in the linear response of networks below isostaticity. In [10] the authors use variational arguments to approximate the energy and the number of eigen modes of an isostatic system. The idea is to cut contacts in an isostatic network of size $L \times L$ along a line spanning the system. After the cutting, there is a number of floppy modes n_f proportional to the length of that line L. Based on these floppy modes the authors construct $n_f \sim L$ trial modes which have eigenfrequencies $\omega \sim 1/L$. According to the variational principle that means that there are $n_f/2$ normal modes with a frequency lower than $\sqrt{2}/L$. Since the number of such normal modes in a crystal is of order one and therefore significantly lower, one understands the abundance of low energy modes in amorphous solids.

The cutting method to construct trial modes has recently been questioned by simulations [18]. The trial modes only show motion localized at

the cutting line and do not penetrate into the bulk which was an assumption that was made in [10]. However, recently in [19] a new way to construct trial modes was introduced.

The previous section introduced floppy modes that only consist of tangential relative motion between particles. For a marginal system close to the isostatic point this characteristic of the response still persists. Even though there has to be relative normal motion which costs energy and causes finite shear and bulk moduli, relative transverse motion still dominates the response. The low frequency modes therefore consists mostly of sliding motion (see Figure 1.7a). Sliding has a low energy cost compared to parallel motion which leads to low frequencies in $\mathcal{D}$. For comparison, Figure 1.7b shows a normal mode with high frequency. The displacements are spatially less correlated and involve more relative normal motion. See [20] or Chapter 6 for a scaling plot of relative tangential and normal motion.

1.4. *This Thesis*

This thesis considers soft sphere packings and networks which are derived from it. However, soft sphere packings in which the contact network can change are only considered in the linear regime, where such changes, by construction, cannot occur (see Chapter 2). Strictly speaking that means that this thesis is about the networks derived from soft sphere packings. We also consider variations of these networks [14, 21, 22] and fibre networks [23–25]. In all chapters the starting point is a packing/network close to z_c. We then investigate one of the following aspects.

Nonlocal Elasticity: In Chapter 3 we consider nonlocal effects in the linear response of soft sphere packings close to jamming. Classical continuum theory is a long wave length approximation where only the strain at a position x influences the stress at the same position x. We show that this approximation is not sufficient for systems which are close to the jamming transition. We directly measure the Fourier transform of a modulus of uniaxial compression and the shear modulus. According to local theory these measurements should yield a constant function. However, our results show that the linear response of soft sphere packings is nonlocal.

Hypostatic Networks: In Chapter 4 we investigate the behavior of hypostatic networks. While these networks are floppy according to Maxwell counting they can be regidified by a "perturbing field". Examples for such a field are bending interactions or a pre-stress on the network. We investigate how the perturbing field influences the density of states and the shear modulus of hypostatic networks. We develop a mean field like description and show that perturbing fields of different nature can have similar effect on the shear modulus.

1

Nonlinear Elasticity: In Chapter 5 we investigate the so called "Poynting effect" which is a nonlinear effect in which a system builds up normal stresses as a response to an applied shear strain. We develop a microscopic theory that describes the amplitude and sign of the effect. In a last step we also connect the Poynting effect to the shear stiffening behavior which is found in the networks.

Viscoelasticity: In Chapter 6 we calculate the dynamical shear modulus $G^*(\omega)$. We test different models for viscous damping. We investigate contact damping in which only the relative normal motion of particles is considered while relative transverse motion is not damped. This damping law is often used because it does not apply an angular momentum to the particles which simplifies the simulations because rotational degrees of freedom can be omitted. However, we find that systems with only normal damping do not show critical scaling close to jamming. As a numerically cheap alternative to contact damping we test Stokes drag. However, while Stokes drag does not influence the shape of G^* it has qualitative influence on the two-point correlation function of the linear response.

2

Numerical Methods

The algorithms which are used in this thesis are primarily concerned with applying homogeneous deformations to systems. While we use the Hessian matrix to apply deformations in the linear regime, we implement FIRE (Fast Inertial Relaxation Engine) to apply quasistatic nonlinear deformations. However, the FIRE algorithm is also used to generate soft sphere packings.

This chapter explains the algorithms and gives details about how they are implemented.
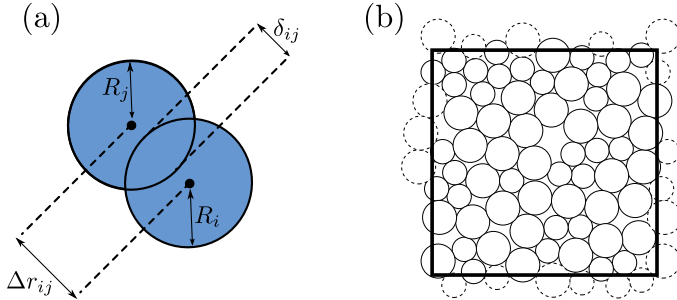
Figure 2.1: (a) Two soft disks overlapping. They have radii R_i, R_j, and distance r_{ij}. The force they exert on each other is proportional to the overlap δ_{ij}. (b) Soft sphere packing in a potential energy minimum. The dashed particles indicate interactions due to periodic boundary conditions.
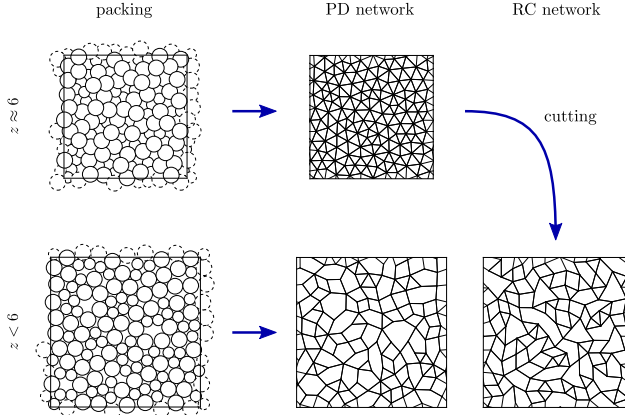
2.1. *Model and Notation*

Notation: A vector $\boldsymbol{x}_i$ which denotes any quantity refererring to an individual particle (e.g. positions, displacements, velocities, ...) is written in bold. The elements of these vectors are $x_{i\alpha}$ where Greek indices refer to Cartesian coordinates and Latin letters indicate the index of the particle. If such a vector has two Latin indices it denotes relative quantities between two particles. A vector that characterizes the state of the whole system is written in bra-ket notation $|\boldsymbol{x}\rangle \coloneqq |\boldsymbol{x}_1, \boldsymbol{x}_2, \boldsymbol{x}_3, ..., \boldsymbol{x}_N\rangle$. In some cases degrees of freedom of the simulation cell are also included. In that case the cell degrees of freedom are explicitly mentioned in the state vector $|\boldsymbol{x}, \boldsymbol{\gamma}\rangle$. Matrices $\hat{M}$ are indicated by a hat. In case of a unit vector $\hat{\boldsymbol{n}}$ we also use a hat.

Soft sphere packings: We consider systems in two spatial dimensions D which consist of N particles. The rectangular systems have volume V, edges L_x and L_y, with periodic boundary conditions in both the x and y direction (as indicated by dashed particles in figure 2.1b). The particles are disks, half of which have radius r and the other half $1.4r$ to prevent them from crystallizing. Two disks only interact if they overlap (see figure 2.1a). The force that they then exert on each other is

$$\boldsymbol{f}_{ij} = \begin{cases} -k\delta_{ij}\dfrac{\boldsymbol{r}_{ij}}{r_{ij}} & \text{if} \quad \delta_{ij} > 0 \\ \boldsymbol{0} & \text{otherwise} \end{cases} \tag{2.1}$$

where the vector $\boldsymbol{r}_{ij} = \boldsymbol{r}_j - \boldsymbol{r}_i$ points from the center of particle i to the center of particle j and the overlap δ_{ij} is given by the difference between their distance and the sum of their radii $\delta_{ij} = R_i + R_j - r_{ij}$. The interaction is a one-sided harmonic spring with rest length $R_i + R_j$ and spring constant k. Results are reported in units which are constructed from the spring constant and the diameter of the smaller particles.

Figure 2.2: Creation protocol of PD and RC networks. PD networks with connectivity z are created from a packing with the same connectivity. An RC network is created from a highly connected packing and a desired contact number is reached by randomly cutting springs.

The process of numerically creating a soft sphere packing is started by placing the disks in the simulation cell with their coordinates $x \in [0, L_x)$ and $y \in [0, L_y)$ drawn from a uniform probability distribution. The next step is to use the energy minimization algorithm FIRE (Fast Inertial Relaxation Engine [26], see Section $2.7.1$) to minimize the potential energy of the system at fixed volume and shape

$$U = \frac{1}{2}k \sum_i \sum_{\langle ij \rangle} \delta_{ij}^2 \tag{2.2}$$

where $\langle ij \rangle$ denotes all the particles j which are in contact with particle i. The result of such an energy minimization is shown in figure 2.1b. Especially for low packing fractions it often happens that so called "rattlers" are present in the system. These particles have no contacts and are therefore not part of the network that spans the simulation box. They do not influence the linear response of the system and are ignored during linear response calculations.

The equilibrated condition of soft sphere packings is in general under stress - all elements of the stress tensor $\hat{\sigma}_0$ are non-zero. Stress in the initial condition is called pre-stress.

The dynamics are overdamped which means that there is no inertia in the system - all masses are set to zero. In Chapters 3, 4, and 5 the dynamics are quasistatic, corresponding to vanishingly slow deformation rates. In Chapter 6 we consider finite rate deformations in the overdamped limit. Details of the overdamped dynamics are discussed in Section 2.6 and Chapter 6.

Elastic spring networks: There are two types of random spring networks which are considered throughout this thesis.

2

First, there are packing-derived (PD) networks, which are created starting from a soft sphere packing. To create a PD network with a certain connectivity z the particle centers in a packing with the desired connectivity are replaced with nodes. The contacts are turned into springs with their rest length set to the separation of the particle centers in the equilibrated configuration.

The second type of networks are randomly cut (RC) networks, which are created starting from a highly connected packing with $z \approx 6$ (see figure 2.2). After turning this packing into a packing derived network a connectivity $z < 6$ is reached by cutting springs. We use a cutting protocol which cuts springs belonging to highly connected nodes first [21].

2.2. *Linear Response - The Hessian Matrix*

The linear response in a packing of soft spheres consists of two regimes: the strictly linear regime and the weak linear response regime. In the strictly linear regime the contact network stays unchanged and the weak linear response regime follows after the first contact change has occured. The stress-strain curve of a single system has a kink or jumps at this point, but if an ensemble is considered the relation between stress and strain (see Section 2.3) remain linear long after the first contact change. The strain that can be applied until the first contact change occurs vanishes for inifinitely large systems [27]. However, the extent of the weak linear response regime depends on the confining pressure p but not on the system size [28].

To describe the response in the strictly linear regime it is only necessary to consider the linear part of the equations of motion. In this case the algorithms are faster and the applied strain is, by construction, asymptotically small. For nonlinear algorithms one has to test that the resulting stress-strain curve is indeed linear.

Let $|\boldsymbol{X}\rangle$ be a vector containing $2N$ elements which are the positions of all particles in mechanical equilibrium. Starting from this equilibrium configuration, we expand the change in energy ΔU in terms of $|\boldsymbol{u}\rangle$, which contains the linear displacements of the particles from the initial condition. (The simulation box is held fixed - see Section 2.4 for linear response including box degrees of freedom.) The energy change caused by the displacements until quadratic order is:

$$\Delta U(|\boldsymbol{u}\rangle) = \frac{1}{2} \sum_{i\alpha, j\beta} \underbrace{\left. \frac{\partial^2 U}{\partial u_{i\alpha} \partial u_{j\beta}} \right|_{|\boldsymbol{X}\rangle}}_{\mathcal{K}_{i\alpha, j\beta}} u_{i\alpha} u_{j\beta} = \frac{1}{2} \langle \boldsymbol{u} | \hat{\mathcal{K}} | \boldsymbol{u} \rangle . \qquad (2.3)$$

Since the system is in mechanical equilibrium the gradient, which means the linear term, vanishes. The first non-vanishing term in the energy change is therefore quadratic in the displacements. This term is proportional to the

second derivatives of the energy in the equilibrium condition, which form the Hessian or stiffness matrix $\hat{\mathcal{K}}$. It is also equivalent to the dynamical matrix if all masses are set to one. If a displacement field $|\boldsymbol{u}\rangle$ is applied to the system, the particles experience a body force $|\boldsymbol{F}\rangle$, which is:

$$\hat{\mathcal{K}}\,|\boldsymbol{u}\rangle = |\boldsymbol{F}\rangle\,. \tag{2.4}$$

On the other hand the case in which a body force is applied the linear set of equations above is solved for the displacements $|\boldsymbol{u}\rangle$.

The Hessian matrix also yields the normal modes (eigenvectors) $|\boldsymbol{\omega}_i\rangle$ and the corresponding eigenvalues ω_i^2 of the response. The eigenvectors have norm one and are orthogonal because $\hat{\mathcal{K}}$ is a real symmetric matrix. Considering the eigenvalue equation:

$$\hat{\mathcal{K}}\,|\boldsymbol{\omega}_i\rangle = \omega_i^2\,|\boldsymbol{\omega}_i\rangle \quad \Leftrightarrow \quad \langle\boldsymbol{\omega}_i|\,\hat{\mathcal{K}}\,|\boldsymbol{\omega}_i\rangle = \omega_i^2\,. \tag{2.5}$$

and comparing it to (2.3) we find that $\omega_i^2/2$ is the energy cost of deforming the system along an eigenmode $|\boldsymbol{\omega}_i\rangle$ with an amplitude of one. The full response $|\boldsymbol{u}\rangle$ is a superposition of all eigenmodes $|\boldsymbol{u}\rangle = \sum_i a_i\,|\boldsymbol{\omega}_i\rangle$. Inserting this into equation (2.4) it is possible to derive the a_i and therefore the linear response in terms of the eigenvalues and eigenvectors

$$|\boldsymbol{u}\rangle = \sum_i \frac{\langle\boldsymbol{F}|\boldsymbol{\omega}_i\rangle}{\omega_i^2}\,|\boldsymbol{\omega}_i\rangle = \sum_i \frac{\Xi_i}{\omega_i^2}\,|\boldsymbol{\omega}_i\rangle\,. \tag{2.6}$$

The contribution of a normal mode to the overall response is linear in $\Xi_i = \langle\boldsymbol{F}|\boldsymbol{\omega}_i\rangle$. We therefore refer to it as coupling between an eigenmode and the applied force. Equation (2.6) shows that if two modes have the same coupling the one with lower eigenfrequency has greater influence on the linear response. In the Chapters 4 and 5 we will show that the coupling is well approximated by a constant $\Xi(\omega) = \Xi$ for the systems and forces we are considering. This means that we are able to draw a direct connection between the energy cost of a normal mode and its contribution to the linear response.

The solid body translations of the system do not cost energy. Upon solving equation (2.4) one finds a two-dimensional space of solutions for $|\boldsymbol{u}\rangle$. However, if there is no net force acting on the system there is no coupling between the solid body translations and the force. In that case the translations do not participate in the response and there is a unique solution to equation (2.4). Rattlers also contribute an eigenmode with zero eigenfrequency but their coupling to an arbitrary body force vector is non-zero. This would cause the linear response to only consist of the displacement of the rattlers. For that reason all rattler are excluded from the linear response calculations.

So far we only considered how to calculate the linear response to a vector of body forces. However, ultimately, the goal is to calculate the response to any type of homogeneous deformation, such as shear and compression
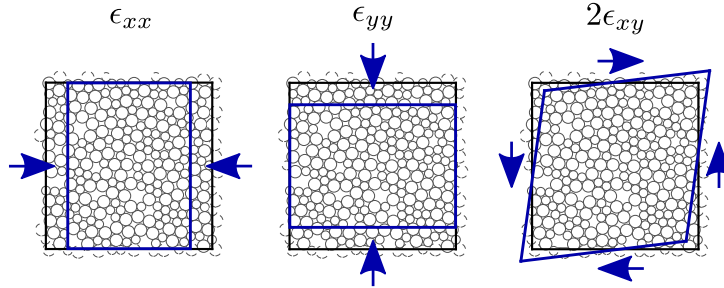
Figure 2.3: Three possible deformations: uniaxial compression in x direction ϵ_{xx} and uniaxial compression in y direction ϵ_{yy} together with a pure shear deformations ϵ_{xy}.

of the simulation cell. Before showing how this realized using the Hessian matrix, we present background about the elasticity tensor.

2.3. *The Elasticity Tensor*

We seek to calculate the elasticity tensor $\hat{\mathcal{C}}$ which is a linear connection between an applied strain $\epsilon_{\alpha\beta}$ and the resulting stress $\sigma_{\alpha\beta}$

$$\sigma_{\alpha\beta} = \mathcal{C}_{\alpha\beta\gamma\lambda}\,\epsilon_{\gamma\lambda}\,. \tag{2.7}$$

The $\mathcal{C}_{\alpha\beta\gamma\lambda}$ are called moduli or coupling parameters. $\epsilon_{\alpha\beta}$, $\sigma_{\alpha\beta}$ and $\mathcal{C}_{\alpha\beta,\gamma\lambda}$ are all symmetric. Usually these quantities are presented in Voigt notation [29] to reduce their order to two and one, respectively. The elasticity tensor becomes a matrix

$$\hat{\mathcal{C}} = \begin{pmatrix} \mathcal{C}_{xxxx} & \mathcal{C}_{xxyy} & \mathcal{C}_{xxxy} \\ \mathcal{C}_{yyxx} & \mathcal{C}_{yyyy} & \mathcal{C}_{yyxy} \\ \mathcal{C}_{xyxx} & \mathcal{C}_{xyyy} & \mathcal{C}_{xyxy} \end{pmatrix} \tag{2.8}$$

while stress and strain are now represented as vectors

$$|\boldsymbol{\sigma}\rangle = \begin{pmatrix} \sigma_{xx} & \sigma_{yy} & \sigma_{xy} \end{pmatrix}^T \quad \text{and} \quad |\boldsymbol{\epsilon}\rangle = \begin{pmatrix} \epsilon_{xx} & \epsilon_{yy} & 2\epsilon_{xy} \end{pmatrix}^T\,. \tag{2.9}$$

Because of symmetry the elements ϵ_{yx} and σ_{yx} are omitted and the amount of coupling parameters is reduced to six ($\mathcal{C}_{\alpha\beta\gamma\lambda} = \mathcal{C}_{\gamma\lambda\alpha\beta}$).

It is useful to represent $|\boldsymbol{\epsilon}\rangle$ as a superposition of three basis vectors $\hat{e}_{xx}, \hat{e}_{yy}$ and $\hat{e}_{xy}$ which all have norm one. $\hat{e}_{xx}$ and $\hat{e}_{yy}$ represent uniaxial compressions in x and y directions while $\hat{e}_{xy}$ denotes a pure shear deformation (see figure 2.3). The vector $|\boldsymbol{\epsilon}\rangle$ gives the amplitudes with which the individual deformations are applied. The above mentioned set of deformations is the canonical choice when choosing a basis set of deformations that spans the whole space of possible homogeneous deformations. It was also chosen for the implementation of the Hessian matrix presented in the next section. However, other choices are possible, because the elasticity tensor

can be expressed in any other basis via a transformation. For instance, the basis

$$\hat{e}_p = \frac{1}{\sqrt{2}}(\hat{e}_{xx} + \hat{e}_{yy}), \quad \hat{e}_q = \frac{1}{\sqrt{2}}(\hat{e}_{xx} - \hat{e}_{yy}), \text{ and } \quad \hat{e}_{xy} \tag{2.10}$$

2

includes two pure shear deformations (last two deformations) together with a compression/expansion (see figure 2.4). The original basis $|\epsilon\rangle$ in terms of the one above with amplitudes $|\epsilon'\rangle$ is

$$|\epsilon\rangle = \hat{\mathcal{Q}}|\epsilon'\rangle \quad \text{with} \quad \hat{\mathcal{Q}} = \begin{pmatrix} 1/\sqrt{2} & 1/\sqrt{2} & 0 \\ 1/\sqrt{2} & -1/\sqrt{2} & 0 \\ 0 & 0 & 1 \end{pmatrix}. \tag{2.11}$$

$\hat{\mathcal{Q}}$ is an orthogonal matrix, which keeps the length of the basis vectors and their relative orientation unchanged. It ensures that the elasticity tensor $\hat{\mathcal{C}}'$ represented in the new basis $|\epsilon'\rangle$ is still symmetric:

$$|\boldsymbol{\sigma}'\rangle = \hat{\mathcal{Q}}^T \hat{\mathcal{C}} \hat{\mathcal{Q}}|\epsilon'\rangle = \hat{\mathcal{C}}'|\epsilon'\rangle. \tag{2.12}$$

Consequently, it is only necessary to choose one set of deformations when implementing the Hessian matrix. All other moduli which are originally not included can be deduced as shown above.

The networks or packings we are considering are each individually anisotropic and all elements in $\hat{\mathcal{C}}$ are in general non-zero. In an ensemble sense, however, the systems are isotropic, so the number of independent parameters can be further reduced. First, all elements of $\hat{\mathcal{C}}$ which couple compression and shear have to vanish. This stems from the fact that there is no preferred direction of shear in isotropic systems - therefore compression cannot cause a shear. Additionally, the response to a uniaxial compression has to be independent of whether it is applied in the x or y direction. This reduces $\hat{\mathcal{C}}$ and $\hat{\mathcal{C}}'$ to

$$\hat{\mathcal{C}} = \begin{pmatrix} \mathcal{C}_{xxxx} & \mathcal{C}_{xxyy} & 0 \\ \mathcal{C}_{xxyy} & \mathcal{C}_{xxxx} & 0 \\ 0 & 0 & \mathcal{C}_{xyxy} \end{pmatrix} \quad \hat{\mathcal{C}}' = \begin{pmatrix} \mathcal{C}_{xxxx} + \mathcal{C}_{xxyy} & 0 & 0 \\ 0 & \mathcal{C}_{xxxx} - \mathcal{C}_{xxyy} & 0 \\ 0 & 0 & \mathcal{C}_{xyxy} \end{pmatrix}. \tag{2.13}$$

The fact that $\hat{\mathcal{C}}'$ is diagonal shows that the strains (2.10) are "eigenstrains" of an isotropic system. If any of the three strains ϵ_p, ϵ_q, or $2\epsilon_{xy}$ are applied there is only a change in the corresponding stress. This is different in the basis $|\epsilon\rangle$ where, for instance, applying ϵ_{xx} causes σ_{yy} to change.

The diagonal form of $\hat{\mathcal{C}}'$ is helpful. We can immediately identify the bulk modulus $\mathcal{C}_{xxxx} + \mathcal{C}_{xxyy} = 2K$ (see Landau and Lifschitz [30]). The other two elements are both the shear moduli of pure shear deformations which are the same in an isotropic medium $\mathcal{C}_{xxxx} - \mathcal{C}_{xxyy} = 2G$ and $\mathcal{C}_{xyxy} = G$. The factor of two is caused by the factor of two in the strain tensor definition. In this thesis we most commonly show data for the shear modulus G, the
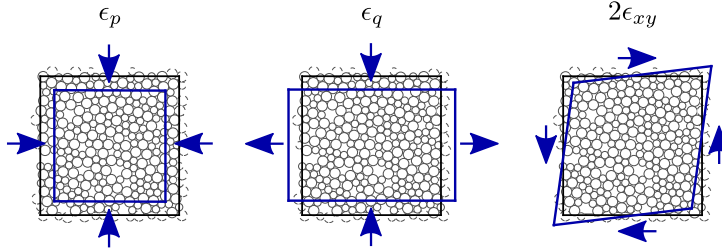
Figure 2.4: Three deformations forming a full basis of all possible homogeneous deformations: Compression, and two pure shear deformations.

bulk modulus K, and the mixed modulus $C = K + G$. Back in the basis $|\epsilon\rangle$ the elasticity tensor is therefore shown in the following two forms:

$$\hat{\mathcal{C}} = \begin{pmatrix} K+G & K-G & 0 \\ K-G & K+G & 0 \\ 0 & 0 & G \end{pmatrix} \text{ and } \quad \hat{\mathcal{C}} = \begin{pmatrix} C & C-2G & 0 \\ C-2G & C & 0 \\ 0 & 0 & G \end{pmatrix}. \tag{2.14}$$

2.4. *Applying Homogeneous Deformations*

Figure 2.3 illustrates that it is necessary to have degrees of freedom that control the shape of the simulation cell in order to apply a homogeneous deformation with which we can measure the individual elements of $\hat{\mathcal{C}}$. A deformation is described by a deformation gradient $\hat{\mathcal{F}}$ which consists of the derivatives of the the coordinates after the deformation X'_i with respect to their values X_i before the deformation. A general form is:

$$X'_i = \hat{\mathcal{F}} X_i \quad \text{with} \quad \mathcal{F}_{\alpha\beta} = \frac{\partial X'_{i\alpha}}{\partial X_{i\beta}} = \delta_{\alpha\beta} + \epsilon_{\alpha\beta} \tag{2.15}$$

with $\epsilon_{\alpha\beta} = \epsilon_{\beta\alpha}$. The last expression on the right gives an explicit form of the deformation gradient in the linear regime where it is an affine (homogeneous) deformation. In that case $\hat{\mathcal{F}}$ is the same everywhere in the system.

If the response of a system is purely affine all particles follow the deformation gradient as stated in (2.15), which means that the displacements are $u^{\mathrm{a}}_{i\alpha} = \sum_\beta \epsilon_{\alpha\beta} X_{i\beta}$. In case of a disordered system the deformation also causes non-affine displacements $\boldsymbol{u}$, which are displacements deviating from the affine displacements described by the homogeneous deformation gradient in equation (2.15). The total displacement $\boldsymbol{u}^{\mathrm{tot}}$ is given by the superposition of the non-affine with the affine part [31]:

$$u^{\mathrm{tot}}_{i\alpha} = u_{i\alpha} + u^{\mathrm{a}}_{i\alpha} = u_{i\alpha} + \sum_\beta \epsilon_{\alpha\beta} X_{i\beta}. \tag{2.16}$$

Similar to equation (2.3), we expand the change of the energy in powers of the displacements, which are a function of the non-affine displacements

and the applied strain:

$$\Delta U(|\boldsymbol{u}^{\text{tot}}\rangle) = \sum_{i\alpha} \underbrace{\left.\frac{\partial U}{\partial u_{i\alpha}}\right|_{|\boldsymbol{X}\rangle}}_{0} u_{i\alpha} + \sum_{\alpha\beta} \underbrace{\left.\frac{\partial U}{\partial \epsilon_{\alpha\beta}}\right|_{|\boldsymbol{X}\rangle}}_{\sigma_{\alpha\beta,0}V} \epsilon_{\alpha\beta} + \frac{1}{2}\sum_{i\alpha,j\beta} \underbrace{\left.\frac{\partial^2 U}{\partial u_{i\alpha}\partial u_{j\beta}}\right|_{|\boldsymbol{X}\rangle}}_{\mathcal{K}^{\text{pp}}_{i\alpha,j\beta}} u_{i\alpha} u_{j\beta}$$

$$+ \sum_{i\alpha,\beta\gamma} \underbrace{\left.\frac{\partial^2 U}{\partial u_{i\alpha}\partial \epsilon_{\beta\gamma}}\right|_{|\boldsymbol{X}\rangle}}_{\mathcal{K}^{\text{bp}}_{i\alpha,\beta\gamma}} u_{i\alpha}\epsilon_{\beta\gamma} + \frac{1}{2}\sum_{\alpha\beta\gamma\lambda} \underbrace{\left.\frac{\partial^2 U}{\partial \epsilon_{\alpha\beta}\partial \epsilon_{\gamma\lambda}}\right|_{|\boldsymbol{X}\rangle}}_{\mathcal{K}^{\text{bb}}_{\alpha\beta\gamma\lambda}} \epsilon_{\alpha\beta}\epsilon_{\gamma\lambda} \,. \quad (2.17)$$

This expansion contains the familiar gradient of the energy, which vanishes in the equilibrium condition but now has another contribution associated with the box degrees of freedom. The contribution does not vanish if the system is under pre-stress, $\sigma_{\alpha\beta,0} \neq 0$, and adds a term linear in the applied strain. Furthermore, there is the term that forms the Hessian matrix which was already mentioned in Section 2.2. In this expression we give the Hessian the superscript "pp" to emphasize that it contains the particle-particle-interactions. $\hat{\mathcal{K}}^{\text{pp}}$ is identical to $\hat{\mathcal{K}}$ in equation (2.3). Aside from the familiar terms that denote particle interactions, there is also a term that couples the box deformation and the particle positions and a term that only couples box degrees of freedom.

The next step is to alter equation (2.17) into an equation similar to (2.3), which consists only of one matrix. First, all stress and strain elements are gathered in two vectors, see equation (2.9). Now equation (2.17) can be written in a more succinct way:

$$\Delta U(|\boldsymbol{u},\boldsymbol{\epsilon}\rangle) = V\langle \boldsymbol{\sigma_0}|\boldsymbol{\epsilon}\rangle + \frac{1}{2}\langle \boldsymbol{u}|\hat{\mathcal{K}}^{\text{pp}}|\boldsymbol{u}\rangle + \langle \boldsymbol{\epsilon}|\hat{\mathcal{K}}^{\text{bp}}|\boldsymbol{u}\rangle + \frac{1}{2}\langle \boldsymbol{\epsilon}|\hat{\mathcal{K}}^{\text{bb}}|\boldsymbol{\epsilon}\rangle \quad (2.18)$$

$\hat{\mathcal{K}}^{\text{bp}}$ is a $3\times 2N$ matrix and $\hat{\mathcal{K}}^{\text{bb}}$ is a 3×3 matrix. Now if all degrees of freedom are gathered in one state vector $|\boldsymbol{u},\boldsymbol{\epsilon}\rangle$, all four terms in the equation above can be combined into one matrix

$$\hat{\mathcal{K}}^{\epsilon} = \begin{pmatrix} \hat{\mathcal{K}}^{\text{pp}} & \hat{\mathcal{K}}^{\text{pb}} \\ \hat{\mathcal{K}}^{\text{bp}} & \hat{\mathcal{K}}^{\text{bb}} \end{pmatrix} \quad \text{with} \quad \hat{\mathcal{K}}^{\text{pb}} = \left(\hat{\mathcal{K}}^{\text{bp}}\right)^T \quad (2.19)$$

containing both particle and box degrees of freedom. Finally it is possible to write the change in energy in a similar manner to equation (2.3):

$$\Delta U(|\boldsymbol{u},\boldsymbol{\epsilon}\rangle) = V\langle \boldsymbol{0},\boldsymbol{\sigma_0}|\boldsymbol{u},\boldsymbol{\epsilon}\rangle + \frac{1}{2}\langle \boldsymbol{u},\boldsymbol{\epsilon}|\hat{\mathcal{K}}^{\epsilon}|\boldsymbol{u},\boldsymbol{\epsilon}\rangle \,. \quad (2.20)$$

Applying an arbitrary deformation $|\boldsymbol{u},\boldsymbol{\epsilon}\rangle$ causes the body forces and the stress to be $|\boldsymbol{F},\boldsymbol{\sigma}V\rangle = |\boldsymbol{0},\boldsymbol{\sigma_0}V\rangle + \hat{\mathcal{K}}^{\epsilon}|\boldsymbol{u},\boldsymbol{\epsilon}\rangle$. However, if only the boundaries are forced, all body forces are zero. The field of nonaffine displacements and the strain in response to a stress can be obtained by solving the equation

$$\hat{\mathcal{K}}^{\epsilon}|\boldsymbol{u},\boldsymbol{\epsilon}\rangle = |\boldsymbol{0},(\boldsymbol{\sigma}-\boldsymbol{\sigma_0})V\rangle = |\boldsymbol{0},\Delta\boldsymbol{\sigma}V\rangle \,. \quad (2.21)$$

The equation above represents a "stress-controlled" deformation. If a system is deformed through stress control, a specific stress is applied at the boundaries. The resulting strain can then be measured. In such a stress-controlled simulation one measures a compliance tensor $\hat{S}$ instead of the elasticity tensor. The two are connected simply by inversion $\hat{C} = \hat{S}^{-1}$. To calculate the whole 3×3 compliance tensor it is necessary to solve (2.21) three times, applying each of the three deformations shown in figure 2.3 separately. Each solution consists of a vector with three elements, two of which yield information about the coupling between deformations. All three vectors combined finally yield the complete compliance tensor.

It is also possible to implement the deformation in a "strain-controlled" manner - a strain is applied to the system and the resulting stress is measured. Here $\hat{\mathcal{K}}^{\epsilon}$ is decomposed back into the four matrices

$$
\begin{aligned}
\hat{\mathcal{K}}^{\mathrm{pp}} \left| \boldsymbol{u} \right\rangle + \hat{\mathcal{K}}^{\mathrm{pb}} \left| \boldsymbol{\epsilon} \right\rangle &= \left| \boldsymbol{0} \right\rangle \\
\hat{\mathcal{K}}^{\mathrm{bp}} \left| \boldsymbol{u} \right\rangle + \hat{\mathcal{K}}^{\mathrm{bb}} \left| \boldsymbol{\epsilon} \right\rangle &= \left| \Delta \boldsymbol{\sigma} \right\rangle .
\end{aligned}
\tag{2.22}
$$

This set of linear equations can be solved by solving the upper equation $\left| \boldsymbol{u} \right\rangle = -(\hat{\mathcal{K}}^{\mathrm{pp}})^{-1} \hat{\mathcal{K}}^{\mathrm{pb}} \left| \boldsymbol{\epsilon} \right\rangle$ and inserting the result into the lower equation:

$$
\left| \Delta \boldsymbol{\sigma} \right\rangle = \underbrace{\left(\hat{\mathcal{K}}^{\mathrm{bb}} - \hat{\mathcal{K}}^{\mathrm{bp}} (\hat{\mathcal{K}}^{\mathrm{pp}})^{-1} \hat{\mathcal{K}}^{\mathrm{pb}} \right)}_{\hat{\mathcal{C}}} \left| \boldsymbol{\epsilon} \right\rangle .
\tag{2.23}
$$

The elements of $\hat{\mathcal{K}}^{\mathrm{bb}}$ are also called Born or affine moduli. If nonaffine displacements are absent $\hat{\mathcal{C}} = \hat{\mathcal{K}}^{\mathrm{bb}}$. This applies to perfect crystals.

In practice it is numerically inefficient to compute the inverse of $\hat{\mathcal{K}}^{\mathrm{pp}}$ directly. It is better to solve the first of the two equations in (2.22) for three different deformations separately, similarily as in the calculation of $\hat{S}$, and then combining the result to obtain $\hat{\mathcal{C}}$.

Calculating the moduli in a strain controlled fashion has numerical advantages. The matrix which has to be inverted is $\hat{\mathcal{K}}$ and not $\hat{\mathcal{K}}^{\epsilon}$. The convergence rate and the accuracy of the solution of linear solvers is determined by the condition number which is, in case of the Hessian matrix, given by the ratio of the largest and smallest eigenvalue $\kappa(\hat{\mathcal{K}}) = \lambda_{\max} / \lambda_{\min}$. For both $\hat{\mathcal{K}}$ and $\hat{\mathcal{K}}^{\epsilon}$ the smallest eigenvalues are approximately the same. However, the eigenvalue in $\hat{\mathcal{K}}^{\epsilon}$ which corresponds to the deformation of the box is of order N, while the largest eigenvalue in $\hat{\mathcal{K}}$ is of order one. This means that the linear system of equations which has to be solved in strain control is numerically more stable.

The results for the linear response presented throughout this thesis were obtained with direct solvers from the Eigen C++ library [32]. In case of real linear equations we used a sparse LDL^T decomposition which is a variant of the Cholesky decomposition. For complex equations a sparse LU decomposition was used. Decompositions are useful if it is necessary to solve for several force vectors, because the decomposition can simply be

(a)   (b)
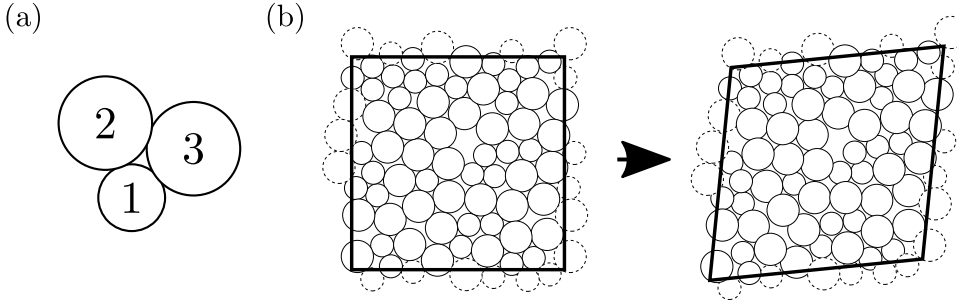
Figure 2.5: (a) Three disks overlapping in a soft sphere packing. (b) Purely affine pure shear deformation of a soft sphere packing.

reused. This is beneficial if more than one deformation is applied to the system. For example, in Chapter 3 the same system of linear equations is solved for more than one hundred force vectors.

While the idea of adding box degrees of freedom was introduced here in a general way, the following sections only focus on shear to simplify the notation.

The following section gives the Hessian in the specific case of soft sphere packings. It also gives details how the Hessian is implemented in the code for one box degree of freedom. Section 2.6 focuses on an extension of the method described here in which dynamics are also considered.

2.5. *The Hessian Matrix for Soft Sphere Packings*

This section derives concrete expressions for the Hessian matrix in the case of soft sphere packings undergoing a pure shear deformation, as depicted in figure 2.5b. While it is possible to calculate $\hat{\mathcal{K}}^\epsilon$ straightforwardly using the expression given in the expansion of the energy (2.17), we follow a different approach in this section that is flexible and easier to implement. The idea is to split the calculation of the Hessian into two steps: First a Hessian is calculated which only depends on the interaction potential and does not contain information about the contact network. This information is added in a second step in which the box degrees of freedom are considered.

First, the interaction potential is rewritten using small relative displacements $\Delta\boldsymbol{u}_{ij} = \boldsymbol{u}_j - \boldsymbol{u}_i$:

$$\Delta U(|\Delta\boldsymbol{u}\rangle) = \frac{k}{2} \sum_i \sum_{\langle ij \rangle} \left(R_i + R_j - |\boldsymbol{r_j} - \boldsymbol{r_i} + \Delta\boldsymbol{u}_{ij}| \right)^2. \qquad (2.24)$$

$\langle ij \rangle$ denotes the sum over all particles j which particle i is in contact with. Note that this expression is in terms of the change in the relative distance between any two particles i and j. The vector $|\Delta\boldsymbol{u}\rangle$ has Nz elements. Taking

the second derivatives of the energy in this relative basis gives a matrix $\hat{\mathcal{K}}^\Delta$ with dimension $Nz \times Nz$ which only has 2×2 matrices $\hat{\mathcal{K}}^\Delta_{ij}$ along its diagonal

$$\left.\frac{\partial^2 \Delta U(|\Delta \boldsymbol{u}\rangle)}{\partial^2 \Delta \boldsymbol{u}_{ij}}\right|_{|\boldsymbol{0}\rangle} = \hat{\mathcal{K}}^\Delta_{ij} = k \left[\hat{\mathbb{1}} + \frac{(R_i + R_j)}{r_{ij}^3} \begin{pmatrix} -y_{ij}^2 & x_{ij}y_{ij} \\ x_{ij}y_{ij} & -x_{ij}^2 \end{pmatrix}\right] \tag{2.25}$$

and is zero otherwise. x_{ij} and y_{ij} are the elements of r_{ij}. Each contact is uniquely identified by ij with $i > j$ so that contacts are not counted twice.

The second step is to transform $\hat{\mathcal{K}}^\Delta$ into the Hessian, which acts on the set of all absolute displacements $|\boldsymbol{u}, \gamma\rangle$. Consequently, we are looking for a transformation $\hat{\mathcal{A}}$ such that

$$\hat{\mathcal{A}} |\boldsymbol{u}, \gamma\rangle = |\Delta \boldsymbol{u}\rangle \tag{2.26}$$

where $\hat{\mathcal{A}}$ is a $2N + 1 \times Nz$ matrix that implements the connectivty of the network and also adds the box degree of freedom. The Hessian $\hat{\mathcal{K}}^\epsilon$ can be calculated with

$$\hat{\mathcal{K}}^\epsilon = \hat{\mathcal{A}}^T \hat{\mathcal{K}}^\Delta \hat{\mathcal{A}}. \tag{2.27}$$

While we are focusing here on the case of pure shear, the choice of which deformation to apply does not influence the first step of the calculation. The box degrees have to be considered for the calculation of $\hat{\mathcal{A}}$ because the relation between relative and absolute displacements depends on the exact choice. For the pure shear depicted in figure 2.5b, we have the relation

$$\begin{aligned} \Delta u_{ij,x} &= u_{j,x} - u_{i,x} + \gamma y_{ij} \\ \Delta u_{ij,y} &= u_{j,y} - u_{i,y} + \gamma x_{ij} . \end{aligned} \tag{2.28}$$

between relative and absolute coordinates. $\hat{\mathcal{A}}$ can be rewritten in terms of the derivatives of $\Delta u_{ij,\alpha}$ with respect to $u_{k\alpha}$

$$\begin{aligned} \Delta u_{ij,\alpha} &= \sum_k \frac{\partial(\Delta u_{ij,\alpha})}{\partial u_{k\alpha}} u_{k\alpha} + \frac{\partial(\Delta u_{ij,\alpha})}{\partial \gamma} \gamma \\ \Rightarrow \quad |\Delta u_{ij}\rangle &= \hat{\mathcal{A}}^{\text{pp}} |\boldsymbol{u}\rangle + \mathcal{A}^{\text{pb}} \gamma . \end{aligned} \tag{2.29}$$

$\hat{\mathcal{A}}^{\text{pp}}$ is a $Nz \times 2N$ matrix which does not depend on the box degree of freedom. $\mathcal{A}^{\text{pb}}$ is a vector of size Nz (or a matrix in the case that more than one box degree of freedom is used).

For a small assembly of particles shown in 2.5a with three particles having three contacts 31, 32, and 21 one gets the following transformation matrix:

$$\hat{\mathcal{A}} = \left(\hat{\mathcal{A}}^{\text{pp}} \ \mathcal{A}^{\text{pb}}\right) = \begin{array}{c} \\ \Delta u_{32,x} \\ \Delta u_{32,y} \\ \Delta u_{31,x} \\ \Delta u_{31,y} \\ \Delta u_{21,x} \\ \Delta u_{21,y} \end{array} \begin{array}{c} \begin{array}{ccccccc} u_{1,x} & u_{1,y} & u_{2,x} & u_{2,y} & u_{3,x} & u_{3,y} & \gamma \end{array} \\ \begin{pmatrix} 0 & 0 & 1 & 0 & -1 & 0 & y_{32} \\ 0 & 0 & 0 & 1 & 0 & -1 & x_{32} \\ 1 & 0 & 0 & 0 & -1 & 0 & y_{31} \\ 0 & 1 & 0 & 0 & 0 & -1 & x_{31} \\ 1 & 0 & -1 & 0 & 0 & 0 & y_{21} \\ 0 & 1 & 0 & -1 & 0 & 0 & x_{21} \end{pmatrix} \end{array} .$$

It is easy to add and remove box degrees of freedom by simply adding and removing columns accordingly. The rest of the calculation of $\hat{\mathcal{K}}^\epsilon$ does not depend on which box degrees of freedom are used.

One disadvantage of the method presented here is that instead of initializing elements of the final Hessian directly, one has to initialize two additional temporary matrices. Consequently, the method presented above has higher memory demands compared to a direct calculation of the Hessian. However, for all matrices involved a large fraction of the elements are zero. In fact, the number of nonzero elements is proportional to the number of contacts $Nz/2$ in the system, which is proportional to N. The size of the matrices increases as N^2, which means that the fraction of nonzero elements is $1/N$ in all matrices and therefore vanishes in large systems. For this reason it is beneficial to store all matrices in a sparse matrix format, for which the memory demand increases only linearly with the system size. In that context storing two additional matrices does not cause any problems even for the larger systems discussed in the course of this thesis, for which $N = 65536$.

2.6. *Adding Dynamics - Oscillatory Rheology*

To probe the viscoelastic response of materials it is common to perform oscillatory rheology measurements. In these experiments a sample is deformed with a periodic force $e^{i\omega t} |\mathbf{0}, \sigma_{xy}\rangle$ and one measures the frequency dependent shear modulus G^*. This so called dynamical modulus is a complex number $G^* = G' + iG''$, where the real part is called the storage modulus and is proportional to the energy stored elastically. The imaginary part is proportional to the energy which is dissipated during one deformation cycle and is therefore also refered to as the loss modulus. The fact that the modulus is a complex number reflects that there is a phase difference between shear stress σ_{xy} and strain γ (see figure 2.6). The phase angle θ is given by $\theta = \arctan(G''/G')$.
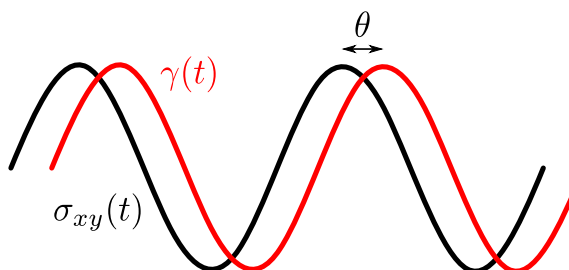

Figure 2.6: The damping causes a phase difference between stress and strain. As the loss modulus becomes much larger than the storage modulus this phase angle approaches $\pi/2$.

The Hessian matrix approach mentioned above describes quasistatic response. It is therefore insufficient to calculate G^* at finite frequencies. To add information about time scales it is necessary to add damping to the equations of motion. In the linear regime this adds another term to (2.21) that is linear in the velocity of the particles

$$\hat{\mathcal{K}}^\epsilon |\boldsymbol{u}, \gamma\rangle + \hat{\mathcal{B}}^\epsilon |\dot{\boldsymbol{u}}, \dot{\gamma}\rangle = e^{i\omega t} |\boldsymbol{0}, \gamma\rangle \ . \tag{2.30}$$

The equation above is an overdamped driven oscillator with driving frequency ω. The damping matrix $\hat{\mathcal{B}}^\epsilon$ is derived from Rayleigh's dissipation function $\mathcal{R}$ which can be used in Lagrangian mechanics to implement dissipation [33]. $\mathcal{R}$ is constructed such that the negative gradient with respect to the velocity gives the dissipative force

$$|F\rangle_{\text{diss}} = -\frac{\partial \mathcal{R}}{\partial |\dot{\boldsymbol{u}}, \dot{\gamma}\rangle} \ . \tag{2.31}$$

Note that box degrees of freedom are also included. The exact form of $\mathcal{R}$ depends on the damping law - see Chapter 6 for explicit expression of $\mathcal{R}$ for a variety of damping laws. The damping matrix is defined similarly to the Hessian by the second derivatives of the Rayleigh dissipation function:

$$\mathcal{B}^{\text{pp}}_{i\alpha j\beta} = \left.\frac{\partial^2 \mathcal{R}}{\partial \dot{u}_{i\alpha} \partial \dot{u}_{j\beta}}\right|_{|\boldsymbol{0}\rangle} , \ \mathcal{B}^{\text{pb}}_{i\alpha} = \left.\frac{\partial^2 \mathcal{R}}{\partial \dot{u}_{i\alpha} \partial \dot{\gamma}}\right|_{|\boldsymbol{0}\rangle} , \text{ and } \quad \mathcal{B}^{\text{bb}} = \left.\frac{\partial^2 \mathcal{R}}{\partial^2 \dot{\gamma}}\right|_{|\boldsymbol{0}\rangle} . \tag{2.32}$$

Because we are dealing with a driven oscillator, the differential equation can be solved with the ansatz

$$|\boldsymbol{u}, \gamma\rangle = |\boldsymbol{A}, A_\gamma\rangle \, e^{i\omega t} \,, \tag{2.33}$$

with complex amplitudes $|\boldsymbol{A}, A_\gamma\rangle$ that depend on the driving frequency. A more general ansatz would be with a frequency Ω not necessarily equal to the driving frequency. However, the system will eventually oscillate with the driving frequency after an intial transient period. The ansatz therefore describes the response after the system has reached a stable oscillation. Inserting the ansatz into equation (2.30) and canceling the exponential gives

$$\left(\hat{\mathcal{K}}^\epsilon + i\omega \hat{\mathcal{B}}^\epsilon\right) |\boldsymbol{A}, A_\gamma\rangle = |\boldsymbol{0}, \sigma_{xy} V\rangle \ . \tag{2.34}$$

This complex linear set of equations can be solved with any driving frequency for the amplitudes of the resulting oscillation. Finally, the shear modulus is $G^* = 1/A_\gamma$.

Another important experimental setup is the application of a sudden stress. The system starts in mechanical equilibrium and at $t = 0$ a stress $|\sigma_{xy} V\rangle$ is applied infinitely fast - the stress is a step funtion in time. The differential equation which describes this setup after the stress was applied is

$$\hat{\mathcal{K}}^\epsilon |\boldsymbol{u}, \gamma\rangle + \hat{\mathcal{B}}^\epsilon |\dot{\boldsymbol{u}}, \dot{\gamma}\rangle = |\boldsymbol{0}, \sigma_{xy} V\rangle \tag{2.35}$$

which is a first order inhomogeneous differential equation. The solution of such an equation is the superposition of the general solution of the homogeneous equation and a particular solution of the inhomogeneous equation. The latter can be constucted by setting $|\dot{\boldsymbol{u}}, \dot{\gamma}\rangle = |\boldsymbol{0}, 0\rangle$, which recovers equation (2.21). The homogeneous part can be solved with an exponential ansatz

$$|\boldsymbol{u}, \gamma\rangle = \sum_i e^{-s_i t} |\boldsymbol{s}_i, s_i^\gamma\rangle \ . \tag{2.36}$$

This ansatz and the particular solution of the inhomogeneous equation give a clear picture of the dynamics. Subjecting the initial equilibrium configuration to a sudden stress change causes it to relax into a new equilibrium condition which is given by the quasistatic solution (after waiting an inifinitely long time), which can be calculated by solving (2.21). The relaxation process can be decomposed into exponential functions that each have an associated relaxation rate s_i. The relaxation rates and the associated mode $|\boldsymbol{s}_i, s_i^\gamma\rangle$ can be calculated by inserting (2.36) into the homogeneous equation:

$$\sum_i \left(\hat{\mathcal{K}}^\epsilon - s_i \hat{\mathcal{B}}^\epsilon \right) e^{-s_i t} |\boldsymbol{s}_i, s_i^\gamma\rangle = 0 \ . \tag{2.37}$$

For a set of linearly independent modes $|\boldsymbol{s}_i, s_i^\gamma\rangle$ this equation can only have a solution if all parts of the sum vanish independently. This yields the following generalized eigenvalue equation

$$\hat{\mathcal{K}}^\epsilon |\boldsymbol{s}_i, s_i^\gamma\rangle = s_i \hat{\mathcal{B}}^\epsilon |\boldsymbol{s}_i, s_i^\gamma\rangle \ . \tag{2.38}$$

The eigenvalues s_i are the relaxation constants and $|\boldsymbol{s}_i, s_i^\gamma\rangle$ are the eigenmodes which are $\hat{\mathcal{B}}^\epsilon$-orthogonal, $\langle \boldsymbol{s}_i, s_i^\gamma | \hat{\mathcal{B}}^\epsilon | \boldsymbol{s}_j, s_j^\gamma \rangle = 0$ if $i \neq j$. The eigenvalues give time scales on which a certain eigenmode relaxes and the eigenvector gives the displacement field of the eigenmode. This is helpful for describing the linear response on different time scales (see Chapter 6).

Furthermore, the eigenvalues and eigenvector obtained from equation (2.38) can be used to solve equation (2.34). We know that the solution can be decomposed into the relaxation modes $|\boldsymbol{A}, A_\gamma\rangle = \sum_i a_i |\boldsymbol{s}_i, s_i^\gamma\rangle$. Inserting this decomposition into equation (2.34), using the generalized eigenvalue equation (2.38) and the fact that the eigenmodes are $\hat{\mathcal{B}}$-orthogonal, one can derive that

$$|\boldsymbol{A}, A_\gamma\rangle = V \sum_i \frac{1}{(s_i + i\omega)} \frac{\langle \boldsymbol{0}, \sigma_{xy} | \boldsymbol{s}_i, s_i^\gamma \rangle}{\langle \boldsymbol{s}_i, s_i^\gamma | \hat{\mathcal{B}}^\epsilon | \boldsymbol{s}_i, s_i^\gamma \rangle} |\boldsymbol{s}_i, s_i^\gamma\rangle \ . \tag{2.39}$$

This result can be used to compute the shear modulus $1/G^* = \langle \boldsymbol{0}, 1 | \boldsymbol{A}, A^\gamma \rangle$ for all possible driving frequencies at once. However, numerically solving the generalized eigenvalue equation for both eigenvalues and eigenvectors is expensive and scales with the cube of the linear size of the matrices $\hat{\mathcal{K}}^\epsilon$ and $\hat{\mathcal{B}}^\epsilon$. Another challenge is that the resulting set of eigenvectors forms a

dense matrix which takes large amount of memory to store if the systems are large. For the system sizes used here it is faster and more memory efficient to solve equation (2.34) directly with a linear solver even though it is necessary to repeatedly solve the equation for all required values of ω.

2.7. *Finite Deformations*

While the strictly linear regime can be probed efficiently with the Hessian approach, it is not fit to investigate nonlinear phenomena like strain stiffening or the Poynting effect (see Chapter 5). On the one hand this is because soft sphere packings change their contact network as one deforms the system. On the other hand even the force (2.1) is nonlinear in the particle positions when $D > 1$, because of the square root in the norm of the separation vector $\boldsymbol{r}_{ij}$. It is therefore also necessary to implement nonlinear algorithms to investigate finite amplitude deformations in networks, which do not have contact changes.

   In the following we present a strain- and a stress-controlled manner to apply a quasistatic finite deformation using the FIRE algorithm [26]. After giving an introduction to the algorithm, we focus on two modes of deformations used in Chapter 5: the strain-controlled application of pure shear strain ϵ_q (Section 2.7.2) and the stress-controlled application of a combination of a pure shear stress q and pressure p (Section 2.7.3). The implementation described here was used for random elastic networks and has not been tested extensively for soft sphere packings. The FIRE algorithm itself is not influence by the type of system we use. However, certain parameters may have to be chosen differently.

2.7.1. *The FIRE algorithm*

The FIRE (Fast Inertial Relaxation Engine) algorithm was first introduced in [26]. The authors use the picture of a blindfolded skier in a mountainous area, which resembles the energy landscape of the system in question. The skier starts in an elevated position in the mountains and tries to find his way down into the valley without seeing. The algorithm suggests three rules that the skier should follow to arrive in the valley efficiently:

1. He should steer such that he slowly turns into the steepest direction pointing downhill

2. If he goes uphill he should stop and turn back downhill into the direction of steepest decent

3. The longer he goes downhill without stopping the more he should increase his velocity

The algorithm is implemented with an MD scheme based on the equation

$$|\dot{\boldsymbol{v}}(t)\rangle = \frac{1}{m}|\boldsymbol{F}\rangle - g(t)v(t)\left(\frac{|\boldsymbol{v}(t)\rangle}{v(t)} - \frac{|\boldsymbol{F}\rangle}{F}\right) \qquad (2.40)$$

with the mass of the skier m, the gradient of the energy $|\boldsymbol{F}\rangle = -\nabla U$, and the velocity $|\boldsymbol{v}(t)\rangle$. The function $g(t)$ implements the three rules. The right part of the equation proportional to the velocity is discretized using the Euler method:

$$|\boldsymbol{v}_t\rangle \rightarrow |\boldsymbol{v}_t\rangle - \alpha \, |\boldsymbol{v}_t\rangle + \alpha \frac{|\boldsymbol{F}\rangle}{F} \, |\boldsymbol{v}_t\rangle \qquad (2.41)$$

2

where $\alpha = g\Delta t$. The FIRE algorithm consists of the following steps:

1. The first part of equation (2.40) $|\dot{\boldsymbol{v}}(t)\rangle = |\boldsymbol{F}\rangle \, /m$ (with $m = 1$) is integrated using any common integrator. We choose a leapfrog integrator [34, 35]. Starting from the velocities $|\boldsymbol{v}_t\rangle$ and positions $|\boldsymbol{X}_t\rangle$ this yields new velocities and positions $|\boldsymbol{v}_{t+1}\rangle$ and $|\boldsymbol{X}_{t+1}\rangle$.

2. The new velocities and positions are used to calculate the scalar product $P = \langle \boldsymbol{v}_{t+1} | \boldsymbol{F}(|\boldsymbol{X}_{t+1}\rangle)\rangle$. The gradient is also used to check for convergence.

3. The new velocities are updated according to (2.41).

4. Depending on the sign of P one of the following steps is carried out afterwards:

   - $P < 0$: The velocities are set to zero $|\boldsymbol{v}_{t+1}\rangle = |\boldsymbol{0}\rangle$, the timestep is decreased $\Delta t \rightarrow f_{\mathrm{dec}}\Delta t$, and α is reset to its initial value $\alpha \rightarrow \alpha_0$.
   - $P > 0$ and the number of timesteps N_t since the last time $P < 0$ is $N_t > N_{\min}$: The timestep is increased $\Delta t \rightarrow \min\left(f_{\mathrm{inc}}\Delta t, \Delta t_{\max}\right)$ and α is decreased $\alpha \rightarrow f_\alpha \alpha$.

In the first case ($P < 0$) the skier is going uphill. He stops and turns into the direction of steepest decent. Decreasing the timestep has the effect that the skier is moving slower directly after stopping - in fact the algorithm progresses slower because it takes smaller steps during each iteration. In the second case ($P > 0$) the skier turns more into the direction of steepest decent (α is decreased) and increases movement speed (Δt is increased).

The steps above are repeated until no element in the gradient is larger than a threshold T which we choose to be $T = 10^{-10}$. The parameters above were chosen as suggested in [26]: $N_{\min} = 5$, $f_{\mathrm{inc}} = 1.1$, $f_{\mathrm{dec}} = 0.5$, $\alpha_0 = 0.1$, $f_\alpha = 0.99$, and $\Delta t_{\max} = 10\Delta t_0$ where we choose $\Delta t_0 = 0.1$.

We found that FIRE is easy to implement and its parameters do not need extensive problem-specific tuning. We use the same set of parameters for the deformation of quasistatic spring networks and the generation of soft sphere packings.

2.7.2. *Strain Control*

The application of a finite strain-controlled deformation is composed of two steps. First, an affine deformation is applied to the particle positions $\boldsymbol{X}_i$

and the lattice vectors $\boldsymbol{L}_x$ and $\boldsymbol{L}_y$:

$$\boldsymbol{X}'_i = \hat{\mathcal{F}}\boldsymbol{X}_i \quad \text{and} \quad \boldsymbol{L}'_\alpha = \hat{\mathcal{F}}\boldsymbol{L}_\alpha \quad \text{with} \quad \hat{\mathcal{F}} = \begin{pmatrix} 1 & \epsilon_q \\ \epsilon_q & 1 \end{pmatrix}. \tag{2.42}$$

2

After this affine deformation the particles are displaced out of their energy minimum. The gradient $|\boldsymbol{F}\rangle$ does not vanish anymore. In the second step the energy of the system is minimized keeping the shape of the box fixed.

After successful minimization the shear modulus can be calculated with the stress tensor

$$\sigma_{\alpha\beta} = \frac{1}{2V}\sum_{ij} f_{ij,\alpha}\frac{r_{ij,\beta}}{r_{ij}}$$

$$\text{with} \quad q = -\frac{1}{2}\cdot(\sigma_{xx} - \sigma_{yy}) \quad p = -\frac{1}{2}(\sigma_{xx} + \sigma_{yy}) \tag{2.43}$$

The shear modulus can be calculated with $G = q/\epsilon_q$. Alternatively, it is possible to calculate the shear modulus of the new configuration using the Hessian matrix. The calculation of the shear modulus with the stress tensor yields the secant modulus, while one calculates the tangent modulus with the Hessian.

When deforming soft sphere packings quasistatically it is necessary to keep the strain steps $\Delta\gamma$ small, otherwise the outcome of the minimization depends on its value. In the appendix of [36] it is shown that for packings the result of a shear deformation becomes independent of $\Delta\gamma$ if $\Delta\gamma < 10^{-4}$ if $N \leq 2048$. For the case of elastic networks, the choice of $\Delta\gamma$ is not as important because these materials are well approximated as hyperelastic. That means that the stress and the strain are not history dependent - they are state variables.

2.7.3. *Stress Control*

For the case of stress control, we target a certain shear stress q and pressure p. The potential energy of the system is minimized under the constraint that the pressure and shear stress in the final configuration are

$$q(\boldsymbol{X}_{\text{final}}) = q_t \quad \text{and} \quad p(\boldsymbol{X}_{\text{final}}) = p_t. \tag{2.44}$$

q_t and p_t are the target shear stress and pressure. The deformation gradient is

$$\hat{\mathcal{F}} = \begin{pmatrix} 1 + \epsilon_q & 0 \\ 0 & 1/(1 + \epsilon_q) \end{pmatrix} \cdot \begin{pmatrix} 1 + \epsilon_p & 0 \\ 0 & 1 + \epsilon_p \end{pmatrix}. \tag{2.45}$$

The minimization problem has $2N + 2$ degrees of freedom, which we choose to present here in a deformed simulation cell C' with coordinates $|\boldsymbol{X}'\rangle$ and strain ϵ_q and ϵ_p. The coordinates $|\boldsymbol{X}\rangle$ refer to a reference simulation cell C with volume V, which is defined to have zero strain. Also here we have the relation $|\boldsymbol{X}'\rangle = \hat{\mathcal{F}}|\boldsymbol{X}\rangle$

If a system changes shape or volume, it has to perform work against the external stresses q_t and p_t. A system that is inflated to a volume V' has to perform the work $W_p = p_t V'$. If a system starts as a square with volume V' and is deformed into a rectangle with the same volume, the work against the external shear stress is

$$W_q = 2q_t V' \ln(1 + \epsilon_q).$$ (2.46)

Including these two additional energy terms into the total energy of the system we get

$$H(\boldsymbol{X}') = U(\boldsymbol{X}') + p_t V' + 2q_t V' \ln(1 + \epsilon_q)$$ (2.47)

which is an enthalpy. From this enthalpy we can derive the forces which are associated with the particle degrees of freedom, as well as the forces associated with the degrees of freedom of the box:

$$\boldsymbol{F}_i = -\left(\frac{\partial H(\boldsymbol{X}')}{\partial \boldsymbol{X}'_i}\right)_{\epsilon_p=0,\epsilon_q=0} = -k\sum_j \delta_{ij} \frac{\boldsymbol{r}_{ij}}{r_{ij}}$$

$$F_p = -\left(\frac{\partial H(\boldsymbol{X}')}{\partial \epsilon_p}\right)_{|\boldsymbol{X}\rangle,\epsilon_q=0} = 2V\left(p(\boldsymbol{X}) - p_t\right)$$

$$F_q = -\left(\frac{\partial H(\boldsymbol{X}')}{\partial \epsilon_q}\right)_{|\boldsymbol{X}\rangle,\epsilon_p=0} = 2V\left(q(\boldsymbol{X}) - q_t\right).$$

The gradient is evaluated at zero because each step in the minimization algorithm starts in $\mathcal{C}$ and deforms the system into a new shape $\mathcal{C}'$. For the next step in the minimization that new shape serves as the reference shape $\mathcal{C}$ with zero strain.

The box degrees of freedom displace all particles at once and therefore have higher inertia than the particle degrees of freedom - their masses, m_p and m_q, are higher than the masses of the particle degrees of freedom. During the equilibration process we are only interested in the new equilibrium configuration - the configuration of the network after waiting an infinitely long time after the stress was applied. Here it is not important to correctly model the dynamics of the networks during a shear deformation. Consequently, we have freedom to choose m_p and m_q in order to reach the equilibrium configuration efficiently. In elastic networks we found that setting $m_p = m_q = N^2$ significantly speeds up the minimization.

During the FIRE minimization the box degrees of freedom are treated separate from the particles. While all parameters mentioned in Section 2.7.1 - T, $N_{\min}$, f_{inc}, f_{dec}, α_0, f_α, $\Delta t_{\max}$, and Δt_0 - are the same, Δt, α, N_t, P are computed separately. We found this to be beneficial because box and particles converge with different speeds. For instance, as the pressure in the simulation cell is already close to the target value it starts to fluctuate around that value frequently setting velocities to zero. If this stopping also applies to the particles that are not yet equilibrated, the algorithm only follows the gradient in each time step, which is inefficient.

Furthermore, the velocities of the box degrees of freedom are limited so that they do not exceed a value of 0.1, which is most important in the beginning of the minimization if the difference to the target stresses are high.

2

3

Nonlocal Elasticity near Jamming in Frictionless Soft Spheres

*We use simuations of frictionless soft sphere packings to identify novel con-
stitutive relations for linear elasticity near the jamming transition. By forcing
packings at varying wavelength, we directly access their transverse and lon-
gitudinal compliances. These are found to be wavelength dependent, in vio-
lation of conventional (local) linear elasticity. Crossovers in the compliances
select characteristic length scales, which signify the appearance of nonlo-
cal effects. Two of these length scales diverge as the pressure vanishes,
indicating that critical effects near jamming control the breakdown of local
elasticity. We expect these nonlocal constitutive relations to be applicable
to a wide range of weakly jammed solids, including emulsions, foams, and
granulates.*

31

3

$$F(y) = F_0 \sin(qy)$$
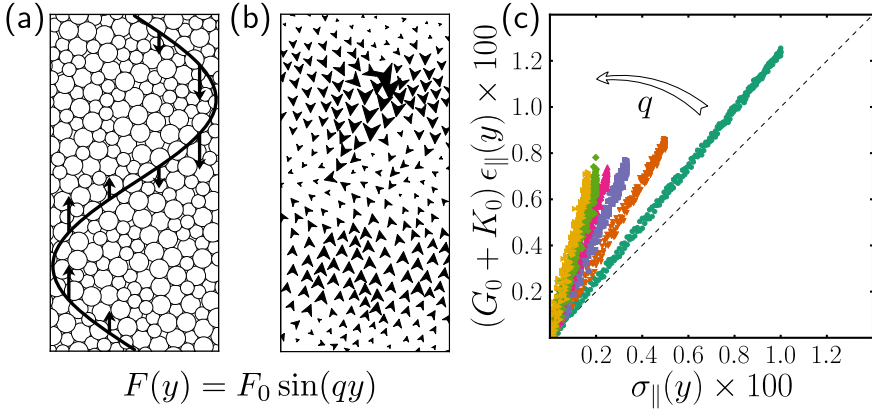
Figure 3.1: (a) Sinusoidal forcing applied to a soft sphere packing, and (b) the resulting displacements. (c) A parametric plot of the constitutive relation is linear with a slope that increases with wavenumber q, violating classical elasticity (dashed line).

3.1. *Introduction*

Classical linear elastic continuum theory is blind to structure: it contains no length scale(s) characteristic of, e.g., interparticle interactions or structural correlations [30]. As a result, the theory is only valid at asymptotically long wavelengths. While predicted displacement fields can be accurate down to a few lattice constants in ordered solids, deviations in amorphous materials are apparent over much longer distances [37, 38]. Soft sphere packings, a standard model for emulsions, foams, and granular materials, provide an important example of this effect. Response functions in simulated packings depart significantly from elasticity [11, 12, 39] when the packings are close to the (un)jamming transition at zero confining pressure p [3, 8].

Jammed solids are anomalously soft: while their shear modulus $G_0 \sim p^{1/2}$ vanishes continuously, the bulk modulus K_0 jumps discontinuously to zero at the jamming point. The vibrational density of states also displays excess low frequency modes with a characteristic scale $\omega^* \sim p^{1/2}$. Together with a linear dispersion relation, these features imply that longitudinal and transverse sound are characterized by diverging length scales $l^* \sim K_0^{1/2}/\omega^* \sim 1/p^{1/2}$ and $l_c \sim G_0^{1/2}/\omega^* \sim 1/p^{1/4}$, respectively [9, 10]. Details remain controversial, but there is consensus that the break down of classical elasticity near jamming is governed by l^* [11], l_c [12], or both [39].

In order to determine the response of jammed solids at short wavelengths, one typically gives up on continuum descriptions and turns to computationally expensive methods that resolve discrete particles, such as molecular dynamics, with resulting restrictions on accessible system sizes. Here we show that, close to jamming, continuum elasticity can be

extended to short wavelengths and the considerable computational advantages of continuum methods can be retained by using nonlocal constitutive relations, which "know about" microstructure by incorporating at least one length scale ℓ [40–43]. Our work is inspired by recent demonstrations that nonlocal effects play a central role in *rheology* near jamming [44–56], and in particular by the successful application of nonlocal models to predict unusual phenomena such as flow below the nominal yield stress [48, 57] and wide shear bands in split-bottomed Couette cells [58, 59].

Nonlocal linear elastic constitutive relations replace the usual moduli with kernels in an integral relation [41]. This can be illustrated with a classical scalar constitutive relation $\sigma = C_0 \epsilon$ in one dimension, which relates the stress σ to the strain ϵ via a modulus C_0 and holds at each position x in a volume Ω. Its nonlocal counterpart $\sigma(x) = \int_\Omega C(x - x')\epsilon(x')\,\mathrm{d}x'$ introduces a kernel $C(x)$. The kernel is *a priori* unknown, though it must vanish as $x \to \infty$ and must be an even-valued function in isotropic systems. The integral constitutive relation can be approximated with a weakly nonlocal or stress gradient form $(1 - \ell^2 \partial^2)\sigma = C_0 \epsilon$. (Strain gradient variations are also possible.) In this simpler form all nonlocal effects are quantified by the coefficient ℓ, which has units of length. To characterize and quantify nonlocal effects in a material, one must determine ℓ, or more generally its full kernel. We do so by measuring the wavenumber-dependent compliance $\widetilde{S}(q) = 1/\widetilde{C}(q)$, where $\widetilde{C}(q)$ is the Fourier transform of $C(x)$. In a tensorial theory for isotropic materials the kernel is not a scalar but a rank 4 tensor with two independent elements, which can be determined by measuring two separate compliances.

In the typical approach to nonlocal modeling, one uses data fitting to determine free parameters in a particular model. This can make it difficult to discriminate between the many available models [40–45, 47–49, 52, 54–59]. Our method more closely resembles oscillatory rheology, which gives direct access to frequency-dependent viscoelastic moduli without fitting to a model. Here we apply forcing that is periodic in space, rather than time, thereby measuring wavelength-dependent compliances [60, 61] without invoking the fluctuation-dissipation relation [62]. On the basis of our measurements, we identify two diverging length scales, growing fluctuations, and new nonlocal constitutive relations.

3.2. *Model system*

We study mixtures of N soft disks in $D = 2$ dimensions with equal numbers of large and small disks having a 1.4:1 ratio of their radii, a commonly studied model system [3, 63]. Unless noted otherwise, $N = 65{,}536$ prior to removing non-load bearing "rattlers". Contacting disks labeled i and j interact via a pair potential $V_{ij} = (1/2)k\delta_{ij}^2$, where δ_{ij} is the difference between the sum of the disks' radii and their center-to-center distance. Non-contacting disks do not interact. All results are reported in units where the spring constant

k and the small particle diameter d are equal to 1. Packings are prepared in a bi-periodic $L \times L$ cell via instantaneous quench from infinite to zero temperature using a nonlinear conjugate gradient method [36], followed by a series of small volume changes to reach a target pressure. Particle displacements are determined by inverting DN coupled linear equations involving the Hessian, the matrix of second derivatives of the potential energy with respect to the particle positions [13, 31]. The response is calculated for vanishing perturbation amplitude, so contact changes and other nonlinear effects are absent. However, recent work has shown that the Hessian accurately predicts average stress-strain curves over finite strain intervals with an extensive number of contact changes [27, 28, 64–66]. We employ the standard technique of "removing the pre-stress", which is equivalent to replacing each contact with a spring at its rest length [14, 67]. Data with the pre-stress are qualitatively similar but noisier. While all our simulations are in $D = 2$ dimensions, we expect no qualitative differences for $D \geq 3$, because the upper critical dimension for jamming is 2 [65].

3.3. *Measuring nonlocal constitutive relations*

We adapt a method developed independently by several authors – see Refs. [39, 68] and especially [60, 61], which explicitly make the connection to nonlocality. Packings are subjected to longitudinal and transverse force densities

$$\boldsymbol{f}_\parallel(y) = (0, f_\parallel)^T \sin qy \qquad (3.1)$$

$$\boldsymbol{f}_\perp(y) = (f_\perp, 0)^T \sin qy \qquad (3.2)$$

with wavenumber q. These establish changes in the stress tensor with Fourier amplitudes $\delta\widetilde{\sigma}_{yy}(q) \equiv \widetilde{\sigma}_\parallel(q) = f_\parallel/q$ and $\delta\widetilde{\sigma}_{xy}(q) \equiv \widetilde{\sigma}_\perp(q) = f_\perp/q$, respectively. We then measure the average displacement fields $\boldsymbol{u}_\parallel = (0, u_\parallel)^T$ and $\boldsymbol{u}_\perp = (u_\perp, 0)^T$. Longitudinal forcing and response are illustrated in Figure 3.1a and b. We restrict ourselves to linear response [28, 66], though application to nonlinear response and flow is possible.

In a classical and isotropic elastic continuum, a sinusoidal force density establishes a sinusoidal displacement field in phase with the forcing. Hence we can reproduce the constitutive relation by noting that a parametric plot of, e.g., the y-components of $q\,\boldsymbol{u}_\parallel(y)$ and $q^{-1}\,\boldsymbol{f}_\parallel(y)$ sweeps out the same curve as a conventional plot of strain $\epsilon_\parallel$ versus stress $\sigma_\parallel$. (This is simplest to see in a scalar 1D model, where the force density $f = -\partial\sigma$ and the strain $\epsilon = \partial u$.) Classical elasticity predicts the curve will be linear with a constant slope $K_0 + G_0$ in two dimensions. The slope is independent of q because the theory is insensitive to gradients. In Figure 3.1c we demonstrate that the second prediction fails near jamming: the slope varies with q and approaches the classical prediction (dashed line) only as $q \to 0$, when spatial gradients are weakest. This is our first main result: the elasticity of jammed packings is indeed nonlocal.
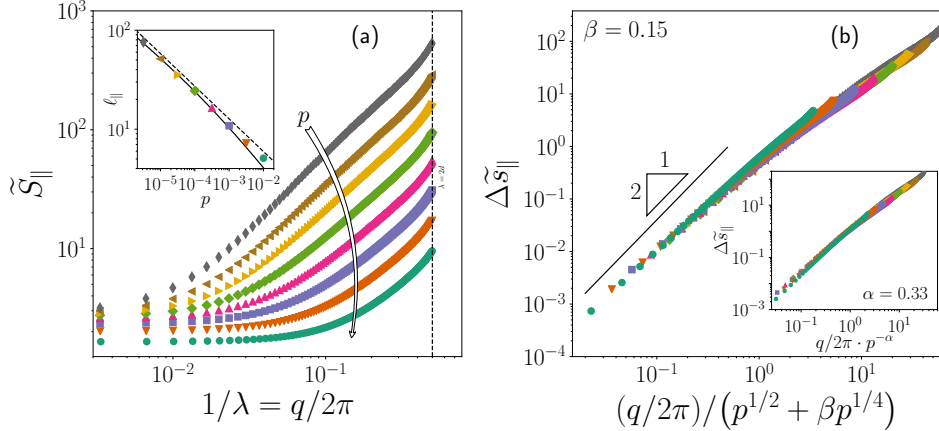
Figure 3.2: (a) Longitudinal compliance $\widetilde{S}_\parallel(q)$ versus inverse wavelength λ for pressures $10^{-5.5} \leq p \leq 10^{-2}$ in half decade steps. (inset) Nonlocal length scale determined from $\widetilde{S}_\parallel(2\pi/\ell_\parallel)/\widetilde{S}_\parallel(0) = 2$. (b) Data collapse of the excess compliance $\Delta\widetilde{s}_\parallel(q)$ for mixed (main panel) and pure power law rescaling (inset).

To quantify nonlocality, we measure the longitudinal compliance $\widetilde{S}_\parallel(q) = q^2\widetilde{u}_\parallel(q)/f_\parallel$ and transverse compliance $\widetilde{S}_\perp(q) = q^2\widetilde{u}_\perp(q)/f_\perp$ for each packing via direct Fourier transform of the displacement field. These two compliances fully determine the linear nonlocal constitutive relation [41], which in Fourier space reads $\widetilde{\sigma}_{\alpha\beta}(\boldsymbol{q}) = \widetilde{C}_{\alpha\beta\gamma\delta}(\boldsymbol{q})\,\widetilde{\epsilon}_{\gamma\delta}(\boldsymbol{q})$ (summation implied). Due to several symmetries, in isotropic materials the tensor $\widetilde{C}$ has just two independent elements [30]; these are fixed by $\widetilde{S}_\parallel$ and $\widetilde{S}_\perp$. Full expressions are given in the Supplementary Material. Because local elasticity must be recovered for spatially uniform strains, the compliances at $q = 0$ encode the bulk and shear modulus, $\widetilde{S}_\parallel(0) = 1/[K_0 + G_0]$ and $\widetilde{S}_\perp(0) = 1/G_0$. Continuity of the $q = 0$ limit is not required, but will be verified numerically.

3.4. *Mean response*

We first consider the response to longitudinal forcing. Figure 3.2 depicts $S_\parallel(q)$ for a range of pressures close to jamming and wavenumbers $2\pi/L \leq q \leq \pi/d$. Data are averaged over approximately 1,000 configurations per condition.

Each curve approaches a pressure-dependent plateau $\widetilde{S}_\parallel(0^+)$ as q tends to zero. To determine whether the limit is continuous, we measure the local compliance $\widetilde{S}_\parallel(0)$ by subjecting each packing to a uniform stress in an independent test [13]. As shown in Figure 3.2b, the excess compliance $\Delta\widetilde{s}_\parallel(q) \equiv \langle \widetilde{S}_\parallel(q)/\widetilde{S}_\parallel(0) \rangle - 1$ vanishes continuously with q, indicating a continuous limit.

3
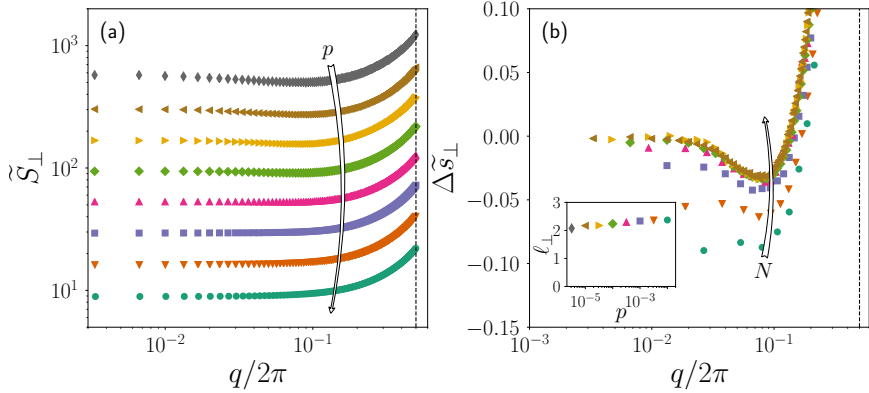
Figure 3.3: (a) The transverse compliance shows no pressure-dependent crossover for $10^{-5.5} \leq p \leq 10^{-2}$. (b) The excess compliance at low p is non-monotonic, even at large system size N. Here: $p = 10^{-4}$ and $2^{10} \leq N \leq 2^{16}$. (inset) Nonlocal length scale determined from $\widetilde{S}_\perp(2\pi/\ell_\perp)/\widetilde{S}_\perp(0) = 2$.

As q increases the compliance shows a clear pressure-dependent crossover, which selects a nonlocal length scale $\ell_\parallel$. We now show that this length diverges with pressure. To do so we demonstrate that the excess compliance $\Delta \widetilde{s}_\parallel$ collapses to a master curve when plotted versus the rescaled coordinate $q\ell_\parallel$. We first consider a simple power law ansatz $\ell_\parallel \sim 1/p^\alpha$, which gives excellent data collapse for $\alpha = 0.33$ and pressures $10^{-5.5} \leq p \leq 10^{-3}$ (Figure 3.2b, inset). The value of α is surprising insofar as it differs from the exponents $1/2$ and $1/4$ of the previously identified length scales l^* and l_c, respectively. Indeed, we show below that l^* and l_c can be identified in the fluctuations about the mean response. If one insists that $\ell_\parallel$ should approach l^* or l_c near jamming, it is also possible to obtain good data collapse of $\Delta \widetilde{s}_\parallel$ by making the alternative ansatz $1/\ell_\parallel \sim 1/l^* + \beta/l_c \sim p^{1/2} + \beta\, p^{1/4}$ – see Figure 3.2b (main panel). For $\beta = 0.15$ and $10^{-5.5} \leq p \leq 10^{-2}$, the ansatz is nearly indistinguishable from pure power law scaling (dashed and solid lines in Figure 3.2a, inset). Hence it is plausible $\ell_\parallel \to l_c$ (α approaches $1/4$) as $p \to 0$. We stress that a diverging nonlocal length implies significant nonlocal corrections to classical elasticity, regardless of the value of its exponent.

We now consider transverse forcing. Figure 3.3 plots the transverse compliance $\widetilde{S}_\perp(q)$ for a range of pressures. While the general shape of the compliance curves echoes the longitudinal case, there are several differences. First, the crossover scale $1/\ell_\perp$ is a constant on the order of the inverse particle size, independent of pressure. Hence the transverse length $\ell_\perp$ does not diverge near jamming, unlike $\ell_\parallel$. A similar p-independent crossover was noted in Ref. [39] without making the connection to nonlocality. The transverse compliance is non-monotonic, with an initial dip that appears to survive in the infinite system size limit (Figure 3.3b). Despite the

dip, the $q \to 0$ limit is again continuous, $\widetilde{S}_\perp(0^+) = \widetilde{S}_\perp(0)$. Finite size effects are stronger than in the longitudinal forcing case (not shown); they are also more dramatic than finite size effects under uniform strain [69], which can be neglected when $p \gg 1/N^2$ – which holds for all data in Figure 3.3.

3.5. *Constitutive relations*

For analytical modeling, it is often desirable to assign a functional form to the compliances. While one would like to have an accurate description of the nonlocal compliances over the whole range of q, no currently available nonlocal model correctly predicts the data of Figs 3.2 and 3.3. Fitting functions are an option, though they lack physical insight. Micromechanical models such as effective medium theory (EMT) would be preferable [70]. While we expect that EMT can predict the nonlocal transverse compliance, it fails to capture the longitudinal compliance even for spatially uniform forcing [71]. Approaches based on spatially fluctuating moduli may provide an alternative [62, 72–74].

Even in the absence of a more detailed model, it is possible to write down constitutive relations that capture essential nonlocal features of the mean response. As isotropy of the material requires $\widetilde{S}_\parallel$ and $\widetilde{S}_\perp$ to be even in q, the leading term in an expansion of the excess compliance is quadratic, as verified in Figure 3.2b. Truncating the expansion leads to weakly nonlocal, or stress gradient, constitutive relations, with a particularly simple form when the wave vector has fixed orientation:

$$(1 - \ell_\perp^2 \, \partial^2)\sigma_\perp = 2G_0 \, \epsilon_\perp \tag{3.3}$$

$$(1 - \ell_\parallel^2 \, \partial^2)\sigma_\parallel = (K_0 + G_0) \, \epsilon_\parallel \, . \tag{3.4}$$

Full expressions are available in the Supplementary Material. These relations represent a qualitative improvement over classical elasticity near jamming. Eq. (3.3) provides a good description of the transverse response over a wide range of q; note the minus sign neglects the dip in $\widetilde{S}_\perp$. Eq. (3.4) introduces the diverging length scale $\ell_\parallel$, though it misses the slow bending over of $\Delta\widetilde{s}_\parallel$ apparent in Figure 3.2b.

3.6. *Fluctuations*

It is apparent from Figure 3.1b that individual particle displacements deviate from perfect sinusoidal response. These non-affine fluctuations can be quantified by the ensemble average of the ratio

$$\mathcal{F}_\circ(q'; q) = \left| \frac{\langle u_\circ(q)|q_\circ'\rangle}{\langle u_\circ(q)|q_\circ\rangle} \right| , \tag{3.5}$$

where $\circ$ refers to $\parallel$ or $\perp$. $\mathcal{F}_\circ$ compares the projections of the DN-component displacement vector $|u_\circ(q)\rangle = \{(\boldsymbol{u}_\circ)_i\}_{i=1\ldots N}$ on sinusoids with wavenum-

3
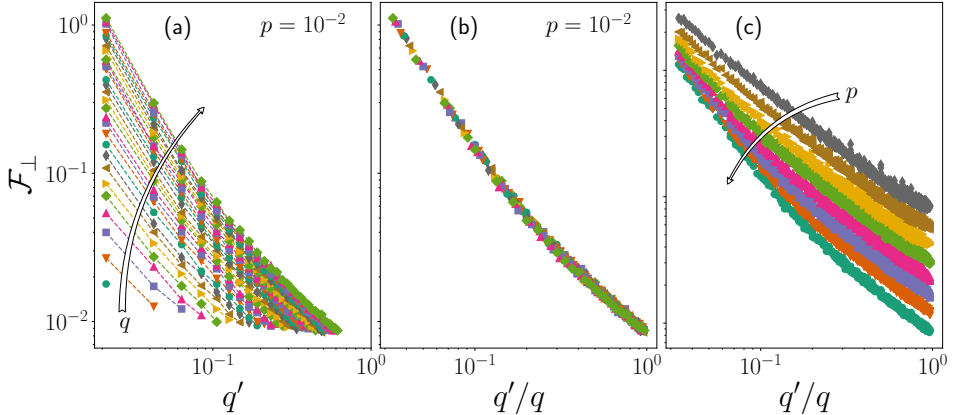
Figure 3.4: (a) Transverse Fourier transform of the response for a range of driving wavenumbers q. (b) The data shows a good collapse when the argument is rescaled linearly with the driving wavenumber. (c) The transverse Fourier transform shows a crossover wavenumber which scales with the pressure ($10^{-5.5} \leq p \leq 10^{-2}$).

bers $q' \neq q$ and q. The sinusoids' polarization matches the forcing. We first consider transverse forcing. We restrict our focus to long wavelengths $q \leq 30(2\pi/L)$, where $S_\perp$ is approximately flat, and consider only $q' < q$, where fluctuation amplitudes are largest. Figure 3.4a shows $\mathcal{F}_\perp$ for a given pressure and different wavenumbers. All curves collapse when plotted versus q'/q (Figure 3.4b). The curves for different pressures in Figure 3.4c present a pressure-dependent crossover from steep to shallow decay. The data can be collapsed further still by plotting $p^{a_\perp}\mathcal{F}_\perp$ versus $(q'/q)/p^{1/4}$, with $a_\perp \approx 0.52$ (Figure 3.5a). We conclude that transverse fluctuations are governed by the length scale l_c.

Analyzing low-q fluctuations under longitudinal forcing is more difficult due to the vanishing crossover near jamming. As a compromise we vary q' and q for $q' < q \leq 10(2\pi/L)$, where the excess compliance $\Delta\widetilde{s}_\parallel$ is approximately quadratic for all accessed pressures. These fluctuations have a more complex dependence on q, as evidenced by slight but systematic spread in the data when plotted versus q'/q – see Figure 3.5b (inset). Nevertheless, there is again a clear p-dependent crossover, which can be collapsed by plotting $p^{a_\parallel}\mathcal{F}_\parallel$ versus $(q'/q)/p^{1/2}$, with $a_\parallel \approx 0.57$ (main panel). While the collapse is less convincing than $\mathcal{F}_\perp$, it suggests that longitudinal fluctuations are governed by the length scale l^*.

For both types of forcing, we observe data collapse only for sufficiently low q'. The restriction to $q' < q$ is strictly necessary in the longitudinal case; data fall off the master curve rapidly for larger q'. In the transverse case the fall off comes later and more gradually. We note that prior work has related l^* [11], l_c [12], or both [39] to (deviations from) classical elastic Green's functions [11, 12, 39].
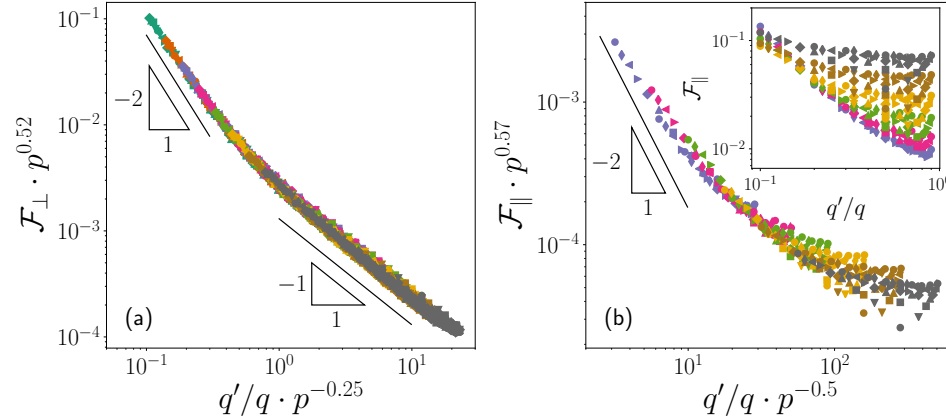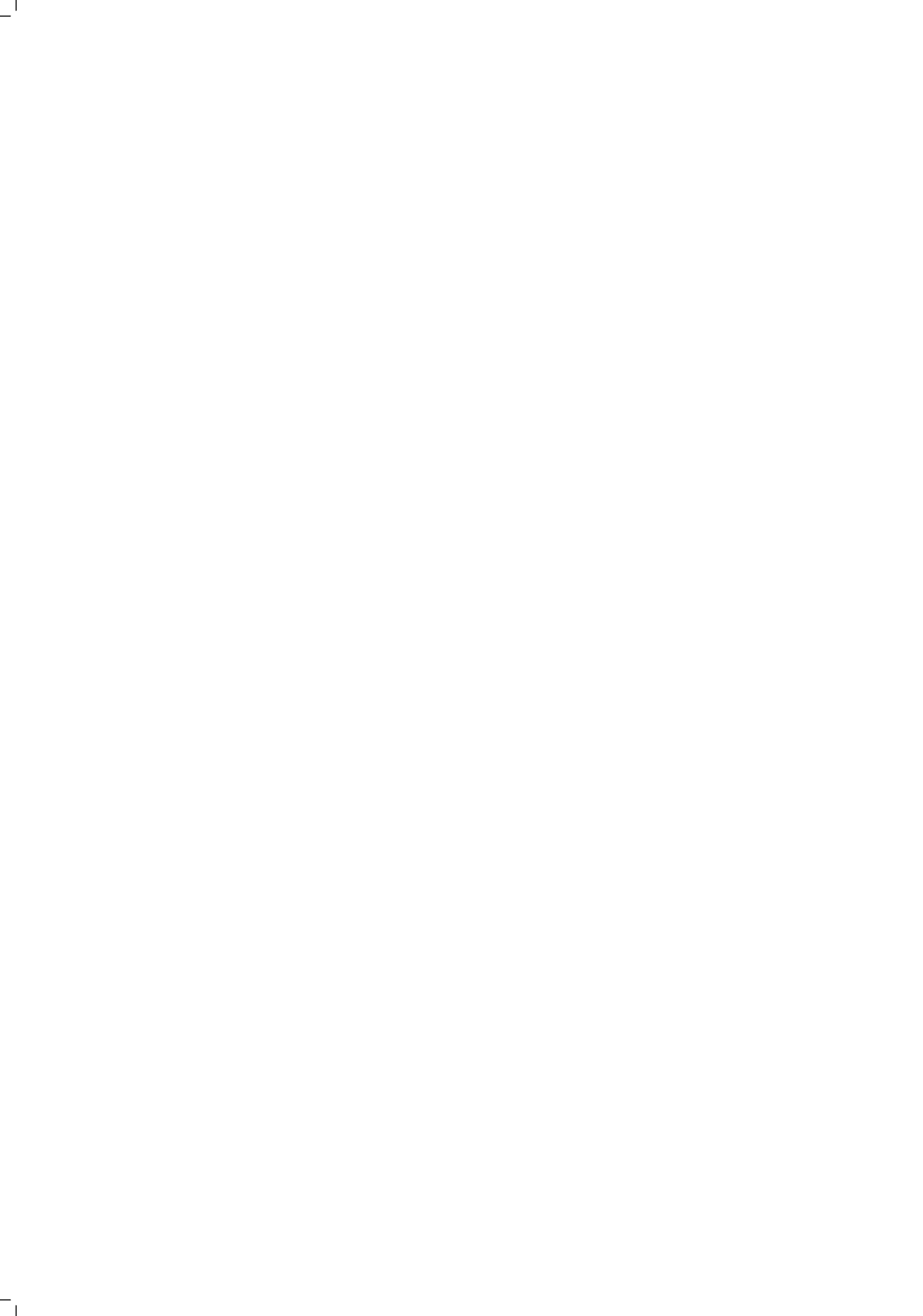
Figure 3.5: (a) Data collapse of the transverse Fourier transform after rescaling with q' with $p^{-0.25}$. (b) The longitudinal Fourier spectrum shows similar collapse before (inset) and after (main panel) rescaling q' with $p^{-0.5}$.

3.7. *Conclusions*

We have demonstrated novel constitutive relations that improve on classical elasticity near jamming by capturing the appearance of a diverging length scale within a continuum description. The divergence scales with the distance to jamming, indicating that critical effects enhance deviations from local elasticity. Nonlocal effects are stronger in deformations involving compression, as reflected in the distinct length scales $\ell_\perp$ and $\ell_\parallel$; the former remains finite, while the latter diverges. Fluctuations about the mean nonlocal response are governed by two distinct diverging length scales.

The sinusoidal forcing technique used here is not restricted to soft spheres – it can be used to test for nonlocal effects in a wide range of materials. It is straightforward to implement numerically and can also be implemented in experimental systems that allow for forcing in the bulk, such as thermoresponsive microgels and granular monolayers. In the jamming context, obvious extensions include acoustic dispersion relations [67], nonlinear forcing [28], and steady flow [75, 76].

4

Rigidity of Hypostatic Random Spring Networks

Networks below a critical connectivity of four contacts per node are hypostatic, and according to Maxwell counting they do not resist a shear deformations. Their shear modulus is zero. We show examples in which these systems are rigidified by pre-stress and bending interactions in two different network models. We find striking similarities in the density of states for both "perturbing fields" and systems. We explain the most outstanding feature of the density of states using variational arguments and connect it to the shear response.

4.1. *Introduction*

Here we focus on the rigidfication of hypostatic networks. Following the Maxwell counting, a network with an average connectivity below the isostatic connectivity $z_c = 4$ in 2D or $z_c = 6$ in 3D is floppy. The shear/bulk modulus therefore vanishes, because the system can accomodate bulk or shear deformations by displacing along floppy modes. These floppy modes consist of tangential relative motion of nodes in contact, which keeps their bond length unchanged. As a result no springs in the networks are compressed/stretched so the floppy mode does not cost energy.

The isostatic state at z_c acts as a non-equilibrium critical state that determines the elastic response in its vicinity. Above the isostatic point the response is dominated by an abundance of anomalous low-frequency modes that resemble floppy-modes. Below the isostatic point the system has a number of floppy modes proportional to $-\Delta z$, the average number of bonds per particle below z_c. The key observation in this chapter is that constraining these floppy modes, so that they now cost energy, can make the system rigid even when it is hypostatic. We will discuss several ways to constrain floppy motion.

An energetic cost of tangential motion is common in nature. In a network bonds usually cannot freely rotate around the nodes they are attached to, or the whole network is under tension due to external stresses. These
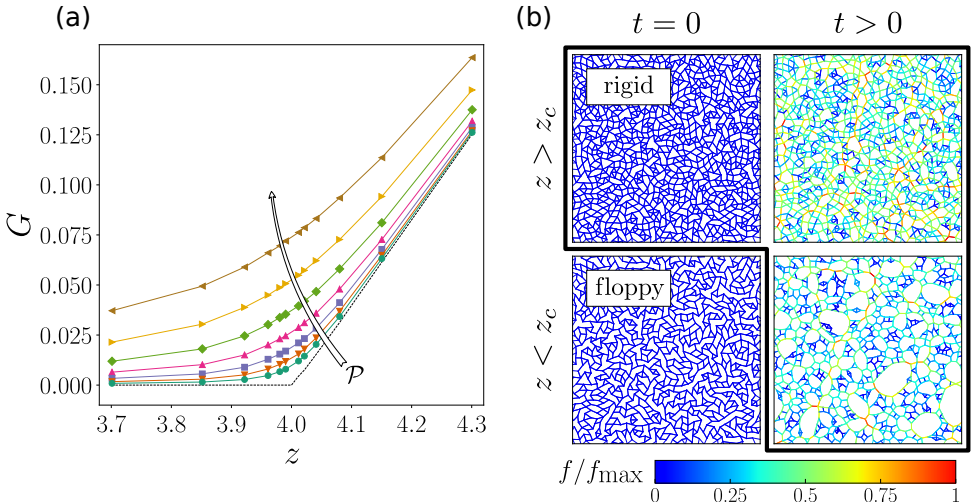
Figure 4.1: (a) Shear modulus of a system subjected to a perturbing field. If $z < 4$ for an unperturbed system then $G = 0$ - the system is floppy. The networks become rigid under the influence of a perturbing field. $\mathcal{P}$ is the control parameter. The dashed line shows the shear modulus for zero perturbation. (b) (Left column) Hyperstatic and hypostatic network without tension. While the hypostatic network is initially floppy it becomes rigid as tension is applied (right column).

additional interactions that constrain the system act as "perturbing" fields that drive the system away from the critical point. This process is illustrated in Figure 4.1a with the shear modulus of a randomly cut network above and below the critical point. The dashed line shows the system without perturbation. If the system is peturbed, here in the form of a stretching of the whole network, the vanishing of G is avoided. The shear modulus increases with perturbation strength $\mathcal{P}$, and below and at the transition it is now finite - the system remains rigid below z_c.

In this chapter we investigate three cases in which networks are rigidified by a perturbing field. First, we consider RC networks below and above isostaticity and investigate their behavior as they are set under tension t. The second part also consists of RC networks, but we add bond bending interactions whose strength is tuned by the bending stiffness κ. The last example consists of a model for networks consisting of semiflexible rods - the Mikado model. Here the networks are also rigid because of the presence of bending interactions, while the network geometry and topology is more complex.

4.2. *RC Networks under Tension*

In this section networks initially without tension are stretched such that a certain target tension t is reached. We start from an RC network with $N = 1024$ nodes and connectivity z. We then minimize the potential energy under the constraint that the pressure is $p = -t$ while the normal stress difference vanishes, $q = 0$. The stress tensor of the systems that are generated has the form

$$\hat{\sigma} = \begin{pmatrix} \sigma_{xx} & \sigma_{xy} \\ \sigma_{xy} & \sigma_{yy} \end{pmatrix} \approx \begin{pmatrix} -t & 0 \\ 0 & -t \end{pmatrix} . \tag{4.1}$$

The off-diagonal element σ_{xy} vanishes in large systems or in an ensemble. For each system we first target a high tension of $t = \sqrt{10} \cdot 10^{-1}$ and then decrease it until we reach $t = 10^{-5}$. Figure 4.1b shows two snapshots of the simulations for two connectivities above and below the isostatic point. The left column contains the two systems without tension. The network above isostaticity is rigid while the hypostatic counterpart is floppy. When the network is expanded (the expansion itself is not shown) the springs are set under tension. The tangential motion that initially did not cost energy is now constrained - the initially floppy network becomes rigid.

4.2.1. *Shear Response*

From hyperstatic unstressed networks we know that the shear modulus is finite and scales with the contact number, $G \sim \Delta z^\mu$. In PD networks and in effective medium theory for bond diluted triangular networks, one finds $\mu = 1$ [77]. In the case of RC networks, previous numerical studies [77, 78] found $\mu \approx 1.4$. In this section we find $\mu = 1$. In [21] the authors argue that
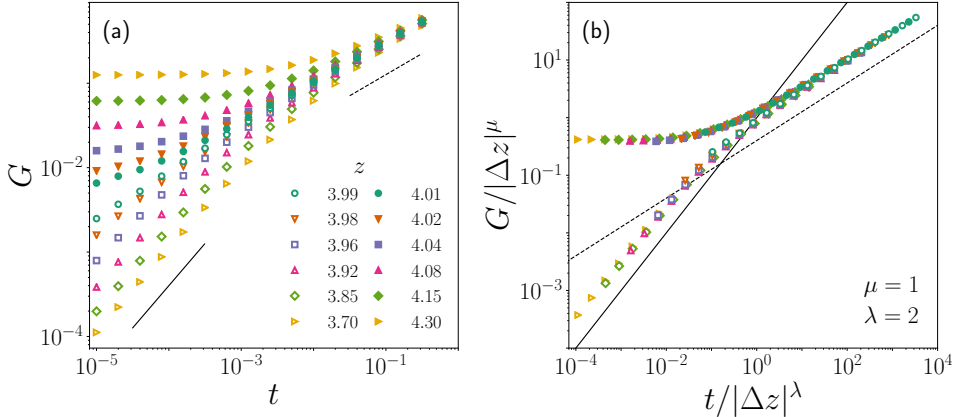
Figure 4.2: (a) The shear modulus of RC networks above (full symbols) and below (open symbols) the isostatic point. While the shear modulus has a plateau for $z > z_c$ it vanishes below isostaticity. The collapse in (b) shows a critical length tension scale which vanishes with Δz^2. The graph also shows usual scaling $G \sim \Delta z$ above the isostatic point. In both figures the solid line has slope one and the dashed line slope $1/2$.

the cutting protocol introduced in Chapter 2 promotes mean field behavior by supressing fluctuations in the local coordination number.

Hypostatic networks have a zero shear modulus $G = 0$. We therefore know that

$$G_+(t \to 0) \to G_0 \sim \Delta z^{\mu} \quad \text{and} \quad G_-(t \to 0) \to 0 \tag{4.2}$$

where G_+ and G_- denote the shear modulus of hyperstatic and hypostatic networks, respectively. Figure 4.2a shows the shear modulus for finite tensions. For small enough tensions G_- increases linearly with a pre-factor that depends on $|\Delta z|$, while G_+ has a plateau. Above some connectivity-dependent tension threshold both become comparable and increase with the square root of the tension. This situation is summarized in Figure 4.3, which depicts the typical behavior of a system close to a critical point.

The response can be split into three regimes. As the tension is small and the system is still close the critical point, G shows critical scaling and its two branches are separated into two regimes (regime I and II). At a characteristic tension, the two branches merge, lose their dependence on the connectivity, and show a square root dependence on the tension (regime III).

Inspired by these observations, we make a scaling ansatz using the distance to isostaticity $|\Delta z|$ and the tension:

$$G_{\pm} = |\Delta z|^{\mu} \mathcal{G}_{\pm} \left(\frac{t}{|\Delta z|^{\lambda}} \right). \tag{4.3}$$

Both branches of the shear modulus have to fulfill the zero tension limit shown in equation (4.2). With the perturbing field ($t \neq 0$) the shear modulus
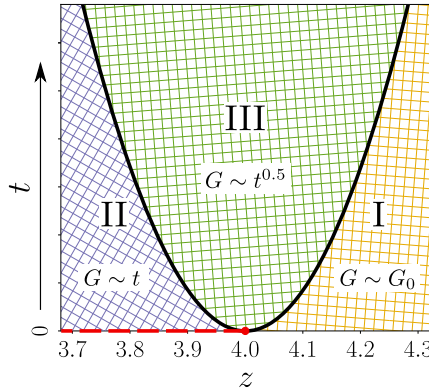
Figure 4.3: The shear response can be devided into three regimes separated by the isostatic point (red dot) and a characteristic tension (shown as solid black line). The dashed red line indicates where the system is floppy.

has to be finite at $\Delta z = 0$ (see Figure 4.1a, 4.3). These requirements are fulfilled if the branches take the following form:

$$\mathcal{G}_+(\tau) \sim \begin{cases} \text{const} & \tau \ll 1 \\ \tau^{\mu/\lambda} & \tau \gg 1 \end{cases} \tag{4.4}$$

and

$$\mathcal{G}_-(\tau) \sim \begin{cases} \tau^\alpha & \tau \ll 1 \\ \tau^{\mu/\lambda} & \tau \gg 1 \end{cases} \tag{4.5}$$

where $\tau = t/|\Delta z|^\lambda$. Figure 4.2b shows a collapse of the data in 4.2a. A critical scaling collapse of these sorts gives precise meaning to the assertion in the Introduction that proximity to the isostatic point governs the response in its vicinity. The plot shows that the data best collapses for $\lambda = 2$ and $\mu = 1$. This implies that $\alpha = 1$ in the hypostatic branch if $\tau \ll 1$ and that G goes as $\tau^{0.5}$ for $\tau \gg 1$. The hyperstatic branch is the same as the hypostatic for large τ but approaches a plateau for $\tau \to 0$.

The fact that the exponent $\mu = 1$ is expected from the behavior of hyperstatic networks at $\tau = 0$. We measure that the crossover exponent $\lambda = 2$ which, the exponent α and together with the scaling analysis above, explains the behavior of G for all values of t on both branches of the scaling function. The last missing piece is to understand the values of the exponents α and λ. In order to do this, we recall that in Chapter 2 we introduced an expression for G in terms of eigenvalues and eigenvectors of the extended Hessian:

$$\frac{1}{G} = \sum_i \frac{\Lambda_i^2}{\omega_i^2} \approx \int_0^\infty \frac{D(\omega)\Lambda^2(\omega)}{\omega^2} \, \mathrm{d}\omega \,. \tag{4.6}$$

By introducing the density of states $D(\omega)$, we approximate the sum as an integral, which is an approximation for large systems. In the following section

we measure the product of the density of states and the coupling factor Λ^2. We rationalize the shape of the density of states and show how it explains the scaling of G. If not stated otherwise we assume that Λ^2 is constant and does not scale with Δz. This assumption is based on the numerical results from 5.

4.2.2. *Density of States*

In standard solids one finds Debye behavior for low eigenfrequencies - the density of states $D(\omega)$ has an intial form of ω^{d-1} (d the dimension of the system). In the case of high coordination numbers one also observes this behavior in RC networks. However, as one reduces z, the frequency window in which one can observe Debye scaling vanishes and one observes instead a sudden increase in the density of states followed by a plateau. This sudden increase happens at a characteristic frequency ω^* that vanishes linearly with the excess connectivity Δz on both sides of the isostatic point [3, 79]. However, hypostatic networks also have a delta peak at zero frequency containing the floppy modes of the system. The integrated weight of this peak vanishes linearly with decreasing $|\Delta z|$.

In Figures 4.4 and 4.5 we report - to our knowledge for the first time - the density of states of RC networks under tension. For constant tension and varying connectivity, the peak in the density of states does not shift but changes height. Figure 4.4b shows that the height of the peak is proportional to $|\Delta z|$, as evidenced by the data collapse when plotting $D\Lambda^2/|\Delta z|$ vs. ω. Figure 4.5a shows the density of states for connectivity $z = 3.7$ and a range of applied tension. It has a dominant peak that shifts to higher frequencies and becomes broader as the tension grows, while the high frequency regime is only weakly influenced. Figure 4.5b shows that the low frequency peak can be collapsed by plotting $D\Lambda^2 \cdot t^{0.5}$ vs. $\omega/t^{0.5}$.

The peak in the density of states is connected to the δ-peak at $\omega = 0$ in the density of states of the unstressed network. Floppy modes consist purely of tangential motion, which neither stretches nor compresses springs. With an applied tension, however, tangential motion is constrained and acquires an energy cost. Consequently, the modes, which are floppy in the unstressed system, are "pulled out" and form a peak at finite frequency. The area below the peak in Figure 4.4 is therefore expected to be proportional to the number of these modes, which is proportional to $|\Delta z|$. To understand why the peak shifts as shown in Figure 4.5, we make a variational argument in which we construct trial modes for the modes which form the peak.

Consider a network with applied tension t. The length of the springs is not equal to their rest length and we measure that there are no floppy modes. We can construct trial modes for the low frequency regime by taking away the tension in this network. This can be achieved by setting the rest length of the springs equal to their current length, so the positions of the nodes are not changed in the process. Now the "tension-free network" has
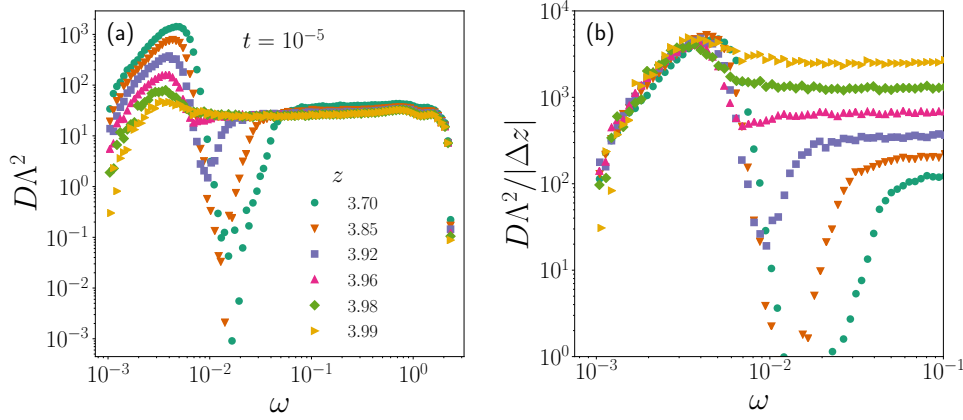
Figure 4.4: (a) The density of states for varying z below isostaticity and a tension of $t = 10^{-5}$. The curves feature a peak which becomes more dominant when $|\Delta z|$ is increased. The collapse in (b) shows that the peak height is proportional to Δz.

floppy modes that we employ as trial modes. These $n = N|\Delta z|/2$ trial modes consist only of tangential motion $\Delta u_\perp$. The energy cost of such a mode in terms of $\Delta u_\parallel$ and $\Delta u_\perp$ has the following form

$$\Delta U = \frac{1}{2} \sum_{\langle ij \rangle} \left(k \Delta u_{\parallel,ij}^2 + \frac{f_{ij}}{\ell_{ij}} \Delta u_{\perp,ij}^2 \right) . \tag{4.7}$$

ℓ_{ij} is the spring length and f_{ij} the force on the contact. Because our trial modes do not have parallel motion, the first term in parenthesis vanishes. We write

$$\Delta U = \sum_{\langle ij \rangle} \frac{f_{ij}}{\ell_{ij}} \Delta u_{\perp,ij}^2 \sim \frac{f}{\ell} \Delta u_\perp^2 \tag{4.8}$$

where f, ℓ, and $\Delta u_\perp$ are average values. The average force is proportional to the applied tension. Furthermore, we know that $\Delta u_\perp$ is independent of Δz, which was rationalized in [10, 80] and numerically confirmed in [20]. Consequently, the trial modes we have constructed have a typical energy that scales as

$$\Delta U \sim \frac{f}{\ell} \Delta u_\perp^2 \sim t . \tag{4.9}$$

We assume there exists a pre-factor a for which $\Delta U \leq E = at$ is satisfied. As described in [10] we now invoke a generalization of the variational priniciple familiar from quantum mechanics [81]. If we have a set of n trial modes with energy $\Delta U \leq E$, then there are at least $n/2$ eigenmodes with energy $\Delta U' \leq 2E$.

Following the considerations above we can conclude that there are at least $N|\Delta z|/4$ eigenmodes which have eigenfrequencies of

$$\omega_p \leq \sqrt{2E} = \sqrt{2a} \cdot t^{0.5} \sim t^{0.5} . \tag{4.10}$$
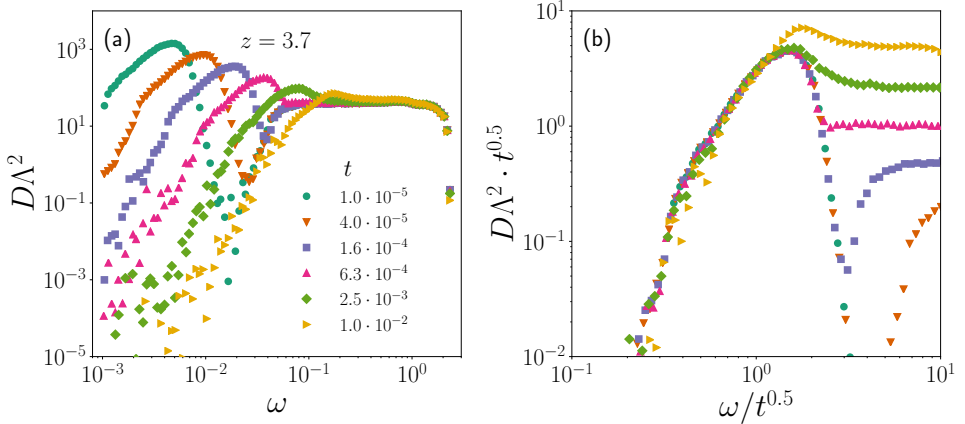
Figure 4.5: (a) The density of states for random spring networks below isostaticity for $z = 3.7$ and varying tension. The peak shifts to higher frequencies as the tension is increased. (b) The same curves as in (a) but collapsed onto a master curve.

Inspired by the findings above, we approximate the density of states with a window function for $\omega^* < \omega < \omega_0 \sim \mathcal{O}(\sqrt{k})$ plus a δ-peak with height equal to the area below the peak in the density of states, $|\Delta z|$. The shear modulus can now be expressed as

$$
\begin{aligned}
\frac{1}{G} &\sim \int_0^\infty \frac{D(\omega)\Lambda^2(\omega)}{\omega^2}\, \mathrm{d}\omega \\
&\sim |\Delta z|\Theta(-\Delta z) \int_0^\infty \frac{\delta(\omega - \omega_p)}{\omega^2}\, \mathrm{d}\omega + \int_{\omega^*}^1 \frac{1}{\omega^2}\, \mathrm{d}\omega \\
\frac{1}{G} &\sim \frac{|\Delta z|\Theta(-\Delta z)}{\omega_p^2} + \frac{1}{\omega^*} \quad \Leftrightarrow \quad G \sim \frac{t\omega^*}{|\Delta z|\omega^*\Theta(-\Delta z) + t}\ .
\end{aligned}
\tag{4.11}
$$

The Heaviside function Θ was introduced to distinguish between the hyperstatic and hypostatic case. If $-\Delta z > 0$ the peak is "switched on" and not present when $-\Delta z < 0$. For hypostatic networks we find $G_- \sim t/|\Delta z|$ as $t \to 0$, which explains the value $\alpha = 1$. For hyperstatic networks $G_+ \sim \omega^* \sim \Delta z$. The two branches meet when

$$
\frac{G_-}{G_+} \sim \frac{t}{|\Delta z|^2} \sim \mathcal{O}(1) \quad \rightarrow \quad t^* \sim |\Delta z|^2\ .
\tag{4.12}
$$

The crossover tension $t^* \sim \Delta z^\lambda$ with $\lambda = 2$ is the same as in the scaling functions (4.4) and (4.5). Now with the variational argument above we understand the origin of the exponent λ. As the tension is small enough there are modes with a typical frequency of $\omega_p \sim t^{0.5}$, which can be approximated by floppy modes. As the tension increases other modes with typical frequency ω^* dominate - we see that the peak in the density of states merges with the high frequency plateau (see Figure 4.5). We find that the behavior
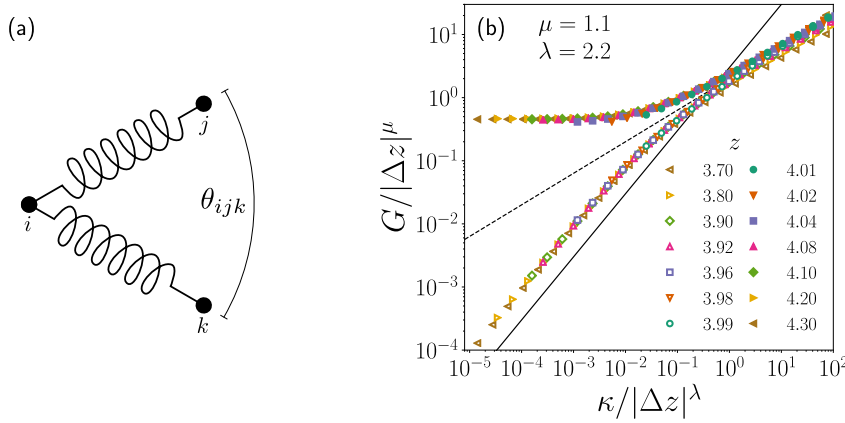
Figure 4.6: (a) Two contacts ij and ik which are adjacent on node i interact via bending interactions. (b) Shear response of RC networks with bending interactions above and below isostaticity. The solid line has slope one and the dashed line slope $1/2$.

of the shear modulus can be understood by considering the two outstanding features in the density of states, the peak and the plateau. These two features, in turn, can be understood by variational arguments.

4.3. *RC Networks with Bending Interaction*

Another example of rigid networks below isostaticity are networks which also include three body interactions such as bending. At first glance these systems seem unrelated, since the interaction potentials are dissimilar. However, as we will show, rigidification by tension and bending have many similarities.

Bending interactions add an extra term to the elastic energy proportional to the bending stiffness κ

$$U = \frac{k}{2} \sum_{\langle ij \rangle} (\delta \ell_{ij})^2 + \frac{\kappa}{2} \sum_{\langle ijk \rangle} (\delta \theta_{ijk})^2 \,. \tag{4.13}$$

$\delta \theta_{ijk}$ is the change in the angle between two contacts ij and ik that are adjacent on node i (see Figure 4.6a).

In Figure 4.6b we show the shear modulus as a function of κ for networks with $N = 32768$ nodes above and below isostaticity. The ensemble consists of 50 systems per condition. The plot shows that there is striking similarity to the shear response in networks under tension. Following the same arguments that were used to derive the scaling function for networks under tension (equation (4.4) and (4.5)) we collapse the shear response us-
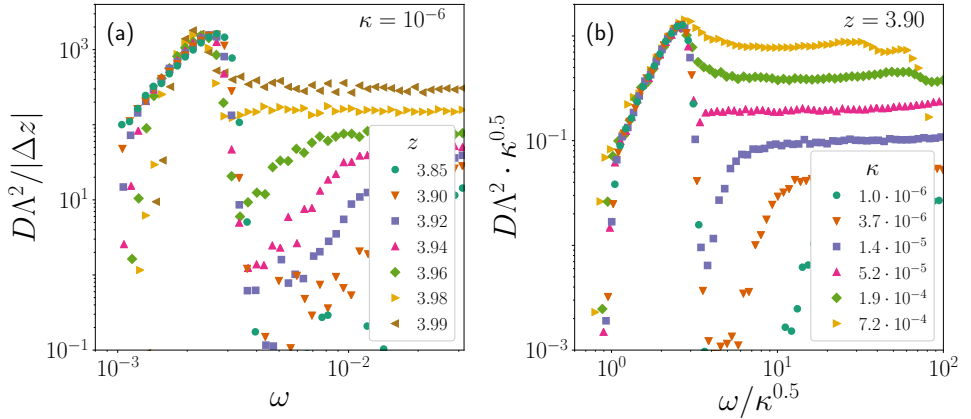
Figure 4.7: (a) Density of states for bending stiffness $\kappa = 10^{-6}$ and varying connectivity. (b) Density of states for connectivity $z = 3.9$ and varying κ.

ing the scaling function

$$G_+(\kappa) \sim \begin{cases} \Delta z^\mu & \kappa' \ll 1 \\ \kappa'^{\,\mu/\lambda} & \kappa' \gg 1 \end{cases}$$

$$G_-(\kappa) \sim \begin{cases} \kappa'/\Delta z^\mu & \kappa' \ll 1 \\ \kappa'^{\,\mu/\lambda} & \kappa' \gg 1 \end{cases} \tag{4.14}$$

where $\kappa' = \kappa/\Delta z^\lambda$. We find the exponents $\mu = 1.1$, which stems from the limit $\kappa \to 0$, and $\lambda = 2.2$. To understand the exponent λ we consider the density of states as we did in Section 4.2.2.

Figure 4.7a and b show the density of states for an ensemble of 1000 per condition. The networks consist of 1024 nodes. The data is again collapsed with connectivity $|\Delta z|$ (a) and bending stiffness (b). We find also here a dominant peak followed by a plateau. The peak can be described with the same exponents that govern the case of tension. The area below the peak is proportional to the number of floppy modes of the hypostatic network if $\kappa = 0$. To understand the shift in the peak (Figure 4.7b) we construct trial modes in the same way as in the previous section. The energy cost of these trial modes for finite bending stiffness scales as

$$\Delta U \sim \kappa(\delta\theta)^2 . \tag{4.15}$$

If we assume that the relative displacements of two nodes that interact via bending are not correlated, we can write $\delta\theta \sim \Delta u_\perp/\ell$ and therefore

$$\Delta U \sim \kappa \left(\frac{\Delta u_\perp}{\ell}\right)^2 \sim \frac{\kappa}{\ell^2} . \tag{4.16}$$

Note that this expression is equivalent to (4.9) under the exchange $t \leftrightarrow \kappa/\ell^2$.
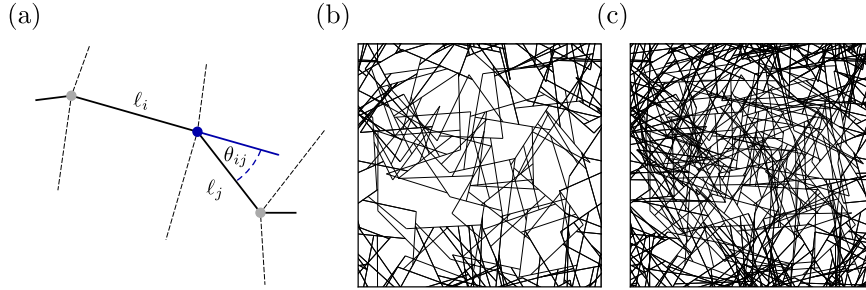
Figure 4.8: (a) One filament in a Mikado network intersected by three other filaments (dashed lines). Mikado networks with average distance between crosslinks $\ell_s \approx 7.84 \cdot 10^{-2}$ (b) and $\ell_s \approx 3.65 \cdot 10^{-2}$ (c).

The average length of the springs does not scale with connectivity, so the shift in the peak is independent of $|\Delta z|$.

We see that bending interactions and tension in hypostatic networks have similar effects on their shear response. In both cases we find an initial linear increase of G with the perturbation strength and the two exponents μ and λ are similar. The scaling function (4.14) has previously been derived in [77, 82] using effective medium theory. The derivation presented here needs less mathematical effort, is based on variational arguments, and illuminates the connection between moduli and modes.

4.4. *Mikado Networks*

Mikado networks [23, 25, 83, 84] are a simple model for semiflexible fiber networks. These networks are present in nature, they constitute the cytoskeleton of cells or the extracellular matrix and are found in materials like wood. They also play an important role in technology, where they can be used to model polymers. Semiflexible networks consist of elongated filaments, which have a bending stiffness that is high enough to withstand thermal fluctuations [25] that would otherwise cause the filament to crumple into a coil.

Mikado networks consist of N monodisperse filaments of length ℓ, which are deposited randomly in a biperiodic square system of linear size L. Their position $\boldsymbol{r}$ with components $r_x, r_y \in [0, L)$ and orientation $\phi \in [0, \pi)$ are both drawn from a uniform probability distribution. If, during the deposition process, two filaments intersect, they form a crosslink around which the rods can freely rotate. The crosslinks cannot be broken. In the initial condition just after deposition, the rods are all straight lines divided by the crosslinks into segments of length ℓ_i. If a force or displacement is applied these segments store energy via stretching and bending. The total energy

of the system is

$$U = \frac{\mu}{2} \sum_i \frac{(\delta \ell_i)^2}{\ell_i} + \frac{\kappa}{2} \sum_{ij} \frac{(\delta \theta_{ij})^2}{\ell_{ij}} \tag{4.17}$$

with the stretching stiffness μ (not to be confused with the exponent μ used elsewhere), bending stiffness κ, the angle θ_{ij} between two neighboring sections on the same rod (see Figure 4.8), and the average length of the two segments ℓ_{ij}. The average length of all line segments in the system is ℓ_s. The filament length ℓ serves as the unit of length. The crosslink density $\rho = N\ell_f/V$ is inversely proportional to the average segment length, $\rho \sim 1/\ell_s$. The average number of crosslinks per rod is $n = \ell_f \rho - 1$. For very low crosslink densities, the networks do not percolate, they only start to span the whole system at the conductivity percolation transition with a crosslink density of $\rho \approx 5.42$ [85]. However, at this density the networks still cannot resist any deformation because of rotation at the crosslinks. This changes at the rigidity percolation transition at $\rho \approx 5.93$ [86]. Here the networks can resist deformations provided the rods have a finite bending stiffness κ.

The following section shows that the rigidity of Mikado networks, although superficially very different, can be described with the same tools that were introduced in the sections above. After giving background on the shear response, which has already been discussed extensively in the literature [23, 84, 87, 88], we show novel data for the density of states and connect it to the shear response in the same manner as in the previous sections.

4.4.1. *Connection to Random Spring Networks*

By construction a Mikado network is composed of rods that form crosslinks. In the following we want to leave this picture and return to a picture closer to random spring networks. We consider the crosslinks as nodes and the filament segments as springs. Most nodes have four segments - two on each of the rods that originally formed the crosslink. If a crosslink is lying at the end of a rod or even at the ends of both rods that form it, the corresponding node has three or two contacts, respectively. Consequently, the coordination number of a Mikado network is always below z_c. With vanishing bending stiffness, the network is therfore not able to resist a shear or bulk deformation. Simple counting reveals that there is a number of floppy modes equal to the number of rods [88].

Note that in spring networks we focus on the distance to the isostatic point $|\Delta z|$, which is equal to the fraction of vibrational modes which are floppy. We construct $|\Delta z|$ in the same way for Mikado networks. The total number of modes is equal to the number of degrees of freedom in the system. That is

$$N_{\text{dof}} = 2N(\ell_f \rho - 1) = 2N \left(\frac{N\ell_f^2}{V} - 1 \right), \tag{4.18}$$
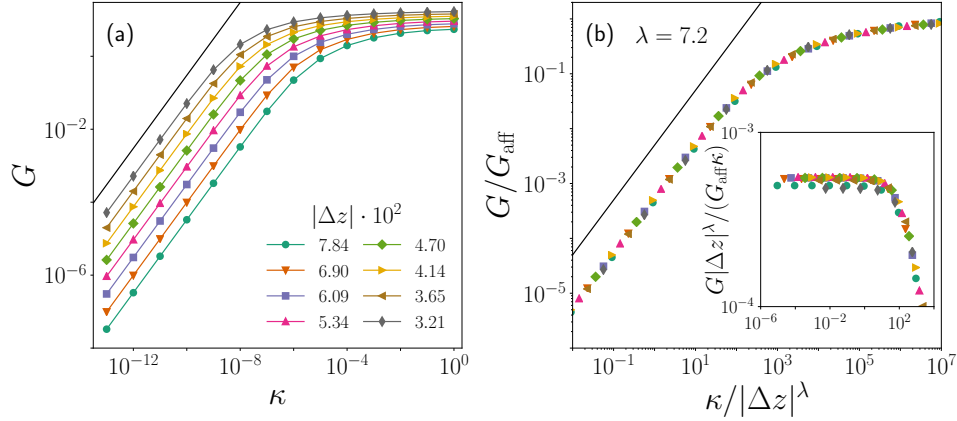
Figure 4.9: (a) For high Δz or low κ the networks respond non-affine and $G \sim \kappa$ (the solid line has slope one). The curves eventually crossover into the affine regime where the modulus becomes independent of κ. (b) Collapse of the curves from (a) with $|\Delta z|$. The inset shows the collapse in the non-affine regime in detail.

the number of crosslinks per rod times the number of rods. The factor of two stems from the dimensionality of the system. The fraction of floppy modes is

$$\frac{N}{N_{\text{dof}}} = \frac{1}{2 \left(N\ell_f^2/V - 1 \right)} \approx \frac{1}{\rho\ell_f} \sim \frac{\ell_s}{\ell_f} = -\Delta z \,. \tag{4.19}$$

We applied an approximation for the limit of large N to simplify the definition of Δz. In the vicinity of the isostatic point $N\ell_f^2/V$ becomes large, so Δz does still approach the fraction of floppy modes. Expression (4.19) shows that the Mikado network can, by construction, not reach the isostatic point. It approaches $-\Delta z \to 0$ as the average distance between two crosslinks vanishes, $\ell_s \to 0$.

Our simulations are performed in two-dimensional square cells of linear length $L = 3\ell_f$. We vary the crosslink density with the number of rods - we report the average crosslink densities of systems with the same number of rods. The second parameter that we tune is the bending stiffness.

4.4.2. *Shear Response*

Figure 4.9a and b show the shear modulus of Mikado networks with $|\Delta z| \in [7.84 \cdot 10^{-2}, 3.21 \cdot 10^{-2}]$ and κ ranging over 13 orders of magnitude. The ensemble consists of 100 systems per condition. The figures show that the shear response can be divided into two regimes. For high $|\Delta z|$ and low bending stiffness the shear modulus grows linearly with κ. In the vicinity of the isostatic point or as κ is increased the response eventually approaches a plateau where the shear modulus becomes independent of κ. In [84] the authors derive an expression for the modulus under the assumption that

the response is affine:

$$G_{\text{aff}} \approx \frac{\pi}{16} \frac{\mu}{\ell_f} \left(\frac{\ell_f}{\ell_s} + \frac{\ell_s}{\ell_f} - 3 \right) \tag{4.20}$$

The expression is independent of κ and, for high crosslink densities $1/\ell_s \to \infty$, proportional to the crosslink density. It diverges at the isostatic point:

$$G_{\text{aff}} \approx \frac{\pi}{16} \frac{\mu}{\ell_f} \cdot \frac{\ell_f}{\ell_s} \sim \frac{\pi}{16} \frac{\mu}{\ell_f \Delta z} . \tag{4.21}$$

4.9b shows the shear modulus in units of the affine modulus (4.20) as a function of $\kappa/|\Delta z|^\lambda$, which makes all graphs in 4.9a collapse, in agreement with previous results [84]. Since the plateau collapses with the affine modulus, the regime where $\kappa \gg 10|\Delta z|^\lambda$ is identified as the affine regime [84]. If $\kappa \ll 10|\Delta z|^\lambda$, the response of the network is non-affine. Here the bending interactions dominate the response. The crossover exponent is $\lambda = 7.2$.

We can see that the shear response is similar to the two previous examples. With no perturbing field, $\kappa = 0$, the shear modulus vanishes. With a finite bending stiffness, which is small enough so that the response is dominated by bending, we find a linear relation between G and κ. In case of RC networks we find a crossover strain λ at which G goes with the square root of the perturbation strength. We do not measure such a regime in the Mikado model, however, we also find a crossover strain in the shear response. The shear response crosses over into an affine regime where the shear modulus does not depend on the strength of the perturbing field. Furthermore, compared to RC networks, the value of λ is significantly larger.

4.4.3. *Density of States*
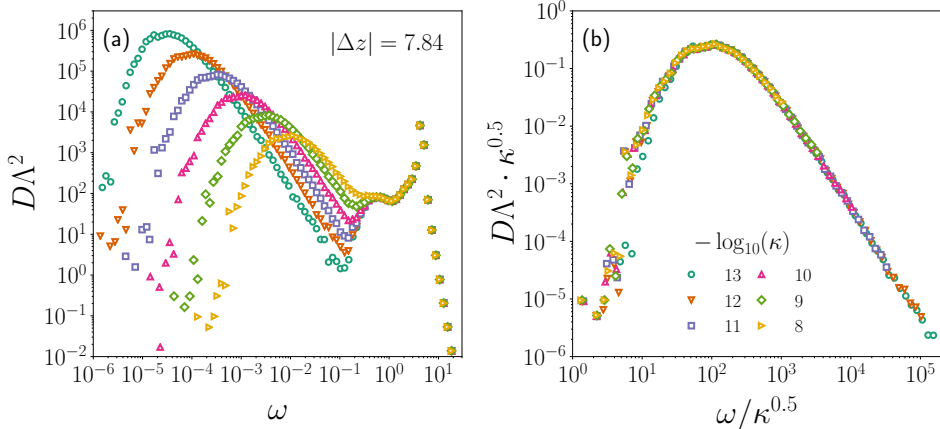
In the following we focus on the non-affine regime. We present the density of states and Λ^2 and explain why the shear modulus scales as $G \sim \kappa$. We will also motivate the crossover exponent λ. To our knowledge this is the first time that the density of states for the Mikado network has been reported. The graphs are generated from an ensemble of 1000 networks per condition.

Figure 4.10a shows the density of states for one value of $|\Delta z|$ and varying bending stiffness. Again, as we already saw in the previous two examples concerned with RC networks, there is a pronounced peak in the density of states, which shifts to higher frequencies as the bending stiffness is increased. The high frequency regime is not significantly influenced by a change in κ.

If the system is considered in the bending-dominated regime, the potential energy w stored in one line segment of length ℓ can be approximated by

$$w(\ell) \sim \kappa \frac{(\delta\theta)^2}{\ell} \sim \kappa \frac{(\Delta u_\perp)^2}{\ell^3} \sim \kappa \frac{\ell_f^2}{\ell^3} . \tag{4.22}$$

Here we assumed that typical non-affine deformations are not correlated and on the order of the filament length ℓ_f [87, 89]. In [89] the authors argue

Figure 4.10: (a) The density of states for one value of $|\Delta z|$. Again we find a dominant peak which shifts to higher frequencies if κ increases. (b) Collapse of the graphs in (a) with the bending stiffness.

that, since a segment's stiffness increases strongly with decreasing length ℓ, there is a single length scale $\ell_{\min}$ with which the response of the system can be approximated. The idea is that segments with a length $\ell < \ell_{\min}$ deform their surroundings rather than being deformed themselves. If the segment length $\ell > \ell_{\min}$, it is soft such that it is deformed itself and does not deform the surrounding area. Consequently, the short segments of length $\ell_{\min}$ increase the energy of the surrounding rods by $w(\ell_{\min})$ (and are not deformed themselves). The authors in [89] argue that this energy contribution is dominant so that it is possible to equate the average energy in a fiber W with the energy stored in a short segment:

$$W = \frac{\ell_f}{|\Delta z|} \int_{\ell_{\min}}^{\infty} w(\ell)P(\ell)\mathrm{d}\ell = w(\ell_{\min}).$$

(4.23)

The probability distribution of the length of the segments is exponential $P(\ell) = 1/\ell_s \exp(-\ell/\ell_s)$. Equation (4.23) can be solved, which yields $\ell_{\min} = \ell_f|\Delta z|^2$. Finally, one finds an average energy per rod of:

$$W \sim \omega_p^2 \sim \frac{\kappa}{\ell_f}\left(\frac{1}{|\Delta z|}\right)^6.$$

(4.24)

The energy is linear in κ and one finds a high scaling exponent in $|\Delta z|$. The linear behavior in κ implies (similar to the two cases earlier this chapter) that there are typical frequencies that scale with $\kappa^{0.5}$. In Figure 4.10 we plot a collapse of the peak in the density of states, which matches the mean field prediction.

Different behavior in the shear modulus, compared to the two previous examples, arises in the dependence on the distance from the isostatic point.
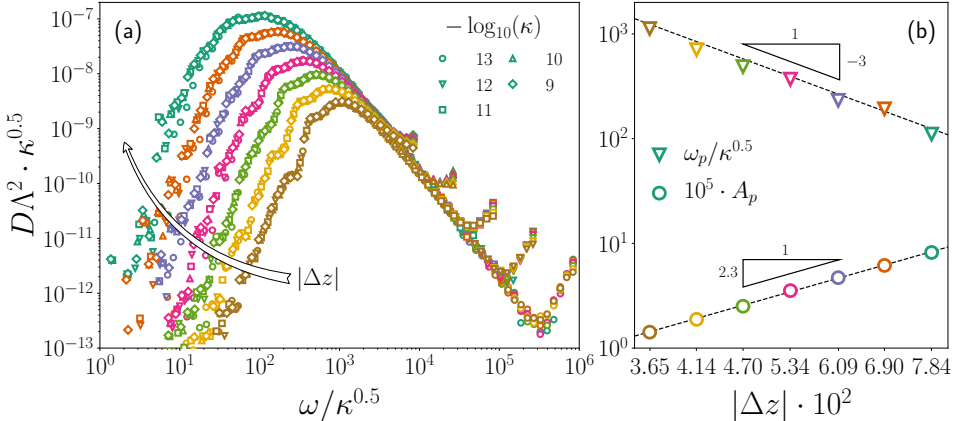
Figure 4.11: (a) Density of states collapsed as shown in 4.10b for varying $|\Delta z|$ (see the x-axis in (b)). The peak in the density of states shifts to lower frequencies as one moves away from the isostatic point. (b) Area below the peak and its position.

In RC networks $|\Delta z|$ only controls the number of soft modes and therefore the height of the peak in the density of states. However, in the Mikado model the rods become stiffer towards bending when ℓ_s is decreased. Consequently, as $|\Delta z|$ is decreased, the area below the peak decreases and in addition the peak shifts to higher frequencies. From equation (4.24) we expect to find a typical peak frequency in the density of states that scales with the distance to isostaticity as $\omega_p \sim |\Delta z|^{-3}$. The area below the peak A_p is expected to decrease with the distance to jamming as $A_p \sim \Delta z$, as determined in Section 4.4.1.

Figure 4.11a shows the density of states for varying κ and $|\Delta z|$. The graphs are collapsed using the bending stiffness. The peak of graphs with smaller $|\Delta z|$ clearly moves to higher frequencies. To probe the scaling of the peak position we determine the peak value of the density of states, rescale it with the bending stiffness, and average over all bending stiffnesses from $\kappa = 10^{-13}$ to $\kappa = 10^{-9}$. The result for $\langle \omega_p/\kappa^{0.5} \rangle_\kappa$ in Figure 4.11b confirms the prediction in 4.24.

The area below the peak is probed by integrating over the peak. However, for low Δz and high κ the peak is not clearly defined, because it merges with the high frequency plateau. For that reason we only use the two lowest values of the bending stiffness, $\kappa = 10^{-13}$ and $\kappa = 10^{-12}$. For these two values the peak is always well separated from the high frequency plateau for all $|\Delta z|$. We integrate from the lowest frequency available to the local minimum that separates the peak from the plateau. The results for the two values of κ are averaged and reported in 4.11b. We find that the area scales as $A_p \sim |\Delta z|^{2.3}$, which differs significantly from our prediction $A_p \sim |\Delta z|$. To understand the origin of this discrepancy, we now investigate the coupling Λ^2 separately.
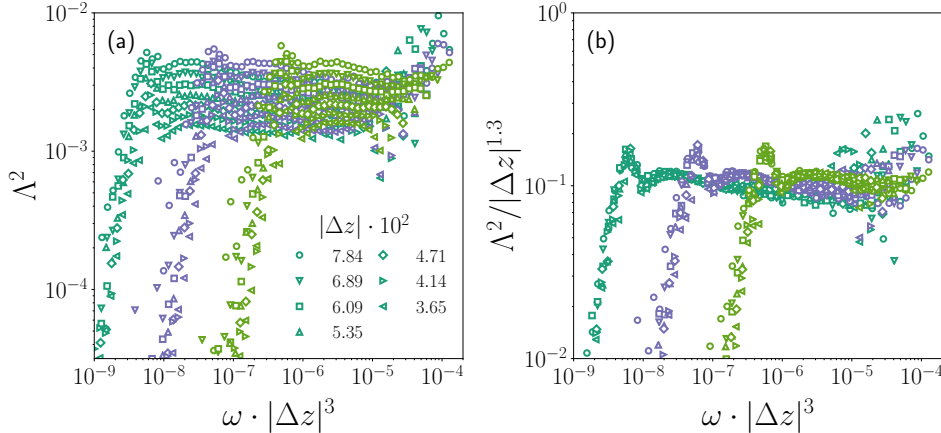
Figure 4.12: (a) Λ^2 for three bending stiffnesses: $\kappa = 10^{-13}$, 10^{-11} and 10^{-9}. The data is plotted for the same ω-range as in 4.11a. (b) The shift in the plateau value can be collapsed with $|\Delta z|$.

The assumption that $A_p \sim |\Delta z|$ is based on the assumption that the coupling Λ^2 is a constant which does not depend on $|\Delta z|$. Figure 4.12a shows Λ^2 for three values of κ and varying $|\Delta z|$. We plot the data for the same range of ω as in Figure 4.11a and shift it with the peak position. The data confirms that Λ^2 does not depend strongly on ω in the regime where the density of states has a peak. However, the value of the plateau depends on $|\Delta z|$, contrary to our assumption. This is qualitatively different from the random spring networks discussed in the previous sections, where there is no such dependence. Figure 4.12b shows that the plateau value can be collapsed with $|\Delta z|^{-1.3}$. That shows that the origin of the discrepancy of the expected scaling of A_p and the one we measure (Figure 4.11b) is buried in the coupling Λ^2.

Finally, we can connect the density of states and Λ^2 to the shear modulus in the bending dominated regime:

$$\frac{1}{G} \sim \int_0^\infty \frac{D\Lambda^2}{\omega^2}\, \mathrm{d}\omega \approx \ell_f^2 \int_0^\infty \frac{|\Delta z||\Delta z|^{1.3}}{\omega^2}\delta(\omega - \omega_p)\, \mathrm{d}\omega\,. \tag{4.25}$$

With the scaling of ω_p introduced in equation 4.24 we get the scaling for the shear modulus

$$G \sim \frac{\kappa}{\ell_f^3}\frac{1}{|\Delta z|^{8.3}} \quad \Leftrightarrow \quad \frac{G}{G_{\mathrm{aff}}} \sim \frac{\kappa}{\mu\ell_f^2}\frac{1}{|\Delta z|^{7.3}}\,. \tag{4.26}$$

This scaling of G derived from the area below the peak and its position is close to the scaling we observe from directly measuring the shear modulus (see Figure 4.9) where we find that $G/G_{\mathrm{aff}} \sim 1/|\Delta z|^{7.2}$. The discrepancy between the two exponents is small considering its high value. Furthermore,

the integration over the peak in Figure 4.11 is erroneous for the smallest values of $|\Delta z|$. Here the peak does not seperate well from the high frequency regime.

The features of the density of states can be rationalized by mean field arguments, however, there are no such arguments for the behavior of Λ^2, yet. Our numerical measurments clearly show that the shear response is dominated by soft modes that would be floppy if the bending stiffness were $\kappa = 0$. As a result the shear modulus of Mikado networks increases linearly with the perturbation strength κ - the same behavior that we found in RC networks with tension and bending interactions. Different than in RC spring networks, the bending stiffness is a function of the spring length. As a result, trial modes which consist of floppy modes are not enough to capture the response. The integral in equation (4.23) has to be regularized by a minimum segment length below which no floppy response can occur.

4.5. *Conclusions*

We have shown three examples in which hypostatic randomly cut networks are rigidified by a perturbing field. We showed networks and perturbing fields that are qualitatively different. However, the shear response could be described by basic mean field assumptions that were shared by all three systems.

The most important common feature is that the shear response for small perturbations is linear in the perturbation strength and dominated by floppy-like soft modes. The number of these soft modes is proportional to the fraction of floppy modes in the unperturbed system.

We are able to use the mean behavior of these modes to predict the density of states. In all three examples we find that the density of states feature a dominant peak which has a characteristic peak frequency that shifts with the square root of the amplitude of the perturbation. The area below the peak is proportional to $|\Delta z|$. The Mikado model forms an exception - the coupling of the eigenmodes to the shear degree of freedom depends on the distance to isostaticity. In case of RC networks this is not the case which makes it possible to restrict all considerations to the density of states. To get a better understanding of the response of Mikado networks it is therefore necessary to gain better insight into the scaling of Λ^2.

The considerations in this chapter are not limited to the three systems discussed. Other systems like networks with a mixture of hard and soft springs [21] or packings of hard and soft particles are expected to show similar behavior.

5

Normal stresses, contraction, and stiffening in sheared elastic networks

When elastic solids are sheared, a nonlinear effect named after Poynting gives rise to normal stresses or changes in volume. We provide a novel relation between the Poynting effect and the microscopic Grüneisen parameter, which quantifies how stretching shifts vibrational modes. By applying this relation to random spring networks, a minimal model for, e.g., biopolymer gels and solid foams, we find that networks contract or develop tension because they vibrate faster when stretched. The amplitude of the Poynting effect is sensitive to the network's linear elastic moduli, which can be tuned via its preparation protocol and connectivity. Finally, we show that the Poynting effect can be used to predict the finite strain scale where the material stiffens under shear.
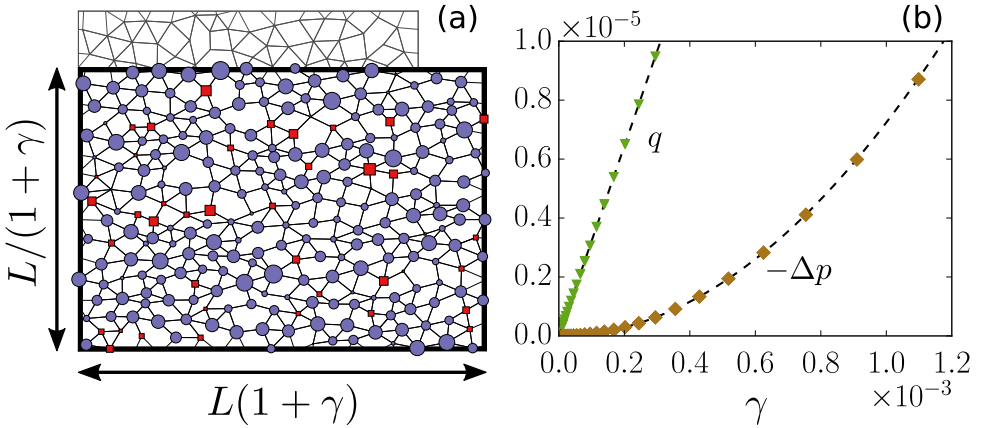
Figure 5.1: (a) Pure shear strain γ applied to an unstressed spring network. Each node's area is proportional to its contribution to the pressure p; circles (squares) are tensile (compressive). (b) The initial growth of the shear stress q is linear in γ, while p is quadratic and negative (tensile).

5

5.1. *Introduction*

The Poynting effect refers to the tendency of a sheared elastic solid to expand or contract in the direction normal to a shearing surface, or to develop normal stress if the surface is held fixed [90, 91]. A similar phenomenon known as Reynolds dilatancy occurs during plastic (versus elastic) deformation of granular media [92, 93]. The "positive" Poynting effect was first observed in metal wires, which lengthen or push outwards at their ends when twisted [91]. More recently, the negative Poynting effect (contraction or tension) was seen in semiflexible polymers from the cytoskeleton and extracellular matrix [94].

Models of the Poynting effect contain phenomenological elements or strong approximations [94–100]. Suggested causes in fiber networks include asymmetry (hence nonlinearity) in the fibers' force extension curve [94, 96], fiber alignment in the initial condition [100], and non-affinity in networks stabilized by bending [89, 101]. While these ingredients may be sufficient to induce the Poynting effect, we find that they are not necessary. This point is made by Figure 6.1a, which depicts an isotropic spring network in 2D subjected to pure shear at constant volumetric strain $\epsilon = 0$. The springs are purely harmonic and initially isotropic, and there are no bending interactions. Nodes that develop tension, labeled with a circle, greatly outnumber nodes under compression (squares), suggesting a negative Poynting effect. And indeed a plot of the pressure change Δp is negative (Figure 6.1b). While the shear stress q grows linearly with the shear strain γ, Δp grows quadratically due to isotropy, which requires pressure or volume changes to be even in γ.

In this Letter we introduce a new micromechanical approach to the Poynting effect, applicable for any elastic interaction between network elements. We focus on the initial growth of Δp and ϵ through the coefficients

$$\chi_\epsilon = \left[\left(\frac{\partial^2 p}{\partial\gamma^2}\right)_\epsilon\right]_0 \quad \text{and} \quad \chi_p = \left[\left(\frac{\partial^2 \epsilon}{\partial\gamma^2}\right)_p\right]_0. \tag{5.1}$$

χ_ϵ and χ_p are evaluated in the initial condition ("0"). Their subscript distinguishes strain control (fixed $\epsilon = 0$) from stress control (fixed $\Delta p = p - p_0 = 0$). We derive exact expressions for the coefficients in hyperelastic solids (e.g. rubbers, solid foams, and tissue), which have reversible stress-strain relations. Note that particulate media are generally not hyperelastic due to shear-induced rearrangements. We relate χ_ϵ and χ_p to a network's vibrational modes and the microscopic Grüneisen parameter Γ_n [102], which quantifies how volumetric strain shifts the frequency ω_n of the nth mode,

$$\Gamma_n = -\left[\left(\frac{1}{\omega_n}\frac{\partial\omega_n}{\partial\epsilon}\right)_\gamma\right]_0. \tag{5.2}$$

We validate our predictions numerically in random networks of linear springs (Figure 1), which are widely studied as minimal models of, e.g., polymer networks, foams, and glasses [12, 21, 22, 71, 103–107]. We show that the sign of the Poynting effect in spring networks is negative and set by the Grüneisen parameter, which can be motivated theoretically. We focus on marginally rigid spring networks close to the isostatic state (mean coordination $z = z_c + \Delta z$, with $z_c \approx 4$ in 2D), and study scaling with Δz.

5.2. *Spring networks*

For concreteness, we first illustrate the Poynting effect in random spring networks.

We consider networks of $N = 1024$ harmonic springs in a periodic unit cell with initial side lengths $L_1 = L_2 = L$. Networks are prepared in two ways. Packing derived (PD) networks are prepared by generating bidisperse packings of soft repulsive disks close to the jamming transition [8, 63, 108]. Each contact between disks is then replaced by a spring with stiffness k and a rest length ℓ_{ij}^0 equal to its initial length ℓ_{ij}, so $p_0 = 0$ [20, 102, 107, 109, 110]. To prepare randomly cut (RC) networks, we start from a PD network with mean coordination $z \approx 6$ and randomly remove springs, with a bias towards highly connected nodes [21, 22, 71]. All numerical results are presented in dimensionless units by setting k and the average disk size in the initial packing to unity. PD and RC networks are indistinguishable by eye, but their shear modulus $G \sim \Delta z^\mu$ and bulk modulus $K \sim \Delta z^{\mu'}$ have qualitatively different dependence on excess connectivity Δz (Figure 5.2, open symbols). In PD networks, G vanishes continuously with $\mu_{\text{PD}} = 1$,
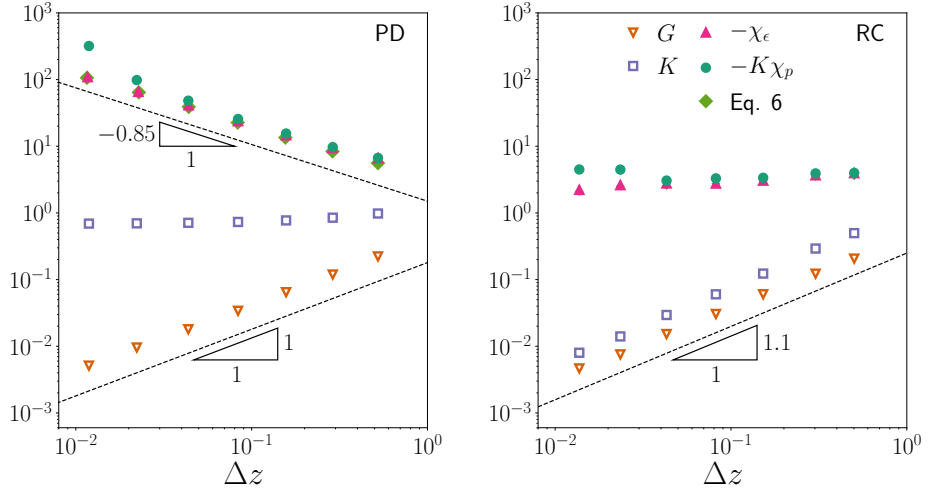
Figure 5.2: The shear modulus G, bulk modulus K, and Poynting coefficients χ_ϵ and χ_p as a function of excess coordination Δz for (a) packing derived and (b) randomly cut spring networks.

while K jumps discontinuously to zero ($\mu'_{\mathrm{PD}} = 0$) [3]. In contrast, in RC networks both G and K vanish continuously, with $\mu_{\mathrm{RC}} = \mu'_{\mathrm{RC}} \approx 1.1$ [21, 22, 71]. We will exploit these differences to test our predictions for the Poynting coefficients.

We consider deformations combining pure shear strain and volumetric expansion, such that lattice vectors of the unit cell are transformed by the deformation gradient

$$\hat{\mathcal{F}} = (1 + \epsilon) \left[\begin{array}{cc} 1 + \gamma & 0 \\ 0 & (1+\gamma)^{-1} \end{array} \right]. \tag{5.3}$$

The corresponding Cauchy stress tensor is

$$\hat{\sigma} = \left[\begin{array}{cc} -p - q & 0 \\ 0 & -p + q \end{array} \right]. \tag{5.4}$$

When networks are sheared using strain control, ϵ is held fixed at zero while γ is increased incrementally. At each step the elastic energy $\sum_{ij} V_{ij} = (k/2) \sum_{ij} (\ell_{ij} - \ell_{ij}^0)^2$ is minimized with respect to the node positions using FIRE [26]. The resulting p and q are determined from

$$\sigma_{\alpha\beta} = 1/(L_1 L_2) \sum_{ij} f_{ij} \, \ell_{ij} (\hat{\boldsymbol{n}}_{ij,\alpha} \hat{\boldsymbol{n}}_{ij,\beta}), \tag{5.5}$$

where $f_{ij} = -\partial V_{ij}/\partial \ell_{ij}$ and $\hat{\boldsymbol{n}}_{ij}$ is a unit vector pointing from node i to j. For stress controlled simulations, γ and ϵ are also allowed to vary while

the energy is minimized subject to $p = 0$ and a prescribed q [16]. Because finite-sized systems are never perfectly isotropic, plots of p or ϵ versus γ contain a linear contribution with a prefactor that vanishes as $N \to \infty$ [69]. To estimate the Poynting coefficients, we symmetrize p and ϵ by averaging the response to shearing both "forward" ($\gamma > 0$) and "backward" ($\gamma < 0$).

Figure 5.2 presents our first main result, the Poynting coefficients for PD and RC networks over a range of Δz. In all cases the Poynting effect is negative. There is an apparent equality between χ_ϵ and $K\chi_p$ (motivated below), albeit with fluctuations at the lowest z. There is a notable difference in how the PD and RC Poynting coefficients scale with with Δz. In PD networks χ_ϵ and $K\chi_p$ diverge, with an empirical fit to $1/\Delta z^{\lambda_{\mathrm{PD}}}$ giving $\lambda_{\mathrm{PD}} \approx 0.85$. In contrast, in RC networks χ_ϵ and $K\chi_p$ are flat ($\lambda_{\mathrm{RC}} = 0$). Hence the Poynting coefficients depend on both preparation and shearing protocols, and in three out of four cases they diverge at the isostatic point.

5.3. *Microscopic theory*

We now develop exact expressions for the Poynting coefficients, beginning with the relation between χ_ϵ and χ_p. In a hyperelastic material, the pressure $\Delta p = (1/2)\chi_\epsilon \gamma^2$ due to shearing at fixed ϵ must be equal to the pressure from a two-step process: first shearing to γ at constant p, followed by a volumetric strain $\epsilon = -(1/2)\chi_p \gamma^2$ that reverses the volume change induced in the first leg. The second step changes pressure by $\Delta p = -K\epsilon = (1/2)K\chi_p\gamma^2$, and therefore $\chi_\epsilon = K\chi_p$.

We next relate χ_ϵ to the shear modulus $G(\epsilon) = (1/2)[(\partial q/\partial \gamma)_\epsilon]_{\gamma=0}$ after a volumetric strain. The total differential of the strain energy density is $dW = \hat{\mathcal{S}} : d\hat{\mathcal{E}}$, where $\hat{\mathcal{E}} = (\hat{\mathcal{F}}^T\hat{\mathcal{F}} - \mathbb{1})/2$ is the Green-Lagrange strain. The second Piola-Kirchoff stress $\hat{\mathcal{S}}$ is related to the more experimentally-relevant Cauchy stress via $\hat{\sigma} = \hat{\mathcal{F}}\hat{\mathcal{S}}\hat{\mathcal{F}}^T/J$, where $J = \det\hat{\mathcal{F}}$. Hence

$$dW = 2(1+\epsilon)^2 \left[-\frac{p\,d\epsilon}{1+\epsilon} + \frac{q\,d\gamma}{1+\gamma} \right] . \qquad (5.6)$$

Using the Maxwell relation of Eq. (5.6), one finds

$$\chi_\epsilon = -2G'(0) - 4G(0), \qquad (5.7)$$

where the prime indicates differentiation with respect to ϵ. Earlier work neglected the difference between the various stress and strain measures in nonlinear elasticity, but still arrived at the same result [95, 97]. Numerical evaluation of Eq. (5.7) is in good agreement with direct measurements of χ_ϵ and $K\chi_p$, as shown in Figure 5.2.

We now relate χ_ϵ to discrete degrees of freedom. Network elasticity is encoded in the the extended Hessian $\hat{\mathcal{H}} = \partial^2 U/\partial |\boldsymbol{q}\rangle^2$, where the the $2N+1$-component vector $|\boldsymbol{q}\rangle$ contains the node positions and shear strain γ [13]. The shear modulus can be written as a sum over the non-rigid body eigenmodes of $\hat{\mathcal{H}}$, $1/G = (v/N)\sum_n \Lambda_n^2/\omega_n^2$, where $v = JL^2/N$, ω_n^2 is the squared
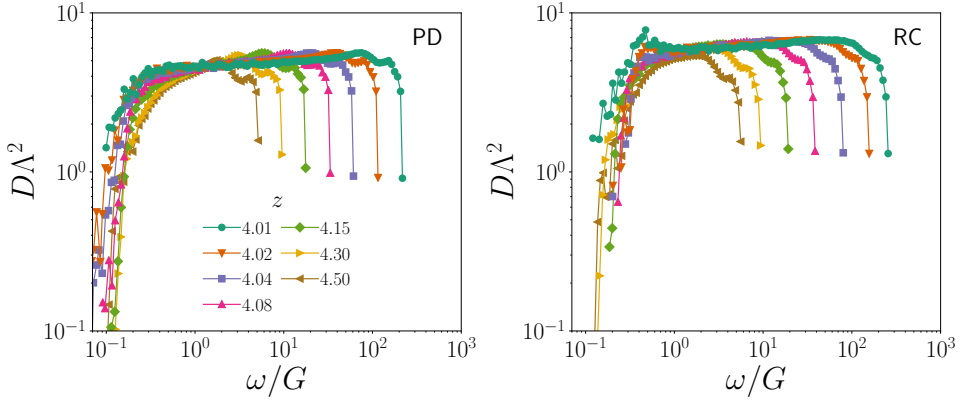
Figure 5.3: The product $D\Lambda^2$ versus eigenfrequency ω in PD and RC networks at varying coordination z. D is the density of states and Λ^2 is a measure of modes' coupling to shear.

5

eigenfrequency of the nth eigenvector, and Λ_n/N is its component along the strain coordinate [13]. Letting $D(\omega)$, $\Lambda^2(\omega)$ and $\Gamma(\omega)$ denote the density of states and averages of Λ_n^2 and the Grüneisen parameter Γ_n in the interval $[\omega, \omega + \mathrm{d}\omega)$, and replacing sums with integrals, we find

$$\frac{1}{G} = v \int_0^\infty \frac{D\Lambda^2}{\omega^2}\, \mathrm{d}\omega\,, \tag{5.8}$$

and, from Eq. (5.7),

$$\chi_\epsilon = 2vG^2 \int_0^\infty \frac{\Gamma}{\omega^2} \left[2 - \frac{\partial \ln \Lambda^2 D}{\partial \ln \omega}\right] \Lambda^2 D\, \mathrm{d}\omega\,. \tag{5.9}$$

Eq. (5.9) is a central result: it explicitly relates the Poynting effect to vibrational modes. Note that the sign of χ_ϵ is controlled by Γ and the logarithmic derivative of $\Lambda^2 D$.

5.4. *Application to networks*

We now evaluate Eq. (5.9) in the context of spring networks, focusing on the scaling of χ_ϵ with Δz. Close to the isostatic state, both PD and RC networks display an anomalous abundance of "soft modes" that dominate the response to forcing [9, 13, 21, 80]. The modes appear above a characteristic frequency ω^*, and for scaling analysis the density of states is well approximated by a window function between ω^* and $\omega_0 \sim \mathcal{O}(k^{1/2})$ [9, 19, 80]. Following Ref. [13], we assume that all soft modes couple similarly to shear, so $\Lambda^2 \sim$ const. Hence Eqs. (5.8) and (5.9) give $\omega^* \sim G$ and

$$\chi_\epsilon \sim G^2 \int_{\omega^*}^{\omega_0} \frac{\Gamma}{\omega^2} \mathrm{d}\omega\,. \tag{5.10}$$
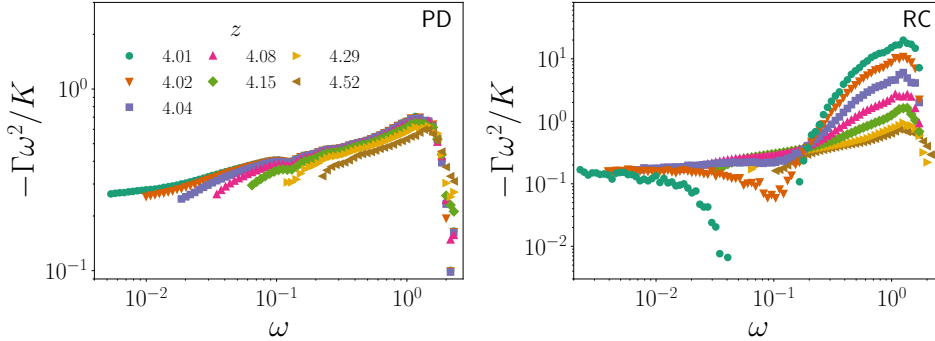
Figure 5.4: The Grüneisen parameter Γ for PD and RD networks, scaled by the prediction of Eq. (5.11) and plotted for $\omega > \omega^*$. Symbols match the legends in Figure 5.3

The sign and form of Γ can be rationalized with scaling arguments. Perturbing a network along mode n carries an energetic cost $\Delta U \propto \omega_n^2$, so $\Gamma \sim -\omega^{-2}(\partial \Delta U/\partial\epsilon)$. ΔU can be expanded in $u_{ij}^{\parallel}$ and $u_{ij}^{\perp}$, the relative normal and transverse motions, respectively, between connected nodes. The well-known result is $\Delta U = (1/2)\sum_{ij}[k(u_{ij}^{\parallel})^2 - (f_{ij}/\ell_{ij})(u_{ij}^{\perp})^2]$, where the force f_{ij} and length ℓ_{ij} are evaluated prior to the perturbation [111]. In a network that has previously undergone a small volumetric strain ϵ from its unstressed state, the typical force will be proportional to the pressure $p = -K\epsilon$, and so $\partial \Delta U/\partial\epsilon \sim K(u^{\perp})^2 N$. Soft modes strongly resemble floppy motions (which neither stretch nor compress springs), with typical transverse motions $u^{\perp} \sim 1/N^{1/2}$, independent of ω [20, 80]. Therefore

$$\Gamma \sim -K/\omega^2 \,, \tag{5.11}$$

and, by Eq. (5.10),

$$\chi_\epsilon \sim -K/G \,. \tag{5.12}$$

This remarkably simple expression for χ_ϵ correctly predicts the sign of the Poynting effect and captures all of the phenomenology in Figure 5.2. It relates the qualitatively different behavior of χ_ϵ in PD and RC networks to the differences in their shear and bulk moduli, predicting $\lambda_{\mathrm{RC}} = 0$ and $\lambda_{\mathrm{PD}} = \mu_{\mathrm{PD}} = 1$. On a qualitative level, it explains that the Poynting effect in spring networks is negative because tension is stabilizing. Finally, the strength of the Poynting effect grows near isostaticity because tension couples to transverse motions, which dominate soft modes and cause strong non-affine fluctuations [21, 80, 110].

The above scaling arguments rely on two essential approximations, namely that $D\Lambda^2 \sim$ const and $\Gamma \sim -K/\omega^2$ above $\omega^* \sim G$. We now validate them by direct numerical evaluation. In Figure 5.3, $D\Lambda^2$ is plotted as a function of ω/G for both PD and RC networks. As expected, in both cases there is a broad plateau above ω^*. In Figure 5.4 we plot the ratio of
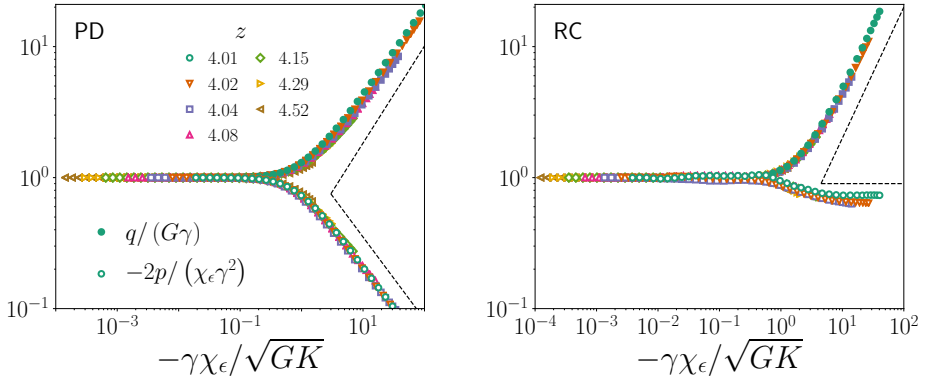
Figure 5.5: Master curves for shear stress q and pressure p of PD and RC networks sheared to finite strain γ at fixed $\epsilon = 0$. The dashed lines on the left have slopes 0.74 and -0.63. On the right the slopes are one and zero.

Γ to $-K/\omega^2$; Γ is estimated from a linear fit of ω_n versus ϵ after a series of small volumetric strain steps. In PD networks the ratio approaches a positive constant as $\Delta z \to 0$, indicating that Eq. (5.11) becomes increasingly accurate as the isostatic point is approached. At finite Δz there is a slow upturn with increasing ω. We attribute this to a subdominant correction to scaling, consistent with the observation that a power law fit to χ_ϵ and $K\chi_p$ in PD networks gives a somewhat smaller value of λ_{PD} than 1. The same ratio has a more complex form in RC networks, including a sign change for the lowest z, but it also approaches a low frequency plateau in the isostatic limit.

5.5. *Finite strain*

The Poynting coefficients quantify the leading order dependence of Δp and ϵ on γ. We now show that the Poynting coefficient χ_ϵ predicts the onset of strain stiffening when a network is sheared at fixed volume.

There has been no prior study of PD networks at finite strain, while studies of RC networks did not report normal stresses. RC shear stresses were shown to stiffen beyond some vanishing strain scale γ^* [21] (unlike sphere packings, which soften [28, 112]). The secant modulus q/γ in RC networks satisfies $q/(G\gamma) = \mathcal{Q}(\gamma/\gamma^*)$, with $\mathcal{Q} \sim 1$ for $x \ll 1$ and $\mathcal{Q} \sim |x|^\theta$ with $\theta > 0$ for $x \gg 1$ [21]. It is natural to make a similar ansatz for the pressure,

$$\frac{2p}{\chi_\epsilon\gamma^2} = \mathcal{P}(\gamma/\gamma^*)\,, \tag{5.13}$$

where $\mathcal{P} \sim 1$ for $x \ll 1$ and $\mathcal{P} \sim |x|^\phi$ for $x \gg 1$.

The scaling functions $\mathcal{Q}$ and $\mathcal{P}$ are plotted in Figure 5.5. In Ref. [21] it was argued that $\gamma^* \sim \Delta z$, which agrees with our RC network data but

fails for PD networks. Instead, we find that data from both network types collapses with

$$\gamma^* \sim \frac{\sqrt{GK}}{|\chi_\epsilon|} \sim \Delta z^\nu \, , \tag{5.14}$$

with $\nu = \lambda + (\mu + \mu')/2$. In order for shear stress and pressure to remain finite when $\Delta z \to 0$, we must have $\theta = \mu/\nu$ and $\phi = -\lambda/\nu$. These give $\theta_{\mathrm{PD}} \approx 0.74$ and $\phi_{\mathrm{PD}} \approx -0.63$ (using $\lambda_{\mathrm{PD}} = 0.85$), as well as $\theta_{\mathrm{RC}} \approx 1$ and $\phi_{\mathrm{RC}} \approx 0$. These are all in good agreement with numerics (dashed lines in Figure 5.5).

To motivate γ^*, we expand the secant modulus in $p(\gamma)$ to find

$$\frac{q}{2G\gamma} \sim 1 + \frac{\chi_\epsilon^2 \gamma^2}{GK} + \mathcal{O}\left(\gamma^4\right) \, . \tag{5.15}$$

Here we have neglected numerical prefactors and used Eq. (5.7), assuming $G'(0) \gg G(0)$ (appropriate near isostaticity). Balancing terms on the right-hand side yields Eq. (5.14), an extrapolated strain scale where the initial linear form of the stress-strain curve breaks down. A link between normal stresses and stiffening was also evidenced in [113].

5.6. *Conclusions*

We have derived exact expressions for the Poynting coefficients in hyperelastic materials, and validated them numerically in two classes of spring networks. Both display a negative Poynting effect, whose origin can be traced to the stabilizing influence of tension on a network's vibrational modes. The amplitude of the effect is controlled by the coupling between tension and relative transverse motions, which explains the correlation between normal stress and non-affinity [101], and results macroscopically in a coefficient χ_ϵ that scales with the ratio K/G. Eq. (5.9) is applicable in any 2D hyperelastic material – hence our results can lend insight to the Poynting effect in other elastic networks, including fiber networks (e.g. [23, 24, 82, 89, 101, 114]). The scaling arguments for $D\Lambda^2$ and Γ presented here are specific to spring networks; they must be modeled or evaluated anew for each material. Our calculations and numerics are all in 2D, but extension to 3D is straightforward and we do not expect the underlying physics to change.

We have shown that Poynting coefficients and stiffening behavior are highly sensitive to the linear elastic moduli. Recent work has demonstrated how to prepare spring networks using a biased cutting protocol to target essentially any positive value of K/G [115, 116]. Our results indicate that the same techniques could be used to select for desirable nonlinear mechanical properties.

One can ask whether the elastic Poynting effect gives insight into Reynolds dilatancy. As noted above, our approach does not apply to irreversible deformations. More heuristically, we note that whereas volumetric

expansion stabilizes elastic systems, it destabilizes particulate matter by opening contacts. This suggests a sign difference, and indeed materials like sand generally dilate under shear unless prepared in a loose state.

5

6

Viscous forces and bulk viscoelasticity near jamming

When weakly jammed packings of soft, viscous, non-Brownian spheres are probed mechanically, they respond with a complex admixture of elastic and viscous effects. While many of these effects are understood for specific, approximate models of the particles' interactions, there are a number of proposed force laws in the literature, especially for viscous interactions. We numerically measure the complex shear modulus G^* of jammed packings for various viscous force laws that damp relative velocities between pairs of contacting particles or between a particle and the continuous fluid phase. We find a surprising sensitive dependence of G^* on the viscous force law: the system may or may not display dynamic critical scaling, and the exponents describing how G^* scales with frequency can change. We show that this sensitivity is closely linked to manner in which viscous damping couples to floppy-like, non-affine motion, which is prominent near jamming.

6.1. *Introduction*

Dense packings of soft, viscous, non-Brownian spheres are widely stud-ied as a minimal model for emulsions, aqueous foams, and soft suspen-sions [7, 28, 75, 76, 117–120]. When compressed, soft spheres "jam" into a marginally solid state with a shear modulus that grows continuously above a critical packing fraction $\phi_c \approx 0.84$ in 2D and 0.64 in 3D [3]. Close to the jamming point, structural and mechanical properties display features reminiscent of a critical point, including diverging time and length scales [3, 7, 9, 11–13, 39, 75, 76, 109, 121, 122]. Mechanically probing the sys-tem on finite time scales reveals a mixture of elastic and viscous response [7, 13, 28, 119, 120, 122]. However numerical studies typically represent particles' viscous interactions with their neighbors and/or the continuous fluid phase using approximate, computationally inexpensive force laws. Here we use simulations and theory to demonstrate that viscoelastic prop-erties of jammed solids are surprisingly sensitive to the form of the viscous force law. Linear viscoelasticity is characterized by the frequency depen-dent complex shear modulus $G^*(\omega) = G'(\omega) + \imath\, G''(\omega)$; its real and imaginary parts are known as the storage and loss modulus, respectively, and quan-tify the amount of energy stored elastically and dissipated viscously during one cycle of oscillatory driving at angular frequency ω [123]. The form of the complex shear modulus near jamming was first described by Tighe [13] for a system of soft spheres interacting via "one-sided" (purely repulsive) springs and linear viscous contact forces; details of the model are presented below. Characteristic features can be seen in Figure 6.1, which plots the average G^* for states prepared close to jamming. At both low and high frequencies, the storage modulus (filled symbols) and loss modulus (open symbols) re-semble a simple Kelvin-Voigt solid (a spring and dashpot in parallel) [123], with $G' \sim$ const and $G'' \sim \omega$. There is also a critical regime at intermediate frequencies, in which both G' and G'' scale as $\omega^{1/2}$. Similar square root scaling has been observed experimentally in foams, emulsions, and other complex fluids,[4, 124–127] and has been linked theoretically to strongly non-affine motion [4]. Plots of the particles' displacements from a static ini-tial condition, evaluated at zero and peak shear stress (Figure 6.1, bottom six panels) show that the critical regime represents a broad crossover from highly non-affine motion in the quasistatic limit at vanishing ω, to strongly affine motion at high frequencies.

The square root scaling is anomalous, in the sense that simple linear in-teractions at the particle scale give rise to nonlinear frequency dependence in the bulk. In contrast, the frequency dependence of G^* in a Kelvin-Voigt solid is consistent with a direct extrapolation from the elastic forces (linear in the particle displacements) and viscous forces (linear in the velocities). Moreover, in soft spheres the critical regime broadens on approach to the jamming transition, with its lower bound approaching zero as the confining pressure p goes to zero and the system unjams [13]. This strongly suggests
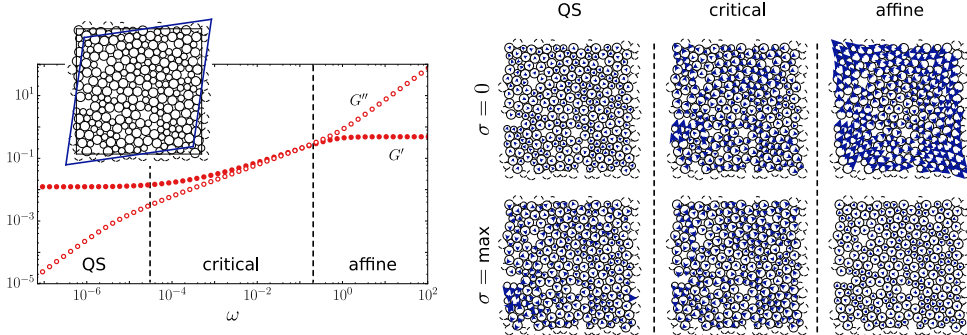
Figure 6.1: (left) Storage modulus G' and loss modulus G'' of a packing of viscous soft disks (inset) prepared at pressure $p = 10^{-4}$ and sheared at driving frequency ω. (right) Particle displacements evaluated at zero and peak stress amplitude for $\omega = 10^{-10}$, 10^{-3}, and 10^4.

that critical effects lie at the origin of the square root scaling near jamming.

While spring-like forces are standard in numerical models of foams and emulsions [3, 7, 13, 28, 75, 76, 118, 119, 128], a number of alternate proposals for viscous interactions can be found in the literature [7, 129–132]. This variety is largely due to authors' efforts to strike a balance between physical accuracy and computational complexity. What influence does the viscous force law have on bulk viscoelastic response near jamming? In equilibrium systems near a critical point, growing correlations wash out particle-scale details, so that similar scaling in bulk properties can be found for different interparticle interactions [133]. Here we show that the nonequilibrium jamming transition is different: the complex shear modulus near jamming is surprisingly sensitive to the form of the viscous force law. Seemingly similar choices can alter the apparent scaling exponents or eliminate dynamic critical scaling entirely. Still others lead to subtler changes in the form of correlation functions.

To probe the role of viscous damping in viscoelasticity near jamming, we implement computer simulations of Durian's bubble model, a widely studied numerical model for foams and emulsions near ϕ_c. We investigate linear contact damping for varying ratios of the drag coefficients for normal and transverse motion, Stokes-like drag laws, and finally nonlinear damping of the relative velocities. One of our main conclusions will be to relate floppy-like, non-affine motion in the quasistatic limit to the form of the storage and loss moduli at finite frequency. We further study the role of two-point velocity correlations and effect of pre-stress on the dynamic viscosity.

6.2. *The bubble model*

Durian's bubble model treats individual bubbles as non-Brownian particles interacting via elastic and viscous forces [7]. The equations of motion are

overdamped, so that at all times the net elastic and viscous forces on a particle i balance,

$$\boldsymbol{F}_i^{\mathrm{el}} + \boldsymbol{F}_i^{\mathrm{visc}} = \boldsymbol{0}\,. \tag{6.1}$$

For contact forces $\boldsymbol{f}_{ij}$, the corresponding net force $\boldsymbol{F}_i = \sum_{j(i)} \boldsymbol{f}_{ij}$ can be found by summing over all particles j in contact with i.

We consider ensembles of packings of N particles in $D = 2$ spatial dimensions prepared at a target pressure p. $N = 32768$ unless indicated otherwise. Initial conditions are generated by minimizing the total elastic potential energy using a nonlinear conjugate gradient algorithm, starting from particle positions placed randomly via a Poisson point process. As is typical in studies of jamming [63], the packings are bidisperse to avoid crystallization, with equal numbers of large and small particles and a radius ratio 1.4:1. The systems are bi-periodic, and shear is imposed via Lees-Edwards boundary conditions.

Units are set by the mean particle size d, the particle stiffness k, and a microscopic time scale τ_1 (the latter two being introduced below). In simulations all three are set to one. However, in some cases we include the microscopic time scale in scaling relations in order to emphasize the dimensionful or dimensionless character of a relation.

All our simulations are performed in $D = 2$ spatial dimensions, which is the upper critical dimension for the jamming transition.[65] We therefore expect the critical behavior we describe here, and in particular the values of critical exponents, to remain unchanged for $D > 2$.

6.2.1. *Elastic interactions*

Elastic forces are modeled via "one-sided springs," i.e. a harmonic repulsion that acts only when particles overlap. Linear springs are a widely accepted[6, 8] approximate[134–139] description of the elastic repulsion that arises due to surface tension when spherical bubbles or droplets are deformed. The elastic force on particle i due to particle j is

$$\boldsymbol{f}_{ij}^{\mathrm{el}} = \begin{cases} -k\,\delta_{ij}\,\hat{\boldsymbol{n}}_{ij} & \text{for} \quad \delta_{ij} \geq 0 \\ \boldsymbol{0} & \text{for} \quad \delta_{ij} < 0\,. \end{cases} \tag{6.2}$$

Here we have introduced the contact stiffness k, the overlap $\delta_{ij} = \rho_i + \rho_j - \Delta r_{ij}$, and the normal vector $\hat{\boldsymbol{n}}_{ij} = (\boldsymbol{r}_j - \boldsymbol{r}_i)/\Delta r_{ij}$. The latter two quantities are defined in terms of the particle radii ρ_i and ρ_j, center positions $\boldsymbol{r}_i$ and $\boldsymbol{r}_j$, and center-to-center distance $\Delta r_{ij} = |\boldsymbol{r}_i - \boldsymbol{r}_j|$. The contact stiffness k is proportional to the surface tension and encodes the energetic cost of deforming a particle and thereby increasing its surface area.

For later convenience we note that the elastic energy corresponding to Eq. (6.2) is $U = \sum_{\langle ij \rangle} U_{ij}$, where

$$U_{ij} = \begin{cases} \frac{1}{2}k\delta_{ij}^2 & \delta_{ij} \geq 0 \\ 0 & \delta_{ij} < 0\,. \end{cases} \tag{6.3}$$
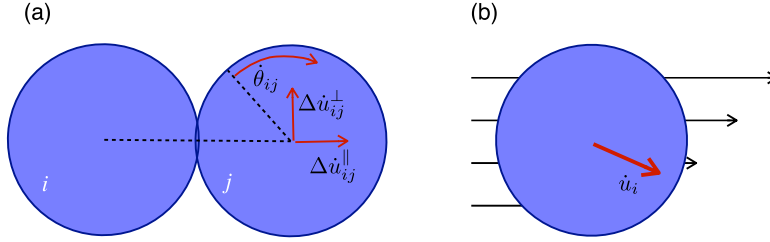
Figure 6.2: (a) Relative velocities in the rest frame of particle i. (b) Motion with respect to an affine flow field.

The energy change ΔU due to small perturbations away from an initial condition in mechanical equilibrium is

$$\Delta U \approx \sigma_0 \gamma V + \frac{1}{2} \sum_{\langle ij \rangle} \left[k \left(\Delta u_{ij}^{\parallel} \right)^2 - \frac{f_{ij}^0}{\Delta r_{ij}^0} \left(\Delta u_{ij}^{\perp} \right)^2 \right] , \qquad (6.4)$$

where $\Delta \boldsymbol{u}_{ij} = \boldsymbol{u}_j - \boldsymbol{u}_i$ is the relative displacement vector, $\Delta \boldsymbol{u}_{ij}^{\parallel} = (\Delta \boldsymbol{u}_{ij} \cdot \hat{\boldsymbol{n}}_{ij}) \hat{\boldsymbol{n}}_{ij}$ is its component along $\hat{\boldsymbol{n}}_{ij}$, $\Delta \boldsymbol{u}_{ij}^{\perp} = \Delta \boldsymbol{u}_{ij} - \Delta \boldsymbol{u}_{ij}^{\parallel}$ is the transverse component, γ the shear strain, and V the volume of the packing (area in 2D). The shear stress σ_0 in the reference state is small with a mean value equal to zero, because the preparation protocol is isotropic. f_{ij}^0 and Δr_{ij}^0 are the contact force and center-to-center distance in the reference packing, respectively. The term proportional to f_{ij}^0 captures the influence of stress in the reference packing, i.e. the confining pressure p. It is referred to as pre-stress, to distinguish it from stresses induced by the shear deformation. At several points below we present data calculated "without pre-stress," which is achieved by setting f_{ij}^0 to zero in Eq. (6.4). This is equivalent to replacing the packing with a network of springs, each with a rest length equal to Δr_{ij}^0 from the corresponding contact.

6.2.2. *Viscous interactions*

Here we describe the several viscous force laws considered below. These can be divided in three classes: linear contact forces, linear body forces, and nonlinear contact forces.

Linear contact damping: We will explore a class of linear viscous contact force laws that damp relative velocities at the point of contact,

$$\boldsymbol{f}_{ij}^{\text{visc}} = -k\tau_1 \left[\Delta \dot{\boldsymbol{u}}_{ij}^{\parallel} + \beta \, \Delta \dot{\boldsymbol{u}}_{ij}^{\perp,c} \right] . \qquad (6.5)$$

See Figure 6.2a for an illustration. The quantity $\Delta \boldsymbol{u}_{ij}^{\perp,c} = (\Delta \dot{u}_{ij}^{\perp} - \rho_i \dot{\theta}_i - \rho_j \dot{\theta}_j) (\hat{\boldsymbol{n}}_{ij} \times \hat{\boldsymbol{z}})$ is the tangential velocity at the contact and $\hat{\boldsymbol{z}}$ is the out-of-

plane unit vector. θ_i is the angular displacement of particle i from its orientation in the initial condition. Dots indicate differentiation with respect to time. The coefficient $k\tau_1$ controls the damping of relative normal motions. It is defined in terms of a microscopic time scale τ_1, which describes the exponential relaxation of two overlapping disks and sets the natural unit of time. The damping coefficient for relative transverse motion $\beta k\tau_1$ is defined by its ratio β to the damping coefficient for normal motion.

The case $\beta = 1$ describes equal damping of normal and transverse motion. For brevity we refer to this case as "balanced" contact damping. Examples of prior studies employing balanced contact damping include Refs. [13, 28, 76, 117, 118, 120, 140, 141]. Note that some of these studies apply damping to the relative motion of the particles' centers, neglecting particle rotations. We include rotations, as this seems more physical – however, we have also implemented balanced damping without rotations and find the form of G^* qualitatively unchanged from the results presented below.

We also separately consider the case $\beta = 0$, in which transverse motion goes undamped. This is not a physically realistic scenario for densely packed foams and emulsions. Nevertheless, this damping law is found in the literature, presumably because it exerts no torque, eliminating the need to keep track of rotational degrees of freedom.[142–145] In dilute systems with volume fractions outside the range considered here, this same force law is also a means to implement inelastic collisions.

Finally, we also treat the case of arbitrary β. We are not aware of any prior work that has systematically varied this coefficient.

Again for later convenience, we note that the Rayleigh dissipation function corresponding to Eq. (6.5) is

$$ R = \frac{1}{2}k\tau_1 \sum_{\langle ij \rangle} \left[\left(\Delta \dot{u}_{ij}^{\parallel} \right)^2 + \beta \left(\Delta \dot{u}_{ij}^{\perp,c} \right)^2 \right]. \qquad (6.6) $$

The Rayleigh dissipation function is used to implement linear damping forces in a Lagrangian formalism. Just as conservative forces are proportional to gradients of the potential energy, dissipative forces are proportional to gradients of the dissipation function.

Stokes-like drag forces: In addition to linear contact drag, we also consider a class of linear viscous force laws in which drag enters as a body force reminiscent of Stokes drag.[7, 146] These can be motivated in two ways.

In the first interpretation, drag between particles is neglected entirely. Instead drag is assumed to result from the motion of individual particles with respect to the continuous fluid phase, which itself is assumed to flow with an affine velocity profile $\boldsymbol{v}_{\text{aff}}(\boldsymbol{x}) = \dot{\gamma} y\,\hat{\boldsymbol{x}}$ set by the shear rate $\dot{\gamma}$. A particle at position $\boldsymbol{r}_i$ then experiences a drag force proportional to the difference

between its velocity v_i and the affine profile (see Figure 6.2b),

$$\boldsymbol{F}_i^{\text{visc}} = -k\tau_1 \left[\dot{\boldsymbol{u}}_i - \boldsymbol{v}_{\text{aff}}(\boldsymbol{r}_i) \right].$$ (6.7)

In this interpretation, the damping coefficient $k\tau_1$ should be proportional to the fluid viscosity η_F, as specified in Stokes' law. The dissipation function is

$$R = \frac{1}{2}k\tau_1 \sum_i \left[(\dot{u}_{i,x} - r_{i,y}^0 \dot{\gamma})^2 + \dot{u}_{i,y}^2 \right] + \frac{1}{2}\eta_F \dot{\gamma}^2 V.$$ (6.8)

The second term accounts for dissipation due to shearing of the continuous fluid phase.

   An alternative interpretation of Eq. (6.7) known as "mean field drag" was introduced by Durian.[7] In this view the body force is an approximation to balanced contact damping. One assumes that the velocity of each contacting particle j can be replaced with its average value at that position, which coincides with the affine velocity field. Angular velocities are set to zero. The resulting viscous force law and dissipation function are identical to Eqs. (6.7) and (6.8), with the caveat that $k\tau_1$ no longer has a fixed proportion to the fluid viscosity. Retaining the fluid viscosity term in the dissipation function is advisable, however, as otherwise the system could deform affinely without dissipating energy.

   Regardless of how the Stokes-like drag force is motivated, its advantage is again computational. As the equations of motion in the bubble model are overdamped, they are first order linear differential equations. Generally, these must be solved using matrix inversion (see below). However in the special case of Eq. (6.7), the relevant inversion can be performed by hand. Prior studies using Stokes or mean field drag include Refs. [7, 22, 75, 117, 119, 122, 132, 141, 147, 148]

Nonlinear contact forces: The viscous contact force law of Eq. 6.5 is linear in the particle velocities. However, viscous friction laws in real foams are actually nonlinear in the relative velocities. There are two classes of interactions, associated with so-called mobile and immobile surfactants, which give rise to different flow profiles within the thin films of the flow, and therefore dissipate energy differently. The case of immobile surfactants was treated by Bretherton,[129] whose drag law proportional to the $2/3$ power of velocity was subsequently verified experimentally.[149] More recently, Denkov and co-workers have argued for an exponent $1/2$ in the case of mobile surfactants.[130] Seth et al.[131] have also suggested a nonlinear force law with exponent $1/2$ to account for elastohydrodynamic interactions between deformable particles in soft glassy matter. We therefore consider force laws of the form

$$\boldsymbol{f}_{ij}^{\text{visc}} = -k\tau_1 \left(\frac{\Delta v_{ij}^c}{\rho_0/\tau_1} \right)^{\alpha-1} \Delta \boldsymbol{v}_{ij}^c,$$ (6.9)

where $\Delta \boldsymbol{v}_{ij}^{c} = \Delta \dot{\boldsymbol{u}}_{ij}^{\parallel} + \Delta \dot{\boldsymbol{u}}_{ij}^{\perp,c}$ is the relative velocity at the contact.

The constant ρ_0 has units of length and is required for dimensional consistency. We set it to 1. We will consider a range of exponents α, including the physically relevant values of $2/3$ and $1/2$.

6.2.3. *Equations of motion*

To solve for the complex shear modulus, it is useful to rewrite the equations of motion, Eq. (6.1), in matrix form. Following Ref. [13], the equations of motion can be expressed as

$$\hat{\mathcal{K}} \, |\boldsymbol{Q}(t)\rangle + \hat{\mathcal{B}} \, |\dot{\boldsymbol{Q}}(t)\rangle = |\boldsymbol{F}(t)\rangle \ . \tag{6.10}$$

The Hessian matrix $\hat{\mathcal{K}}$ and the damping matrix $\hat{\mathcal{B}}$ are defined in terms of the elastic potential energy U and the Rayleigh dissipation function R,

$$\mathcal{K}_{mn} = \left. \frac{\partial^2 U}{\partial Q_m \partial Q_n} \right|_{|\boldsymbol{Q}\rangle = |\boldsymbol{0}\rangle} \qquad \mathcal{B}_{mn} = \left. \frac{\partial^2 R}{\partial \dot{Q}_m \partial \dot{Q}_n} \right|_{|\dot{\boldsymbol{Q}}\rangle = |\boldsymbol{0}\rangle} \ . \tag{6.11}$$

The $3N + 1$-component vector $|\boldsymbol{Q}\rangle = (u_{1x}, u_{1y}, \ldots, \theta_1, \theta_2, \ldots, \gamma)$ contains all degrees of freedom, including the amplitude γ of the pure shear strain experienced by the box. The reference packing is defined as the state $|\boldsymbol{Q}\rangle = |\boldsymbol{0}\rangle$. The vector $|\boldsymbol{F}\rangle$ contains the generalized forces conjugate to each of the components of $|\boldsymbol{Q}\rangle$. The component conjugate to γ is equal to $\delta\sigma V = (\sigma - \sigma_0)V$, where σ is the shear stress.

The Fourier transform of Eq. (6.11) gives

$$\left(\hat{\mathcal{K}} + \imath\omega\hat{\mathcal{B}} \right) |\boldsymbol{Q}^*(\omega)\rangle = \delta\sigma \, V \, |\hat{\boldsymbol{\gamma}}\rangle \tag{6.12}$$

where ω is the angular frequency. Note that $|\boldsymbol{Q}^*(\omega)\rangle$ is complex. We impose a generalized forcing term pointing along the γ-coordinate, i.e. $|\boldsymbol{F}\rangle \propto |\hat{\boldsymbol{\gamma}}\rangle = (0, 0, \ldots, 1)$. All other generalized forces are zero (body forces and torques are balanced). The equations of motion are therefore reduced to a a set of complex linear equations which can be solved numerically for each frequency ω.

The complex shear modulus can be determined by solving Eq. (6.12) for the complex vector $|\boldsymbol{Q}^*(\omega)\rangle$ using standard linear algebra routines. The resulting shear strain is $\gamma^*(\omega) = \langle\hat{\boldsymbol{\gamma}}|\boldsymbol{Q}^*(\omega)\rangle$. The complex shear modulus is then

$$G^*(\omega) \equiv G'(\omega) + \imath G''(\omega) = \frac{\gamma^*(\omega)}{\delta\sigma} \ . \tag{6.13}$$

6.3. *Linear contact damping*

We now consider the complex shear modulus in the presence of linear contact damping. We begin with balanced damping, i.e. Eq. (6.5) for $\beta = 1$. This
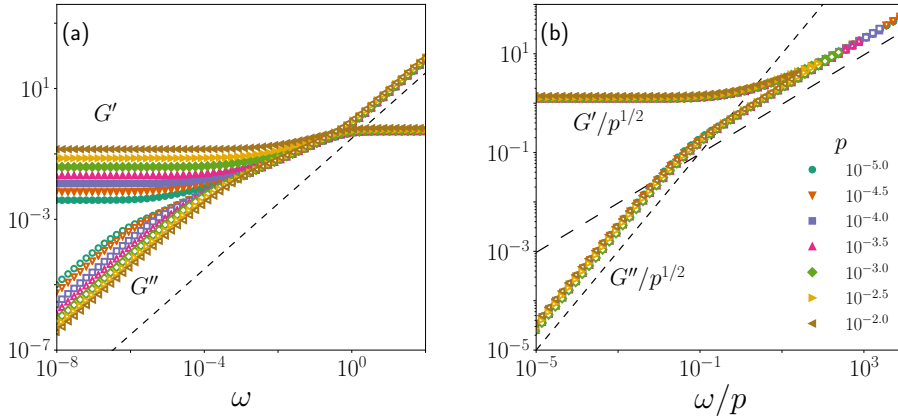
Figure 6.3: (a) The storage and loss moduli, G' and G'', for balanced contact damping ($\beta = 1$). The dashed line has slope 1. (b) Collapse of the same data to two critical scaling functions. The short- and long-dashed lines have slopes of 1 and 1/2, respectively.

scenario was already extensively studied in Ref. [13], and provides a useful point of comparison for alternative viscous force laws. Here we highlight the main results.

6.3.1. *Balanced damping*

Balanced linear contact damping was discussed above for the case $p = 10^{-4}$ – see Figure 6.1. We can gain further insight by varying the distance to jamming. In Figure 6.3a we plot the complex shear modulus as a function of frequency for a range of pressures $p = 10^{-5} \ldots 10^{-2}$. In all cases the same quasistatic, critical, and affine regimes identified in Figure 6.1 are evident. However the crossover frequency $\omega^* \equiv 1/\tau^*$ from the quasistatic to the critical regime shifts to lower values as $p \to 0$, indicating that the time scale τ^* diverges at the jamming point. The crossover from critical to high frequencies, on the other hand, is insensitive to pressure; it occurs for $\omega \sim \mathcal{O}(1)$ in all cases. We can infer that the quasistatic and critical regimes are intimately related to the jamming transition, while the high frequency response does not have a critical character.

Inspired by the above observation, we now restrict our focus to frequencies $\omega < 1$. A more rigorous derivation of the following results is found in Ref. [13]. Our approach here is more heuristic and begins with the scaling ansatz

$$\frac{G^*}{G_0} = \mathcal{G}^* \left(\omega \tau^* \right) \quad \text{for} \quad \omega < \mathcal{O}(1) , \tag{6.14}$$

which relates the dimensionless ratio G^*/G_0 to the dimensionless product $\omega \tau^*$. As discussed below, the quasistatic shear modulus scales as $G_0 \sim p^\mu$

with $\mu = 1/2$. Similarly, we assume that τ^* diverges at the jamming point,

$$\tau^* \sim \frac{1}{p^\lambda} \tag{6.15}$$

for some positive exponent λ. The real and imaginary parts of the scaling function $\mathcal{G}^* = \mathcal{G}' + \imath\mathcal{G}''$ satisfy

$$\mathcal{G}'(x) \sim \left\{ \begin{array}{ll} 1 & x < 1 \\ x^\Delta & x > 1 \end{array} \right. \tag{6.16}$$

and

$$\mathcal{G}''(x) \sim \left\{ \begin{array}{ll} x & x < 1 \\ x^\Delta & x > 1 \, . \end{array} \right. \tag{6.17}$$

The forms $\mathcal{G}' \sim 1$ and $\mathcal{G}'' \sim x$ for small x are the simplest choices respecting the symmetry properties of the storage and loss moduli, which are even and odd functions, respectively. The power laws $\mathcal{G}' \sim x^\Delta$ and $\mathcal{G}'' \sim x^\Delta$ represent non-trivial assumptions. The same exponent Δ must appear in both the real and imaginary parts to satisfy the Kramers-Kronig relations.

The scaling ansatz of Eqs. (6.14-6.17) is tested in Figure 6.3b, which plots G'/p^μ and G''/p^μ with $\mu = 1/2$ versus ω/p^λ with $\lambda = 1$. The resulting collapse is excellent. As expected, the real and imaginary parts of the scaling function are constant and linear, respectively, for low values of the rescaled frequency. There is a crossover around $\omega/p \sim \mathcal{O}(1)$ to a power law with exponent $\Delta \approx 0.5$ (long dashed line). This is the $\omega^{1/2}$ scaling discussed above.

The scaling collapse in Figure 6.3 empirically determines the values of the critical exponents; they are $\mu = 1/2$, $\lambda = 1$, and $\Delta = 1/2$. The value of μ is fixed by the known scaling of G_0. The exponent Δ is related to μ and λ. To see this, note that one generally expects the moduli to remain finite except possibly at the critical point, where both p and ω go to zero. In the case where $p = 0$ and $\omega > 0$, Eqs. (6.14-6.17) predict that both moduli scale as $p^{\mu-\lambda\Delta}\omega^\Delta$, which remains finite only if $\Delta = \mu/\lambda = 1/2$. It remains to motivate $\lambda = 1$, which we do in Section 6.3.3.

6.3.2. *"Imbalanced" contact damping ($\beta \neq 1$)*

In this section we probe the effects of undamped sliding motion, with emphasis on the limit $\beta = 0$. Our main result is to show that imbalanced damping "kills" dynamic critical scaling near jamming.

It is useful first to consider response in the absence of the pre-stress term, i.e. by setting $f_{ij}^0 = 0$ in Eq. (6.4). The Hessian and damping matrices are then directly proportional, $\hat{\mathcal{K}} = \tau_1\hat{\mathcal{B}}$, allowing Eq. (6.12) to be solved exactly in terms of G_0,

$$G^* = G_0(1 + \imath\tau_0\omega) \, . \tag{6.18}$$
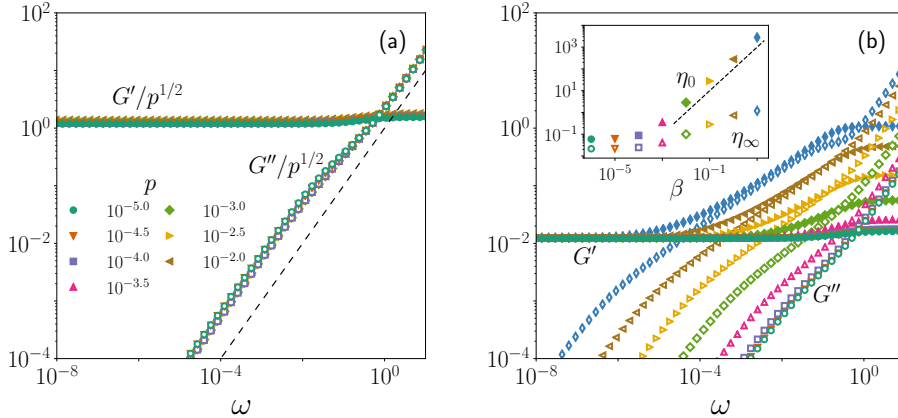
Figure 6.4: (a) Storage and loss modulus for a system without transverse damping ($\beta = 0$). (b) G' and G'' for systems at pressure $p = 10^{-4}$ and varying transverse damping β. (inset) Dynamic viscosity η_0 and affine viscosity η_∞ for the same data, denoting the low and high frequency limits of G''/ω. In both figures the dashed line has slope 1.

The resulting complex shear modulus is that of a Kelvin-Voigt element, the simplest viscoelastic solid – the storage modulus is flat, while the loss modulus is linear over the entire range of ω. Re-introducing the pre-stress term breaks the direct proportionality between $\hat{\mathcal{K}}$ and $\hat{\mathcal{B}}$, but produces only mild changes in the moduli, as shown in Figure 6.4a (open and filled squares). Moreover, data for a range of pressures close to the jamming point can all be collapsed by rescaling the storage and loss moduli by $p^{0.5}$. Note that the frequency axis does not need to be rescaled, indicating the absence of a diverging time scale.

We emphasize that a seemingly simple change to the viscous force law, namely setting the damping coefficient for sliding motion to zero, has produced a dramatic and qualitative shift in the viscoelastic response. More precisely, the intermediate regime, identified above when $\beta = 1$, has completely vanished. Recall that this regime is a manifestation of dynamic critical scaling and dominates the response for a wide range of frequencies near jamming. In this sense setting $\beta = 0$ kills dynamic critical scaling.

What happens for intermediate values of β? In Figure 6.4b we plot G^* for fixed p and a range of β over seven decades. One sees that the critical regime gradually appears, and for sufficiently large β the moduli resemble their form for $\beta = 1$. This suggests that it is reasonable to speak of weakly and strongly damped sliding motion. We quantify this distinction more precisely below.

6.3.3. *Relation to floppiness in quasistatic response*

The dynamic critical scaling of Eq. (6.14), and the critical exponent λ in particular, can be related to the scaling relations for normal, transverse,

and non-affine motion in quasistatic response. This link is motivated by the observation that for asymptotically low driving frequencies, the particles' trajectories must approach their quasistatic ($\omega \to 0$) form.

Packings at the jamming point are isostatic, meaning they have just enough contacts to constrain all particle motions (except for a few individual "rattlers", which can be removed from the analysis). Consider breaking a contact in a packing at the jamming transition, where all contacting particles are "kissing" and $f_{ij}^0 = 0$. The broken contact removes a constraint and therefore introduces a floppy mode, an infinitesimal motion of the particles that can be performed without work. By considering the energy expansion of Eq. (6.4), one sees that all relative normal motions in a floppy mode must be zero – floppy motions are sliding motions, in which all relative motion between particles is transverse to the contact. Jammed packings do not have floppy modes, but the eigenmodes of the Hessian remain "floppy-like," i.e. transverse/sliding motion dominates.[11, 14] This feature is also found in the response to shear, which is dominated by low frequency modes [13]. Through careful analysis of the modes, it is possible to show that the shear modulus scales as $G_0 \sim p^{1/2}$.[13**?**] Here we take this scaling relation as a given and, following Ref. [14], infer its consequences for the typical relative normal and transverse displacement amplitudes, $\Delta u^{\parallel}$ and $\Delta u^{\perp}$, as well as the typical amplitude of non-affine displacements u_{na}.

By definition, the change in elastic energy $\Delta U \equiv U - U_0$ due to an infinitesimal shear strain γ is $\Delta U = (1/2)G_0 V \gamma^2$. Momentarily neglecting the pre-stress term in Eq. (6.4), which should be small as $p \to 0$, we anticipate that the typical relative normal motion scales as $(\Delta u^{\parallel})^2 \sim G_0 \gamma^2$, or

$$\frac{\Delta u^{\parallel}}{\gamma} \sim p^{1/4} \,. \tag{6.19}$$

This scaling relation is consistent with our expectation that relative normal motion vanishes at the jamming point. We now re-introduce the non-positive pre-stress term in Eq. (6.4) in order to determine $\Delta u^{\perp}$. The first and second terms in brackets in Eq. (6.4) have typical values $(\Delta u^{\parallel})^2$ and $p(\Delta u^{\perp})^2$, respectively; in the latter case we have used the face that the typical force in the reference packing is proportional to the pressure. While mechanical stability requires the total energy change ΔU to be positive,[16] the system can minimize its deformation energy by organizing its motion to make the magnitude of the pre-stress term as large as possible – in other words, if the bound $p(\Delta u^{\perp})^2 \lesssim (\Delta u^{\parallel})^2$ is saturated. This gives

$$\frac{\Delta u^{\perp}}{\gamma} \sim \frac{1}{p^{1/4}} \,. \tag{6.20}$$

This relation relies on the (reasonable) assumption that the typical contact force scales linearly with the pressure. As expected, the amount of sliding motion grows dramatically and ultimately diverges as the system approaches the jamming point.
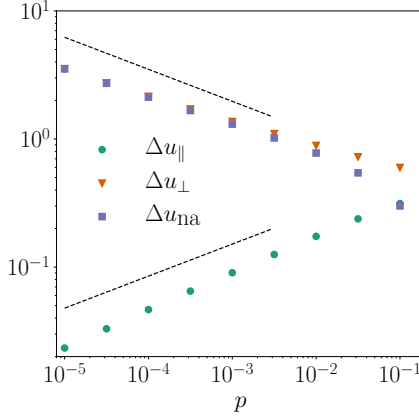
Figure 6.5: Scaling of the relative normal, relative transverse, and non-affine motion as a function of pressure. Dashed lines have slopes of $\pm 1/4$.

Finally, we consider the typical amplitude of non-affine displacements u_{na}. Bond vectors Δr_{ij}^{0} in the reference packing are randomly oriented, so there is a local competition between energetically favorable sliding at the particle scale, and globally imposed affine motion. Therefore we expect the typical non-affine amplitude to be comparable to the typical relative displacement amplitude, which is dominated by transverse motion, i.e.

$$\frac{u_{\mathrm{na}}}{\gamma} \sim \frac{1}{p^{1/4}} \, . \tag{6.21}$$

Hence non-affine motion is the natural consequence of floppy-like motion near jamming.

Eqs. (6.19-6.21) have previously been derived and tested numerically by Ellenbroek et al. and Wyart et al.[14, 21] For completeness we verify them again in Figure 6.5, which plots the median of the probability density function of $|\Delta u_{\parallel}|$, $|\Delta u_{\perp}|$, and $|u_{\mathrm{na}}|$ for varying p while neglecting the pre-stress term. Results including pre-stress show compatible trends, albeit with more noise; we revisit the role of pre-stress below. Plots of the means show the same trend for $\Delta u_{\perp}$ and u_{na}, but $\Delta u_{\parallel}$ develops a plateau at low p due to a long tail of the PDF.We now use the quasistatic relations (6.19-6.21) to determine the critical exponent λ. The $\omega \to 0$ limit of the dissipation function is proportional to the dynamic viscosity, $R = \eta_0(\omega\gamma_0)^2 V/2$, where γ_0 is the maximum strain amplitude. At the same time, from the viscous force law one anticipates $R \sim \boldsymbol{f}^{\mathrm{visc}} \cdot \Delta \boldsymbol{v} \sim \omega^2[(\Delta u^{\parallel})^2 + \beta(\Delta u^{\perp})^2]$. Invoking
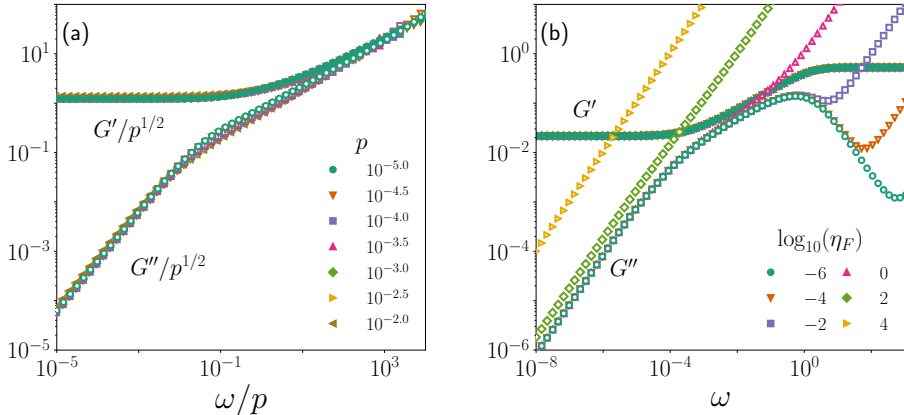
Figure 6.6: (a) Critical scaling collapse of the storage and loss moduli for Stokes drag and fluid viscosity $\eta_F = 1$. (b) Storage and loss moduli for $p = 10^{-4}$ and varying η_F.

Eqs. (6.19) and (6.20) gives

$$
\begin{aligned}
\eta_0 &\sim \left(\frac{\Delta u^\parallel}{\gamma_0} \right)^2 + \beta \left(\frac{\Delta u^\parallel}{\gamma_0} \right)^2 \\
&\sim (p/k)^{1/2} + \frac{\beta}{(p/k)^{1/2}} \, .
\end{aligned}
\tag{6.22}
$$

For balanced damping and $p \ll 1$, the second term dominates and $\eta_0 \sim 1/p^{1/2}$. Comparing to Eqs. (6.14-6.17), which require $\eta_0 = G_0\,\tau^* \sim p^{\mu - \lambda}$, it follows that $\lambda = 1$ and $\Delta = 1/2$. Hence we can motivate the exponents in the scaling functions (6.16) and (6.17).

Eq. (6.22) is compatible with our numerical results for undamped sliding ($\beta = 0$), as well. Then only the first term is present and $\eta_0 \sim p^{1/2}$ – it vanishes rather than diverges.

One can also consider the case of arbitrary β. The second term will always dominate for sufficiently low pressure; hence the dynamic viscosity diverges for any finite damping of sliding motion. In this sense the case $\beta = 0$ is singular. For arbitrary $\beta > 0$ the crossover frequency where the quasistatic regime ends and the linear regime begins scales as $\omega^* \sim p/\beta$. We have seen above that the critical regime ends at a frequency $\omega\tau_1 \sim \mathcal{O}(1)$. Hence the critical regime, with its $\omega^{1/2}$ scaling in G' and G'', is avoided entirely whenever $\omega^* \gg 1$, or $\beta \ll \beta^* \sim p$. This crossover is evident in Figure 6.4b. The scale β^* provides a convenient dividing line between cases of strong and weak damping of transverse motion.
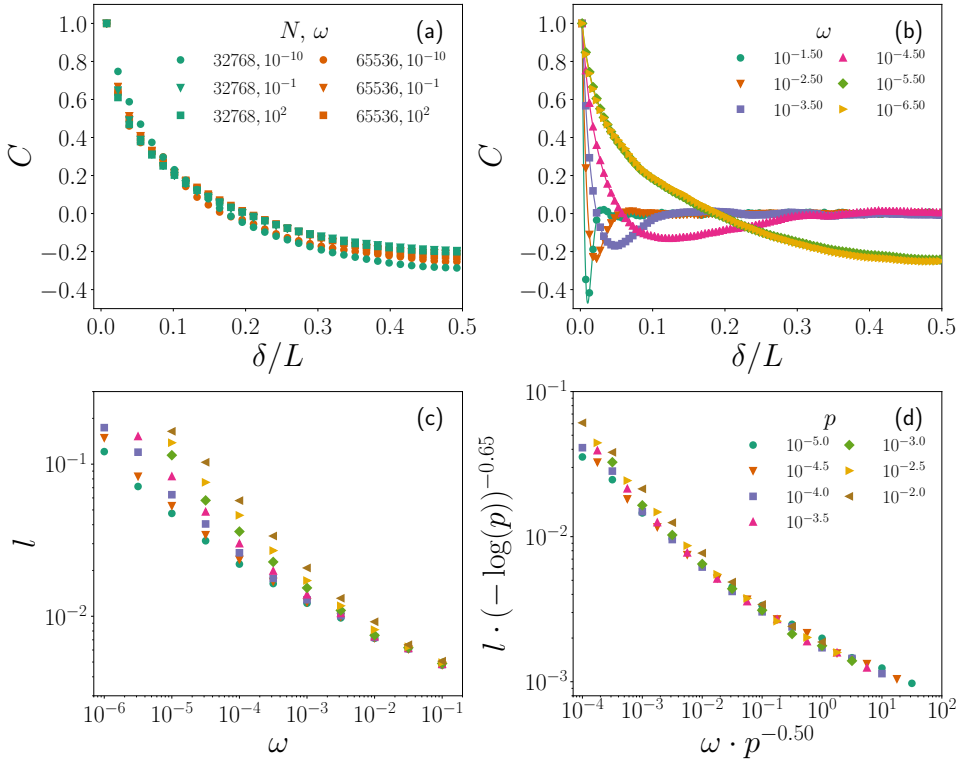
Figure 6.7: (a) Two-point correlation function C of the transverse (hence non-affine) particle displacements with balanced contact damping. (b) The same correlation function C for Stokes drag. (c) Length scale l corresponding to roots of the curves in (b). (d) Data collapse of l.

6.4. *Stokes Drag*

We now turn to the case of linear viscous body forces, i.e. the mean field or Stokes-like drag of Eq. (6.7). In Figure 6.6a we plot the complex shear modulus for Stokes drag for varying pressure and a fluid viscosity $\eta_F = 1$. We find dynamic critical scaling with the same critical exponents $\mu = 1/2$, $\lambda = 1$, and $\Delta = 1/2$ as for balanced contact drag. Hence it appears that Stokes drag falls into the same universality class as strongly damped relative transverse motion.

As in the previous section, the above result can be rationalized on the basis of quasistatic scaling relations. The key observation is that the typical non-affine motion u_{na} and the relative transverse motion $\Delta u^\perp$ diverge in the same way as the pressure tends to zero; *cf.* Eqs. (6.20) and Eq. (6.21). For Stokes drag the dissipation function scales as $R \sim (u_{\mathrm{na}}\omega)^2$, again giving $\eta_0 \sim (p/k)^{-1/2}$.

Recall that if one considers the Stokes drag term to be a mean field

approximation for balanced contact damping, then the fluid viscosity η_F can vary independently of the damping coefficient $k\tau_1$. We probe the dependence of G^* on η_F in Figure 6.6b by varying η_F over ten decades. We observe that the fluid viscosity contributes a linear term $\eta_F\omega$ to the loss modulus, which is always dominant at sufficiently high frequencies. For large η_F and/or low pressures satisfying $\eta_F \gg 1/p^{1/2}$, the loss modulus becomes linear for all frequencies. In this event the critical properties of the loss modulus are obscured, but criticality is still apparent in the storage modulus.

6.4.1. *Correlations*

Despite the similarity in their viscoelastic response, we find a striking difference in the spatial correlations of non-affine displacements between the cases of linear viscous body forces and balanced contact damping.

For a system undergoing simple shear in the x-direction, correlations of the non-affine displacements between particles separated by a distance $\delta_{ij} = |x_i - x_j|$ can be quantified with the two-point correlation function $C = \langle u'_{i,y}(x_i)\, u'_{j,y}(x_i + \delta_{ij}) \rangle / \langle (u'_{i,y})^2 \rangle$. Here $u'_{i,y}$ is the y-component of the real part of the complex displacement vector of particle i with x-coordinate x_i. The average $\langle \cdot \rangle$ runs over all particle pairs within a narrow "lane", hence C is a function of $|\delta_{ij}|$. We have verified that C becomes independent of the lane width for sufficiently small values. We have also confirmed that results using the imaginary part $u''_{i,y}$ are indistinguishable.

Non-affine correlation functions in weakly jammed solids have been studied previously for three cases. DiDonna and Lubensky[150] and Maloney[31] showed there is no characteristic length scale in quasistatic linear elastic response; instead C collapses when distances are rescaled by the box size L. Heussinger and Barrat found compatible results for quasistatic shear flow. Olsson and Teitel[75] found that the same correlation function does select a growing length scale, independent of L, in shear flow at finite rate using Stokes drag. However Tighe et al.[151] showed that the form of C resembles quasistatic linear response when one uses balanced contact damping instead of Stokes drag. Hence there remain important open questions about correlations at finite driving rate and the role of the viscous force law. Here we fill a gap in the literature, namely linear response at finite rates.

In Figure 6.7a we plot C for balanced contact damping at a single pressure, two system sizes, and three values of the frequency ω separated by twelve decades. There is a monotonic decay of the correlations, with little dependence on the frequency. The shape is also independent of the pressure (not shown). The data collapse when plotted as a function of δ/L. Hence two-point displacement correlations provide no evidence of a growing length scale near jamming; snapshots of the velocities display "swirls" with a characteristic radius of approximately one quarter of the box size.

Correlations for Stokes-like drag display a strikingly different shape, as shown in Figure 6.7b. C possesses a minimum that shifts to larger distances with decreasing ω. For the lowest plotted frequencies, $\omega = 10^{-5.5}$
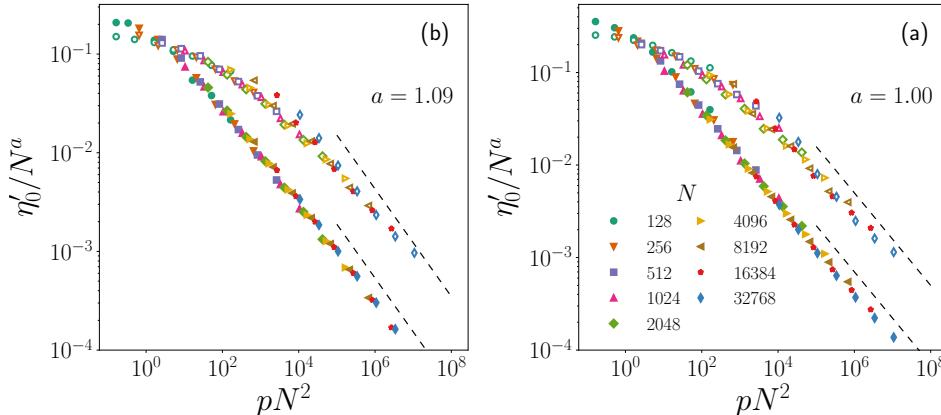
Figure 6.8: Finite size scaling collapse of the dynamic viscosity η_0 for (a) balanced contact damping and (b) Stokes drag. Filled/open data points are calculated with/without pre-stress. Dashed curves have a slope of $-a/2$, with a indicated in the plot.

and $10^{-6.5}$, the minimum is no longer clearly identifiable and the shape of C begins to resemble the form for balanced contact damping. One can define a correlation length l from the point where C crosses the x-axis, plotted in Figure 6.7c. We find a length scale that grows with decreasing frequency, before reaching a plateau with a height of approximately $L/4$. Focusing on length scales below this plateau, we find empirically that a reasonable data collapse is achieved by plotting $l/(-\ln p)^{0.65}$ versus $\omega/p^{0.5}$, implying that the length scale would diverge at the jamming point ($p \to 0$ and $\omega \to 0$) in thermodynamically large systems. We note that log corrections are typical in systems at their upper critical dimension, which is indeed $D = 2$ for the jamming transition.[65, 69].

The takeaway is that the form of the correlation function at finite rate is strongly sensitive to the viscous force law. For balanced contact damping there is no evidence of a diverging length scale. For Stokes drag there is a growing correlation length that is cut off by the box size as the frequency is sent to zero.

6.4.2. *Finite Size Effects*

Elastic moduli and the mean coordination number of marginally jammed matter are known to be influenced by finite size effects.[16, 28, 65, 69, 152] In quasistatic systems they become important when the pressure p is comparable to the pressure increment $p^* \sim 1/N^2$ required to add a contact to, or remove a contact from, the packing. Here we show that the same pressure scale governs finite size effects in the dynamic viscosity η_0.

In Figure 6.8 the dynamic viscosities for both balanced contact damping and Stokes drag ($\eta_F = 1$) are plotted for a wide range of pressures and

system sizes, both with pre-stress (open symbols) and without pre-stress (filled symbols). In all cases, we find that the data collapse to a master curve when η_0/N^a is plotted versus $p/p^* \sim pN^2$, implying $\eta_0 \sim 1/p^{a/2}$. For balanced contact damping, we find the best collapse when $a = 1.0$, consistent with the scaling $\eta_0 \sim 1/p^{1/2}$ determined above. For Stokes drag we find better collapse for the somewhat higher value $a = 1.09$. For comparison, we also plot curves with slope $-a/2$. Provided that η_0 is an intensive material property, as is typically the case, the master curves must approach this slope for large system sizes. This condition is met for the contact damping data, but for Stokes drag the collapsed data have a slightly shallower slope, particularly for the data with pre-stress. Using a lower value of α brings $-a/2$ closer to the observed slope, but the data collapse is somewhat worse. Given the small difference in these values and the scatter in our data, we consider it likely that α is in fact equal to 1 for Stokes drag. However, on the basis of present data we cannot exclude the possibility that $a > 1$ for Stokes drag, or that η_0 has a weak system size dependence.

For both contact damping and Stokes drag, pre-stress plays a role in the onset of finite size effects. Whereas the data without pre-stress show a sharp crossover around $pN^2 \sim \mathcal{O}(1)$, the crossover in the data with pre-stress is much more gradual. Even for $pN^2 > 10^3$, a naïve power-law fit to η_0 versus p would yield a slope that is too shallow. Therefore studying the results of simulations with and without pre-stress, side-by-side, can potentially improve the assessment of critical exponents near jamming at modest system sizes.

6.5. *Nonlinear Damping*

The drag forces considered in the previous sections are all linear in the particle velocities. Compared to nonlinear drag laws, linear forces are easier and cheaper to simulate. However, theory [129–131] and experiments [149] indicate that the bubble-bubble viscous force in foams (and so likely emulsions, as well) is in fact nonlinear in the relative velocity, as in Eq. (6.9). We now probe the influence of an exponent $\alpha \neq 1$ on the complex shear modulus. Our main result is that the time scale τ_1 must be generalized to account for a nontrivial frequency dependence. As a result, the frequency dependence of both the storage and the loss modulus changes.

Nonlinear equations of motion cannot be written as a matrix equation in terms of $\hat{\mathcal{K}}$ and $\hat{\mathcal{B}}$. Molecular dynamics simulations are an option,[132] but beyond the scope of the present work. Instead, we turn to an approximation known as the method of equivalent damping. The central idea of the approximation is to replace the nonlinear force law with an "equivalent" linear force law with a frequency dependent effective damping coefficient $k\tau_\alpha$,

$$\boldsymbol{f}_\alpha^{\text{eff}} = -k\tau_\alpha \, \Delta \boldsymbol{v}^{\,c} \,. \tag{6.23}$$

The effective damping coefficient is expressed in terms of a microscopic time scale τ_α that depends on the frequency and amplitude of the forcing, as described below. τ_α generalizes τ_1, the constant time scale for $\alpha = 1$.

We now apply the method of equivalent damping to a single degree of freedom system, namely an overdamped oscillator driven by a sinusoidal force with amplitude F_0 and frequency ω. For the effective damping law of Eq. (6.23), the resulting oscillations have an amplitude

$$u_0 = \frac{F_0}{k} \left[\frac{1}{1 + (\omega \tau_\alpha)^2} \right]^{1/2} .$$ (6.24)

To fix τ_α, we require that the energy dissipated by $\boldsymbol{f}_\alpha^{\text{eff}}$ during one period is equal to the energy dissipated by the nonlinear force law (6.9) when the particle is constrained to follow the same trajectory through phase space. One finds

$$\tau_\alpha(\omega) = \frac{2\tau_1^\alpha}{\sqrt{\pi}} \left(\frac{u_0 \omega}{\rho_0} \right)^{\alpha-1} \frac{\Gamma\left(1 + \frac{\alpha}{2}\right)}{\Gamma\left(\frac{3}{2} + \frac{\alpha}{2}\right)} .$$ (6.25)

This is an implicit relation, as u_0 depends on τ_α. Separately considering the low and high frequency limits gives

$$\tau_\alpha = \begin{cases} 1/(F_0 \omega)^{1-\alpha} & \omega < \omega_\times \\ 1/F_0^{(1-\alpha)/\alpha} & \omega > \omega_\times , \end{cases}$$ (6.26)

with a crossover frequency $\omega_\times \sim F_0^{(1-\alpha)/\alpha}$.

To extend the above insights to soft sphere packings, we make an additional but reasonable assumption that the typical induced force on each contact is proportional to the applied stress, $F_0 \sim \delta\sigma$. Under this assumption, the scaling ansatz (6.14-6.17) remains valid, provided that one takes $\tau^* \sim \tau_\alpha/p$, instead of τ_1/p. Because τ_α is a function of frequency and the applied stress, the "bare" storage and loss moduli G' and G'' (as opposed to $\mathcal{G}'$ and $\mathcal{G}''$) inherit new dependences on ω and $\delta\sigma$. For systems near jamming and the physically relevant case $\alpha < 1$, $1/\tau^*$ is always smaller than $\omega_\times$ and hence $\tau_\alpha \sim (\delta\sigma\,\omega)^{\alpha-1}$ in the quasistatic and critical regimes. In the quasistatic regime one finds that the storage modulus $G' \simeq G_0$ is unchanged, while the loss modulus becomes

$$G'' \sim \frac{1}{\delta\sigma^{1-\alpha}} \frac{\omega^\alpha}{p^{1/2}} .$$ (6.27)

As in the linear case, the loss modulus in the quasistatic regime "trivially" reflects the form of the viscous force law, i.e. both scale as ω^α. G'' also no longer displays linear response, as it depends on the applied stress. In the critical regime one finds

$$G' \sim \frac{\omega^{\alpha/2}}{\delta\sigma^{(1-\alpha)/2}}$$ (6.28)

and likewise

$$G'' \sim \frac{\omega^{\alpha/2}}{\delta\sigma^{(1-\alpha)/2}} \; . \tag{6.29}$$

We emphasize that the $\omega^{1/2}$ scaling of the linear case has been generalized to $\omega^{\alpha/2}$. Hence within the method of equivalent damping, the nonlinear frequency dependence of G^* in viscous soft spheres contains a nontrivial dependence on the exponent α of the nonlinear viscous force law.

6.6. *Conclusions*

We have shown that the viscoelastic response of viscous soft sphere packings close to jamming depends qualitatively on the damping law. The extent to which damping couples to floppy-like, and hence non-affine, motion is a key determinant of the resulting response. When the coupling is strong, as for balanced linear contact damping or Stokes-like drag with $\eta_F = 1$, the viscoelastic response displays dynamic critical scaling, including square root scaling of the storage and loss moduli over a broadening range of frequencies. When the coupling is weak, as when $0 < \beta < \beta^*$ for contact damping or when $\eta_F > 1/p^{1/2}$ for Stokes-like drag, aspects of the critical response are obscured. And when floppy-like motion is completely undamped, as for $\beta = 0$, dynamic critical scaling vanishes entirely. We demonstrated a subtle interplay between the force law and non-affine correlations. For systems with contact damping, the only length scale identified by two-point correlation functions is the box size. However, in systems with Stokes drag, we observe a correlation length that diverges with vanishing ω, with a cutoff at the box size. Finally, we presented numerical evidence that pre-stress increases the strength of finite size effects.

We have also made predictions for the viscoelastic response in the presence of nonlinear drag laws. Within the context of the method of equivalent damping, we find that dynamic critical scaling survives; however the scaling of the bare storage and loss moduli now depends on the microscopic exponent α. This provides a novel way to infer properties of the dominant dissipative mechanism at the particle scale from the frequency dependence of G^*. As the method of equivalent damping is an approximation, these predictions require further testing. As a basic check, we have verified Eq. (6.27-6.29) by directly inserting the effective damping coefficient from Eq. (6.26) in the linear equations of motion. Of course this does not constitute an independent test of the method of equivalent damping, which would require, e.g., molecular dynamics simulations of Durian's bubble model. We leave this as an important task for future work.

Our results suggest that, when performing numerical studies of jammed matter, one must take care to match the form of the viscous force law to the physics of whatever particular material one wishes to model – growing correlations do not wash out this detail. In particular, the linear contact damping law with $\beta = 0$ should be avoided, as it significantly alters the

viscoelastic response and is difficult to justify on physical grounds, at least
in the context of foams, emulsions, and soft colloidal particles.

6

7

Conclusion and Outlook

In this thesis we investigated the mechanics of marginal solids and can group our findings in terms of length, strain, and time scales. For each of these we investigated how they scale with the distance to the isostatic point and related this scaling to what we know about the linear response of packings/networks close to isostaticity. The most important key feature is the fact that the linear response is dominated by transverse relative motion as well as the scaling of shear and bulk moduli. Our main findings regarding length, strain, and time scales follow.

Length Scales: In Chapter 3 we measured diverging length scales in the linear response of soft sphere packings close to isostaticity. In these systems it is not straightforward to measure diverging length scales in the linear response. Pair correlation functions only yield length scales which directly scale with the size of the system [153]. While many other groups succeeded in measuring ℓ_c or ℓ^* separately with distinct methods [9, 11, 12], we were able to find both length scales in the fluctuations of the linear response. In this sense Chapter 3 gives a thorough characterization of length scales which can be found in the linear response of soft sphere packings. Furthermore, it is important to note that the method which we presented is model-free. It does not rely on fitting and therefore the assumption of an empirical constitutive relation. We directly measure the Fourier transform of the moduli which gives information about their spatial dependence. So far in most applications one assumes a stress strain relation with a set of parameters (which often lack physical insight) and determines them by fitting to experimental or simulation data. With the method introduced in Chapter 3 this is not necessary. In addition, it is straightforward to apply the method to consider other materials.

Noteworthy in the context of this thesis is the application of the method to RC networks. For these networks it would be interesting to do the same simulations as we did for PD networks. The interesting difference between the two systems is the scaling in the bulk modulus. Because the bulk modulus in RC networks vanishes continuously [71] like the shear modulus, we expect differences in the modulus $\hat{S}_\parallel$ which is connected to compression. For the same reason the length scale found in the fluctuations in the linear response to sinusoidal compression is also expected to behave differently.

The application to Mikado networks is also of potential interest because one could numerically test the assumptions made in [87]. If the bending stiffness and the density of the filaments is low, the system's response is strongly non-affine. In this case measurements of the wavenumber dependent moduli are expected to show signs of a nonlocal length scale of the order of a filament length. In the case of high bending stiffness one would expect to find a nonlocal length scale which is of the order of the segment size.

Strain Scales: The Chapter 4 and 5 are about the nonlinear behavior of the response of networks to shear deformations. In Chapter 4 we investigated how the shear response of hypostatic random spring networks develops as an external perturbing field is applied. We tested two different network models, RC networks and Mikado networks and two types of perturbing fields, bending interactions and pre-stress. We measured the shear modulus as a function of the distance to the isostatic point and as a function of the amplitude of the perturbing field. Our findings show that although the network models and perturbing fields we considered seem very different at first, the shear response shows surprising similarities in all cases. We explain these similarities with the density of states and variational arguments.

In Chapter 5 we considered the shear response of hyperstatic PD and RC networks. We investigated the Poynting effect which is a nonlinear effect that describes the build-up of normal stresses as a shear strain is applied. (Or the volume change of the system as a shear stress is applied.) We successfully predicted the sign and the scaling of the Poynting effect using only properties of the linear response regime. As a final step we numerically measured the scaling of characteristic strain scales on which shear stiffening occurs and connected this stiffening behavior to the Poynting effect.

The theoretical framework we presented in Chapter 5 can be used to consider any hyperelastic medium. While we checked two network models in this thesis the framework could be adapted to Mikado networks. The scaling of Λ^2 and the shape of the density of states are determined in Chapter 4 which are already two important ingredients to determine the scaling of the amplitude of the Poynting effect. The only part missing is the Grüneisen parameter.

In fact, considering Mikado networks in the nonlinear shear regime would also involve ideas developed in Chapter 4 since we are then dealing with a hypostatic network which is rigidified by a perturbing field. One of the main differences is the shape of the density of states, which also features a sharp peak for low eigenfrequencies. While we focused on the nonlinear elasticity of systems which are approximated well by a hyperelastic medium, it would be interesting to also investigate the Poynting effect for particulate matter (where it is usually referred to as dilatancy). When soft sphere packings are sheared hyperelasticity is violated because of the change in the contact network - which means that the theoretical methods used in Chapter 5 cannot be applied. However, it is still possible to consider the packings with simulations.

Furthermore, it would be interesting to test more systems for the behavior we find in Chapter 4. Candidates would be hypostatic networks which are rigidified by a population of weak springs [21] or soft sphere packings in which a fraction of the particles is softer.

7

Time Scales: Chapter 6 is about the linear viscoelastic response of soft sphere packings. Here we found that the critical scaling in the dynamical modulus G^* depends on the details of the damping law used. In the case of a viscous force law which damps only normal relative motion the critical scaling regime does not exist and therefore no diverging time scale in the linear shear response can be found. In the case of Stokes drag and contact damping which damps both normal and transverse relative motion we found the expected critical scaling regime in G^*. However, we showed that the damping law also influences the two point correlation function of the linear response. With Stokes drag we found a diverging length scale in the linear response while we could only measure length scales of the order of the system size if contact damping is used.

Our findings show that it is important to bear in mind that damping has strong qualitative influence on the linear response of soft sphere packings. It is therefore important to adjust the simulation model such that it captures the essential physics of the system in question. Especially in foams where the exact form of the damping law depends on what kind of surfactants are used [130, 154, 155] the exponent of the damping law is influenced. Here it can be important to consider simulations with nonlinear damping laws. Our results for the nonlinear damping laws rely on approximations, however. It would be of benefit to also test our findings with molecular dynamics simulations.

7

A

Nonlocal Elasticity - Green's Function

In the main text we studied the case where forcing is restricted to a single wave vector $q\hat{\boldsymbol{y}}$. Here we generalize to arbitrary wave vector $\boldsymbol{q} = (q_x, q_y)^T \equiv q(n_x, n_y)^T$ and derive expressions for the fourth order compliance tensor $\widetilde{S}_{ijkl}(\boldsymbol{q})$ that connects strain $\widetilde{\epsilon}_{ij}(\boldsymbol{q})$ and stress $\widetilde{\sigma}_{kl}(\boldsymbol{q})$,

$$\widetilde{\epsilon}_{ij}(\boldsymbol{q}) = \widetilde{S}_{ijkl}(\boldsymbol{q})\,\widetilde{\sigma}_{kl}(\boldsymbol{q})\,, \tag{A.1}$$

with summation implied. The strain in response to arbitrary stress can then be given by the inverse Fourier transform of $\widetilde{S}_{ijkl}(\boldsymbol{q})\,\widetilde{\sigma}_{kl}(\boldsymbol{q})$.

We first consider relations between the force density field $\widetilde{\boldsymbol{f}}(\boldsymbol{q})$ and displacement field $\widetilde{\boldsymbol{u}}(\boldsymbol{q})$, i.e. the Green's function $\widetilde{\boldsymbol{G}}(\boldsymbol{q})$. We then turn to strain-stress relations.

A

A.1. *Green's function*

As shown in the main text, $\widetilde{S}_\parallel(q)$ and $\widetilde{S}_\perp(q)$ characterize the response to forcing parallel and transverse to $\boldsymbol{q}$, respectively. In an isotropic material the microstructure does not select any particular directions in space, hence for arbitrary $\boldsymbol{q}$ we have

$$
\begin{aligned}
q^2\widetilde{\boldsymbol{u}}_\parallel(\boldsymbol{q}) &= \widetilde{S}_\parallel(q)\widetilde{\boldsymbol{f}}_\parallel(\boldsymbol{q}) \\
q^2\widetilde{\boldsymbol{u}}_\perp(\boldsymbol{q}) &= \widetilde{S}_\perp(q)\widetilde{\boldsymbol{f}}_\perp(\boldsymbol{q})\,.
\end{aligned}
\tag{A.2}
$$

Note that the compliances depend on q but not the orientation of the wave vector. In the remainder we suppress dependences on q, n_x, and n_y in order to keep expressions compact.

The displacement-force relation is

$$
q^2\left(\widetilde{\boldsymbol{u}}_\parallel + \widetilde{\boldsymbol{u}}_\perp\right) = q^2\widetilde{\boldsymbol{u}} = \widetilde{S}_\parallel\widetilde{\boldsymbol{f}}_\parallel + \widetilde{S}_\perp\widetilde{\boldsymbol{f}}_\perp\,.
\tag{A.3}
$$

The above can be rewritten by introducing the matrices

$$
\hat{M}_\parallel = \begin{pmatrix} n_x^2 & n_x n_y \\ n_x n_y & n_y^2 \end{pmatrix}
\tag{A.4}
$$

and

$$
\hat{M}_\perp = \hat{\mathbb{1}} - \hat{M}_\parallel = \begin{pmatrix} n_y^2 & -n_x n_y \\ -n_x n_y & n_x^2 \end{pmatrix}
\tag{A.5}
$$

to give

$$
q^2\widetilde{\boldsymbol{u}} = \left(\widetilde{S}_\parallel\hat{M}_\parallel + \widetilde{S}_\perp\hat{M}_\perp\right)\widetilde{\boldsymbol{f}}(\boldsymbol{q}) \equiv \widetilde{\boldsymbol{G}}\widetilde{\boldsymbol{f}}\,.
\tag{A.6}
$$

Here

$$
\frac{\widetilde{G}_{ij}}{q^2} = \frac{1}{q^2}\left[\widetilde{S}_\perp\delta_{ij} + (\widetilde{S}_\parallel - \widetilde{S}_\perp)n_i n_j\right]
\tag{A.7}
$$

is the Green's function. Note that the Green's function of a classical elastic continuum is recovered when $\widetilde{S}_\parallel = 1/(K+G)$ and $\widetilde{S}_\perp = 1/G$, independent of q, where G and K are the shear and bulk modulus, respectively.

A.2. *Strain-stress relation*

The Green's function prescribes the nonlocal strain-stress relation. The strain tensor and displacement field are connected by:

$$
\epsilon_{ij} = \frac{1}{2}\left(\frac{\partial u_i}{\partial x_j} + \frac{\partial u_j}{\partial x_i}\right)
\tag{A.8}
$$

or, in Fourier space,

$$
\widetilde{\epsilon}_{ij} = \frac{\iota q}{2}\left(n_i\widetilde{u}_j + n_j\widetilde{u}_i\right)\,.
\tag{A.9}
$$

A

Similarly, the equilibrium condition

$$\frac{\partial \sigma_{ij}}{\partial x_i} = -f_j \, , \tag{A.10}$$

or equivalently

$$\widetilde{f}_j = -\imath q n_i \widetilde{\sigma}_{ij} \, , \tag{A.11}$$

relates the stress tensor and the force density. The two above relations, together with (A.6), allow the compliance tensor $\widetilde{S}_{ijkl}$ to be written in terms of the elements of the Green's function:

$$\widetilde{\epsilon}_{ij} = \underbrace{\frac{1}{2}\left(n_i \widetilde{G}_{jk} n_l + n_j \widetilde{G}_{il} n_k \right)}_{\widetilde{S}_{ijkl}} \widetilde{\sigma}_{kl} \tag{A.12}$$

0 The constitutive relation can be (re-)written compactly using Voigt notation. Defining

$$\widetilde{\boldsymbol{f}} = \begin{pmatrix} n_x & 0 & n_y \\ 0 & n_y & n_x \end{pmatrix} \widetilde{\boldsymbol{\sigma}} \equiv \hat{D}\widetilde{\boldsymbol{\sigma}} \quad \text{and} \quad \widetilde{\boldsymbol{\epsilon}} = \hat{D}^T \widetilde{\boldsymbol{u}} \tag{A.13}$$

with $\widetilde{\boldsymbol{\sigma}} = (\widetilde{\sigma}_{xx}, \widetilde{\sigma}_{yy}, \widetilde{\sigma}_{xy})^T$ and $\widetilde{\boldsymbol{\epsilon}} = (\widetilde{\epsilon}_{xx}, \widetilde{\epsilon}_{yy}, 2\widetilde{\epsilon}_{xy})^T$, the constitutive relation becomes $\widetilde{\boldsymbol{\epsilon}} = \hat{\widetilde{S}} \cdot \widetilde{\boldsymbol{\sigma}}$, with the compliance matrix

$$\hat{\widetilde{S}} \equiv \hat{D}^T \hat{\widetilde{G}} \hat{D} =$$
$$\begin{pmatrix} (\widetilde{S}_\| n_x^2 + \widetilde{S}_\perp n_y^2)n_x^2 & (\widetilde{S}_\| - \widetilde{S}_\perp)n_x^2 n_y^2 & 2(\widetilde{S}_\| - \widetilde{S}_\perp)n_x^3 n_y + S_\perp n_x n_y \\ (\widetilde{S}_\| - \widetilde{S}_\perp)n_x^2 n_y^2 & (\widetilde{S}_\| n_y^2 + \widetilde{S}_\perp n_x^2)n_y^2 & 2(\widetilde{S}_\| - \widetilde{S}_\perp)n_x n_y^3 + S_\perp n_x n_y \\ 2(\widetilde{S}_\| - \widetilde{S}_\perp)n_x^3 n_y + S_\perp n_x n_y & 2(\widetilde{S}_\| - \widetilde{S}_\perp)n_x n_y^3 + S_\perp n_x n_y & 4(\widetilde{S}_\| - \widetilde{S}_\perp)n_x^2 n_y^2 + \widetilde{S}_\perp \end{pmatrix}.$$
$$\tag{A.14}$$

The q-dependence of $\widetilde{S}_\|$ and $\widetilde{S}_\perp$ is that given in Figs. 2 and 3 of the main text. To recover the stress gradient expansion discussed in the text, one Taylor expands the compliances,

$$\widetilde{S}_\|(q) = \widetilde{S}_\|(0)[1 + (\ell_\| q)^2 + \ldots]$$
$$\widetilde{S}_\perp(q) = \widetilde{S}_\perp(0)[1 + (\ell_\perp q)^2 + \ldots]$$
$$\tag{A.15}$$

truncates after the quadratic term in q, and considers $\boldsymbol{q} = q\hat{\boldsymbol{y}}$.

Bibliography

[1] G. Katgert, B. P. Tighe, and M. van Hecke, *The jamming perspective on wet foams,* Soft Matter **9**, 9739 (2013).

[2] J. G. Berryman, *Random close packing of hard spheres and disks,* Phys. Rev. A **27**, 1053 (1983).

[3] C. S. O'Hern, L. E. Silbert, A. J. Liu, and S. R. Nagel, *Jamming at zero temperature and zero applied stress: The epitome of disorder,* Phys. Rev. E **68**, 011306 (2003).

[4] A. J. Liu and S. R. Nagel, *Nonlinear dynamics: Jamming is not just cool any more,* Nature **396**, 21 (1998).

[5] M. Wyart, *On the rigidity of amorphous solids,* Ann. Phys. Fr. **30**, 1 (2005).

[6] A. J. Liu and S. R. Nagel, *The jamming transition and the marginally jammed solid,* Annu. Rev. Condens. Matter Phys. **1**, 347 (2010).

[7] D. J. Durian, *Foam mechanics at the bubble scale,* Phys. Rev. Lett. **75**, 4780 (1995).

[8] M. van Hecke, *Jamming of soft particles: Geometry, mechanics, scaling and isostaticity,* J. Phys. Condens. Matter **22**, 033101 (2010).

[9] L. E. Silbert, A. J. Liu, and S. R. Nagel, *Diverging length scales near the jamming transition,* Phys. Rev. Lett. **95**, 098301 (2005).

[10] M. Wyart, S. R. Nagel, and T. A. Witten, *Geometric origin of excess low-frequency vibrational modes in weakly connected amorphous solids,* EPL **72**, 486 (2005).

[11] W. G. Ellenbroek, E. Somfai, M. van Hecke, and W. van Saarloos, *Critical scaling in linear response of frictionless granular packings near jamming,* Phys. Rev. Lett. **97**, 258001 (2006).

[12] E. Lerner, E. DeGiuli, G. Düring, and M. Wyart, *Breakdown of continuum elasticity in amorphous solids,* Soft Matter **10**, 5085 (2014).

[13] B. P. Tighe, *Relaxations and rheology near jamming,* Phys. Rev. Lett. **107**, 158303 (2011).

[14] W. G. Ellenbroek, M. van Hecke, and W. van Saarloos, *Jammed frictionless disks: Connecting local and global response,* Phys. Rev. E **80**, 061307 (2009).

[15] J. Maxwell, *On the calculation of the equilibrium and stiffness of frames,* Philosoph. Mag. **27**, 294 (1864).

[16] S. Dagois-Bohy, B. P. Tighe, J. Simon, S. Henkes, and M. van Hecke, *Soft-sphere packings at finite pressure but unstable to shear,* Phys. Rev. Lett. **109**, 095703 (2012).

[17] N. W. Ashcroft and N. D. Mermin, *Solid state physics (Saunders College, Philadelphia, 1976).*

[18] D. M. Sussman, C. P. Goodrich, and A. J. Liu, *Spatial structure of states of self stress in jammed systems,* Soft matter **12**, 3982 (2016).

[19] L. Yan, E. DeGiuli, and M. Wyart, *On variational arguments for vibrational modes near jamming,* EPL **114**, 26003 (2016).

[20] H. Mizuno, K. Saitoh, and L. E. Silbert, *Elastic moduli and vibrational modes in jammed particulate packings,* Phys. Rev. E **93**, 062905 (2016).

[21] M. Wyart, H. Liang, A. Kabla, and L. Mahadevan, *Elasticity of floppy and stiff random networks,* Phys. Rev. Lett. **101**, 215501 (2008).

[22] B. P. Tighe, *Dynamic critical response in damped random spring networks,* Phys. Rev. Lett. **109**, 168303 (2012).

[23] D. A. Head, A. J. Levine, and F. MacKintosh, *Deformation of cross-linked semiflexible polymer networks,* Phys. Rev. Lett. **91**, 108102 (2003).

[24] J. Wilhelm and E. Frey, *Elasticity of stiff polymer networks,* Phys. Rev. Lett. **91**, 108103 (2003).

[25] C. P. Broedersz and F. C. MacKintosh, *Modeling semiflexible polymer networks,* Rev. Mod. Phys. **86**, 995 (2014).

[26] E. Bitzek, P. Koskinen, F. Gähler, M. Moseler, and P. Gumbsch, *Structural relaxation made simple,* Phys. Rev. Lett. **97**, 170201 (2006).

[27] M. S. van Deen, B. P. Tighe, and M. van Hecke, *Contact changes of sheared systems: Scaling, correlations, and mechanisms,* Phys. Rev. E **94**, 062905 (2016).

[28] J. Boschan, D. Vågberg, E. Somfai, and B. P. Tighe, *Beyond linear elasticity: Jammed solids at finite shear strain and rate,* Soft Matter **12**, 5450 (2016).

[29] W. Voigt, *Lehrbuch der kristallphysik (mit ausschluss der kristalloptik)* (Springer-Verlag, 2014).

[30] L. D. Landau and E. M. Lifshitz, *Theory of Elasticity* (Butterworth-Heineman, Oxford, 1997).

[31] C. E. Maloney and A. Lemaître, *Amorphous systems in athermal, qua-sistatic shear,* Phys. Rev. E **74**, 016118 (2006).

[32] G. Guennebaud, B. Jacob, *et al.*, *Eigen v3,* http://eigen.tuxfamily.org (2010).

[33] H. Goldstein, C. Poole, and J. Safko, *Classical mechanics* (Pearson Education, 2002).

[34] R. D. Skeel, *Variable step size destabilizes the störmer/leapfrog/verlet method,* BIT **33**, 172 (1993).

[35] D. Frenkel and B. Smit, *Understanding molecular simulation: from algorithms to applications*, Vol. 1 (Elsevier, 2001).

[36] D. Vågberg, P. Olsson, and S. Teitel, *Glassiness, rigidity, and jam-ming of frictionless soft core disks,* Phys. Rev. E **83**, 031307 (2011).

[37] A. Tanguy, J. P. Wittmer, F. Leonforte, and J.-L. Barrat, *Continuum limit of amorphous elastic bodies: A finite-size study of low-frequency harmonic vibrations,* Phys. Rev. B **66**, 174205 (2002).

[38] R. Maranganti and P. Sharma, *Length scales at which classical elas-ticity breaks down for various materials,* Phys. Rev. Lett. **98**, 195504 (2007).

[39] K. Karimi and C. E. Maloney, *Elasticity of frictionless particles near jamming,* Phys. Rev. E **92**, 022208 (2015).

[40] R. D. Mindlin, *Micro-structure in linear elasticity,* Arch. Rat. Mech. Anal. **16**, 51 (1964).

[41] A. C. Eringen, *On differential equations of nonlocal elasticity and solu-tions of screw dislocation and surface waves,* J. Appl. Phys. **54**, 4703 (1983).

[42] Z. P. Bazant and M. Jirásek, *Nonlocal integral formulations of plastic-ity and damage: survey of progress,* J. Eng. Mech. **128**, 1119 (2002).

[43] H. Askes and E. C. Aifantis, *Gradient elasticity in statics and dy-namics: An overview of formulations, length scale identification proce-dures, finite element implementations and new results,* Int. J. Solids Struct. **48**, 1962 (2011).

[44] O. Pouliquen and N. Renaut, *Onset of granular flows on an inclined rough surface: dilatancy effects,* Journal de Physique II **6**, 923 (1996).

[45] O. Pouliquen, Y. Forterre, and S. Le Dizes, *Slow dense granular flows as a self-induced process,* Adv. Complex Syst. **4**, 441 (2001).

[46] T. S. Komatsu, S. Inagaki, N. Nakagawa, and S. Nasuno, *Creep motion in a granular pile exhibiting steady surface flow,* Phys. Rev. Lett. **86**, 1757 (2001).

[47] I. S. Aranson, L. S. Tsimring, F. Malloggi, and E. Clément, *Nonlocal rheological properties of granular flows near a jamming limit,* Phys. Rev. E **78**, 031303 (2008).

[48] J. Goyon, A. Colin, G. Ovarlez, A. Ajdari, and L. Bocquet, *Spatial cooperativity in soft glassy flows,* Nature **454**, 84 (2008).

[49] O. Pouliquen and Y. Forterre, *A non-local rheology for dense granular flows,* Phil. Trans. Roy. Soc. A **367**, 5091 (2009).

[50] G. Katgert, B. P. Tighe, M. E. Möbius, and M. van Hecke, *Couette flow of two-dimensional foams,* EPL **90**, 54002 (2010).

[51] K. Nichol, A. Zanin, R. Bastien, E. Wandersman, and M. van Hecke, *Flow-induced agitations create a granular fluid,* Phys. Rev. Lett. **104**, 078302 (2010).

[52] M. Bouzid, M. Trulsson, P. Claudin, E. Clément, and B. Andreotti, *Nonlocal rheology of granular flows across yield conditions,* Phys. Rev. Lett. **111**, 238301 (2013).

[53] E. Wandersman and M. Van Hecke, *Nonlocal granular rheology: Role of pressure and anisotropy,* EPL **105**, 24002 (2014).

[54] M. Bouzid, A. Izzet, M. Trulsson, E. Clément, P. Claudin, and B. Andreotti, *Non-local rheology in dense granular flows,* Eur. Phys. J. E **38**, 1 (2015).

[55] P. Kharel and P. Rognon, *The non-local repercussions of partial jamming in glassy and granular flows,* arxiv:1605.00337 (2016).

[56] T. Gueudré, J. Lin, A. Rosso, and M. Wyart, *Scaling description of non-local rheology,* Soft Matter **13**, 3794 (2017).

[57] L. Bocquet, A. Colin, and A. Ajdari, *Kinetic theory of plastic flow in soft glassy materials,* Phys. Rev. Lett. **103**, 036001 (2009).

[58] K. Kamrin and G. Koval, *Nonlocal constitutive relation for steady granular flow,* Phys. Rev. Lett. **108**, 178301 (2012).

[59] D. L. Henann and K. Kamrin, *A predictive, size-dependent continuum model for dense granular flows,* Proc. Natl. Acad. Sci. U.S.A. **110**, 6730 (2013).

[60] M. R. Kuhn, *Are granular materials simple? an experimental study of strain gradient effects and localization,* Mech. Mater. **37**, 607 (2005).

[61] B. Todd, J. Hansen, and P. J. Daivis, *Nonlocal shear stress for homogeneous fluids,* Phys. Rev. Lett. **100**, 195901 (2008).

[62] T. Kawasaki and L. Berthier, *Macroscopic yielding in jammed solids is accompanied by a nonequilibrium first-order transition in particle trajectories,* Phys. Rev. E **94**, 022615 (2016).

[63] D. J. Koeze, D. Vågberg, B. B. Tjoa, and B. P. Tighe, *Mapping the jamming transition of bidisperse mixtures,* EPL **113**, 54001 (2016).

[64] C. F. Schreck, T. Bertrand, C. S. O'Hern, and M. Shattuck, *Repulsive contact interactions make jammed particulate systems inherently nonharmonic,* Phys. Rev. Lett. **107**, 078301 (2011).

[65] C. P. Goodrich, A. J. Liu, and S. R. Nagel, *Finite-size scaling at the jamming transition,* Phys. Rev. Lett. **109**, 095704 (2012).

[66] M. S. van Deen, J. Simon, Z. Zeravcic, S. Dagois-Bohy, B. P. Tighe, and M. van Hecke, *Contact changes near jamming,* Phys. Rev. E **90**, 020202 (2014).

[67] S. S. Schoenholz, C. P. Goodrich, O. Kogan, A. J. Liu, and S. R. Nagel, *Stability of jammed packings II: the transverse length scale,* Soft Matter **9**, 11000 (2013).

[68] E. Somfai, J.-N. Roux, J. H. Snoeijer, M. Van Hecke, and W. Van Saarloos, *Elastic wave propagation in confined granular systems,* Phys. Rev. E **72**, 021301 (2005).

[69] C. P. Goodrich, S. Dagois-Bohy, B. P. Tighe, M. van Hecke, A. J. Liu, and S. R. Nagel, *Jamming in finite systems: Stability, anisotropy, fluctuations, and scaling,* Phys. Rev. E **90**, 022138 (2014).

[70] E. DeGiuli, A. Laversanne-Finot, G. Düring, E. Lerner, and M. Wyart, *Effects of coordination and pressure on sound attenuation, boson peak and elasticity in amorphous solids,* Soft Matter **10**, 5628 (2014).

[71] W. G. Ellenbroek, Z. Zeravcic, W. van Saarloos, and M. van Hecke, *Non-affine response: Jammed packings vs. spring networks,* EPL **87**, 34004 (2009).

[72] K. Karimi and C. E. Maloney, *Local anisotropy in globally isotropic granular packings,* Phys. Rev. Lett. **107**, 268001 (2011).

[73] H. Mizuno, L. E. Silbert, and M. Sperl, *Spatial distributions of local elastic moduli near the jamming transition,* Phys. Rev. Lett. **116**, 068302 (2016).

[74] W. Schirmacher, *Thermal conductivity of glassy materials and the "boson peak,"* EPL **73**, 892 (2006).

[75] P. Olsson and S. Teitel, *Critical scaling of shear viscosity at the jamming transition,* Phys. Rev. Lett. **99**, 178001 (2007).

[76] B. P. Tighe, E. Woldhuis, J. J. C. Remmers, W. van Saarloos, and M. van Hecke, *Model for the scaling of stresses and fluctuations in flows near jamming,* Phys. Rev. Lett. **105**, 088303 (2010).

[77] C. P. Broedersz, X. Mao, T. C. Lubensky, and F. C. MacKintosh, *Criticality and isostaticity in fibre networks,* Nat. Phys. **7**, 983 (2011).

[78] S. Feng and P. N. Sen, *Percolation on elastic networks: new exponent and threshold,* Phys. Rev. Lett. **52**, 216 (1984).

[79] G. Düring, E. Lerner, and M. Wyart, *Phonon gap and localization lengths in floppy materials,* Soft Matter **9**, 146 (2013).

[80] M. Wyart, L. E. Silbert, S. R. Nagel, and T. A. Witten, *Effects of compression on the vibrational modes of marginally jammed solids,* Phys. Rev. E **72**, 051306 (2005).

[81] D. J. Griffiths, *Introduction to quantum mechanics* (Cambridge University Press, 2016).

[82] M. Das, D. Quint, and J. Schwarz, *Redundancy and cooperativity in the mechanics of compositely crosslinked filamentous networks,* PloS One **7**, e35939 (2012).

[83] F. MacKintosh, J. Käs, and P. Janmey, *Elasticity of semiflexible biopolymer networks,* Phys. Rev. Lett. **75**, 4425 (1995).

[84] D. Head, A. Levine, and F. MacKintosh, *Distinct regimes of elastic response and deformation modes of cross-linked cytoskeletal and semiflexible polymer networks,* Phys. Rev. E **68**, 061907 (2003).

[85] G. Pike and C. Seager, *Percolation and conductivity: a computer study. I,* Phys. Rev. B **10**, 1421 (1974).

[86] J. Åström, S. Saarinen, K. Niskanen, and J. Kurkijärvi, *Microscopic mechanics of fiber networks,* J. Appl. Phys. **75**, 2383 (1994).

[87] C. Heussinger and E. Frey, *Stiff polymers, foams, and fiber networks,* Phys. Rev. Lett. **96**, 017802 (2006).

[88] C. Heussinger and E. Frey, *Floppy modes and nonaffine deformations in random fiber networks,* Phys. Rev. Lett. **97**, 105501 (2006).

[89] C. Heussinger, B. Schaefer, and E. Frey, *Nonaffine rubber elasticity for stiff polymer networks,* Phys. Rev. E **76**, 031906 (2007).

[90] W. Thomson, *Elasticity,* in *Encyclopaedia Britannica* (Adam and Charles Black, Edinburgh, 1878).

[91] J. Poynting, *On pressure perpendicular to the shear planes in finite pure shears, and on the lengthening of loaded wires when twisted,* Proc. R. Soc. A **82**, 546 (1909).

[92] O. Reynolds, *On the dilatancy of media composed of rigid particles,* in *Proc. Brit. Assoc.* (1885) p. 896.

[93] J. Ren, J. A. Dijksman, and R. P. Behringer, *Reynolds pressure and relaxation in a sheared granular system,* Phys. Rev. Lett. **110**, 018302 (2013).

[94] P. A. Janmey, M. E. McCormick, S. Rammensee, J. L. Leight, P. C. Georges, and F. C. MacKintosh, *Negative normal stress in semiflexible biopolymer gels,* Nat. Mater. **6**, 48 (2007).

[95] D. Weaire and S. Hutzler, *Dilatancy in liquid foams,* Philos. Mag. **83**, 2747 (2003).

[96] A. R. Cioroianu and C. Storm, *Normal stresses in elastic networks,* Phys. Rev. E **88**, 052601 (2013).

[97] B. P. Tighe, *Shear dilatancy in marginal solids,* Granular Matter **16**, 203 (2014).

[98] F. Meng and E. M. Terentjev, *Nonlinear elasticity of semiflexible filament networks,* Soft Matter **12**, 6749 (2016).

[99] H. C. de Cagny, B. E. Vos, M. Vahabi, N. A. Kurniawan, M. Doi, G. H. Koenderink, F. C. MacKintosh, and D. Bonn, *Porosity governs normal stresses in polymer gels,* Phys. Rev. Lett. **117**, 217802 (2016).

[100] C. Horgan and J. Murphy, *Poynting and reverse poynting effects in soft materials,* Soft Matter **13**, 4916 (2017).

[101] E. Conti and F. C. MacKintosh, *Cross-linked networks of stiff filaments exhibit negative normal stress,* Phys. Rev. Lett. **102**, 088102 (2009).

[102] N. Xu, V. Vitelli, A. J. Liu, and S. R. Nagel, *Anharmonic and quasi-localized vibrations in jammed solids—modes for mechanical failure,* EPL **90**, 56001 (2010).

[103] S. Feng, M. Thorpe, and E. Garboczi, *Effective-medium theory of percolation on central-force elastic networks,* Phys. Rev. B **31**, 276 (1985).

[104] D. J. Jacobs and M. F. Thorpe, *Generic rigidity percolation in two dimensions,* Phys. Rev. E **53**, 3682 (1996).

[105] B. P. Tighe and J. E. S. Socolar, *Nonlinear elastic stress response in granular packings,* Phys. Rev. E **77**, 031303 (2008).

[106] M. Sheinman, C. P. Broedersz, and F. C. MacKintosh, *Nonlinear effective-medium theory of disordered spring networks,* Phys. Rev. E **85**, 021801 (2012).

[107] C. Buss, C. Heussinger, and O. Hallatschek, *Thermalized connectivity networks of jammed packings,* Soft Matter **12**, 7682 (2016).

[108] C. S. O'Hern, L. E. Silbert, A. J. Liu, and S. R. Nagel, *Reply to "comment on 'jamming at zero temperature and zero applied stress: The epitome of disorder'",* Phys. Rev. E **70**, 043302 (2004).

[109] K. Baumgarten, D. Vågberg, and B. P. Tighe, *Nonlocal elasticity near jamming in frictionless soft spheres,* Phys. Rev. Lett. **118**, 098001 (2017).

[110] K. Baumgarten and B. P. Tighe, *Viscous forces and bulk viscoelasticity near jamming,* Soft Matter **13**, 8368 (2017).

[111] S. Alexander, *Amorphous solids: their structure, lattice dynamics and elasticity,* Phys. Rep. **296**, 65 (1998).

[112] S. Dagois-Bohy, E. Somfai, B. P. Tighe, and M. van Hecke, *Softening and yielding of soft glassy materials,* Soft Matter **13**, 9036 (2017).

[113] M. Vahabi, B. E. Vos, H. C. de Cagny, D. Bonn, G. H. Koenderink, and F. MacKintosh, *Normal stresses in semiflexible polymer hydrogels,* Phys. Rev. E **97**, 032418 (2018).

[114] J. A. Åström, J. P. Mäkinen, M. J. Alava, and J. Timonen, *Elasticity of poissonian fiber networks,* Phys. Rev. E **61**, 5550 (2000).

[115] C. P. Goodrich, A. J. Liu, and S. R. Nagel, *The principle of independent bond-level response: Tuning by pruning to exploit disorder for global behavior,* Phys. Rev. Lett. **114**, 225501 (2015).

[116] D. R. Reid, N. Pashine, J. M. Wozniak, H. M. Jaeger, A. J. Liu, S. R. Nagel, and J. J. de Pablo, *Auxetic metamaterials from disordered networks,* Proc. Natl. Acad. Sci. U.S.A. , 201717442 (2018).

[117] S. Tewari, D. Schiemann, D. J. Durian, C. M. Knobler, S. A. Langer, and A. J. Liu, *Statistics of shear-induced rearrangements in a two-dimensional model foam,* Phys. Rev. E **60**, 4385 (1999).

[118] V. Langlois, S. Hutzler, and D. Weaire, *Rheological properties of the soft-disk model of two-dimensional foams,* Phys. Rev. E **78**, 021401 (2008).

[119] T. Hatano, *Growing length and time scales in a suspension of athermal particles,* Phys. Rev. E **79**, 050301 (2009).

[120] J. Boschan, S. Vasudavan, P. E. Boukany, E. Somfai, and B. P. Tighe, *Stress relaxation in viscous soft spheres,* Soft Matter **13**, 6870 (2017).

[121] F. Bolton and D. Weaire, *Rigidity loss transition in a disordered 2d froth,* Phys. Rev. Lett. **65**, 3449 (1990).

[122] K. Khakalo, K. Baumgarten, B. P. Tighe, and A. Puisto, *Coarsening and mechanics in the bubble model for wet foams,* Phys. Rev. E **98**, 012607 (2018).

[123] H. A. Barnes and J. F. Hutton, *An Introduction to Rheology* (Elsevier, 1989).

[124] S. Cohen-Addad, H. Hoballah, and R. Höhler, *Viscoelastic response of a coarsening foam,* Phys. Rev. E **57**, 6897 (1998).

[125] A. D. Gopal and D. J. Durian, *Relaxing in foam,* Phys. Rev. Lett. **91**, 188303 (2003).

[126] J. M. Kropka and M. Celina, *Viscoelasticity of liquid organic foam: Relaxations, temporal dependence, and bubble loading effects on flow behavior,* J. Chem. Phys. **133**, 024904 (2010).

[127] J. J. Liétor-Santos, B. Sierra-Martín, and A. Fernández-Nieves, *Bulk and shear moduli of compressed microgel suspensions,* Phys. Rev. E **84**, 060402 (2011).

[128] I. Srivastava and T. S. Fisher, *Slow creep in soft granular packings,* Soft Matter **13**, 3411 (2017).

[129] F. P. Bretherton, *The motion of long bubbles in tubes,* J. Fluid Mech. **10**, 166 (1961).

[130] N. Denkov, S. Tcholakova, K. Golemanov, K. Ananthapadmanabhan, and A. Lips, *Viscous friction in foams and concentrated emulsions under steady shear,* Phys. Rev. Lett. **100**, 138301 (2008).

[131] J. R. Seth, L. Mohan, C. Locatelli-Champagne, M. Cloitre, and R. T. Bonnecaze, *A micromechanical model to predict the flow of soft particle glasses,* Nat. Mater. **10**, 838 (2011).

[132] B. Andreotti, J.-L. Barrat, and C. Heussinger, *Shear flow of non-brownian suspensions close to jamming,* Phys. Rev. Lett. **109**, 105901 (2012).

[133] B. I. Halperin and P. C. Hohenberg, *Scaling laws for dynamic critical phenomena,* Phys. Rev. **177**, 952 (1969).

[134] D. Morse and T. Witten, *Droplet elasticity in weakly compressed emulsions,* EPL **22**, 549 (1993).

[135] M.-D. Lacasse, G. S. Grest, and D. Levine, *Deformation of small compressed droplets,* Phys. Rev. E **54**, 5436 (1996).

[136] B. P. Tighe, *Handbook of granular materials,* (CRC Press, 2016) Chap. Wet Foams, Slippery Grains.

[137] S. Hutzler, R. P. Murtagh, D. Whyte, S. T. Tobin, and D. Weaire, *Z-cone model for the energy of an ordered foam,* Soft Matter **10**, 7103 (2014).

[138] R. Höhler and S. Cohen-Addad, *Many-body interactions in soft jammed materials,* Soft matter **13**, 1371 (2017).

[139] J. Winkelmann, F. Dunne, V. Langlois, M. Möbius, D. Weaire, and S. Hutzler, *2d foams above the jamming transition: Deformation matters,* Colloids Surf. A **534**, 52 (2017).

[140] C. E. Maloney and M. O. Robbins, *Evolution of displacements and strains in sheared amorphous solids,* J. Phys.: Condens. Matter **20**, 244128 (2008).

[141] D. Vagberg and B. P. Tighe, *On the apparent yield stress in non-brownian magnetorheological fluids,* Soft Matter **13**, 7207 (2017).

[142] P.-E. Peyneau and J.-N. Roux, *Frictionless bead packs have macroscopic friction, but no dilatancy,* Phys. Rev. E **78**, 011307 (2008).

[143] T. Hatano, *Scaling properties of granular rheology near the jamming transition,* J. Phys. Soc. Jpn. **77**, 123002 (2008).

[144] M. Otsuki and H. Hayakawa, *Critical behaviors of sheared frictionless granular materials near the jamming transition,* Phys. Rev. E **80**, 011308 (2009).

[145] C. Heussinger, P. Chaudhuri, and J.-L. Barrat, *Fluctuations and correlations during the shear flow of elastic particles near the jamming transition,* Soft Matter **6** (2010).

[146] D. J. Evans and G. Morriss, *Statistical Mechanics of Nonequilibrium Liquids* (Cambridge University Press, 2008).

[147] A. Ikeda, L. Berthier, and P. Sollich, *Unified study of glass and jamming rheology in soft particle systems,* Phys. Rev. Lett. **109**, 018301 (2012).

[148] E. Lerner, G. Düring, and M. Wyart, *A unified framework for non-brownian suspension flows and soft amorphous solids,* Proc. Natl. Acad. Sci. U.S.A. **109**, 4798 (2012).

[149] G. Katgert, M. E. Möbius, and M. van Hecke, *Rate dependence and role of disorder in linearly sheared two-dimensional foams,* Phys. Rev. Lett. **101**, 058301 (2008).

[150] B. A. DiDonna and T. C. Lubensky, *Nonaffine correlations in random elastic media,* Phys. Rev. E **72**, 066619 (2005).

[151] B. P. Tighe, J. H. Snoeijer, T. J. H. Vlugt, and M. van Hecke, *The force network ensemble for granular packings,* Soft Matter **6**, 2908 (2010).

[152] B. P. Tighe and T. J. H. Vlugt, *Stress fluctuations in granular force networks,* J. Stat. Mech.: Theory Exp. , P04002 (2011).

[153] C. Maloney, *Correlations in the elastic response of dense random packings,* Phys. Rev. Lett. **97**, 035503 (2006).

[154] G. Katgert, A. Latka, M. E. Möbius, and M. van Hecke, *Flow in linearly sheared two-dimensional foams: From bubble to bulk scale,* Phys. Rev. E **79**, 066318 (2009).

[155] M. Le Merrer, R. Lespiat, R. Hohler, and S. Cohen-Addad, *Linear and non-linear wall friction of wet foams,* Soft Matter **11**, 368 (2015).

Acknowledgements

Doing a PhD for four years comes with many challenges which are not all technical. It can often be hard to stay confident that all these little things which one is doing actually add up to a good thesis. It is hard to keep the big picture of the thesis in mind and manage everything and not get lost on the way. And of course, on top of that it is important to stay motivated and positive about what one is doing. All those people who helped me with these things I would like to thank here.

I just start with my Co-Promotor and daily supervisor Brian Tighe and my Promotor Thijs Vlugt without whom the project would not even have started. Thank you Thijs and Brian for giving me the opportunity to work in the Engineering Thermodynamics group. Brian I would like to regard with special thanks here. Over the course of those four years of my PhD I never had the feeling being left alone without help in case I needed it. I believe we formed a good team with an honest and straight forward way of communicating which made our work productive. In turn we were rewarded with a few good papers in nice journals.

I would also like to thank people who were not directly involved in my project. I had a great time in Delft and having nice friends around makes live much easier. Of course without them I would not have finished my thesis.

Weiwei, Wenli, Jan, Sebastian, Marloes, Metin, Vilborg, Mohammad, Vincent, Uttiya, Nikos, Noura, Rishab, Gustavo, Stephan, Mira, Nanouk, Simone, Ahmadreza, Rumen, Johan, Jannick, Bastian, Anja, Benno, Leut, Rike, Fabian, Imke, Joscha, Jessi.

Und natürlich ein ganz besonderes Danke an meine Eltern und Geschwister. Auch wenn natürlich nicht unmittelbar, habt ihr aber doch auch euren Teil dazu beigetragen, dass ich nun diese Arbeit hier abschließe. Natürlich nervt ihr mich manchmal und ich nerve auch euch. Aber doch bin ich immer glücklich mal wieder nach Hause zu kommen oder mit euch zu skypen. Es ist gut zu wissen, dass ich ihr da seid.

Curriculum Vitæ

Karsten BAUMGARTEN

08-07-1988   Born in Einbeck, Germany.

Education

2001–2008   Gymnasium
             Gymnasium Corvinianum
             Northeim, Germany

2008–2011   Bachelor of Science in Physics
             Georg-August-University Göttingen

2011–2013   Master of Science in Physics
             Georg-August-University Göttingen

2014–2019   PhD
             Delft University of Technology
             Thesis: Mechanics of Marginal Solids:
                              Length, Strain, and Time Scales
             Promotor: Prof. dr. T. J. H. Vlugt
             Copromotor: Dr. B. P. Tighe

List of Publications

1. **Karsten Baumgarten, Daniel Vågberg, and Brian P. Tighe**,
   Nonlocal Elasticity near Jamming in Frictionless Soft Spheres,
   Phys. Rev. Lett. 118, 098001 (2017).

2. **Karsten Baumgarten and Brian P. Tighe**,
   Viscous forces and bulk viscoelasticity near jamming ,
   Soft Matter, 2017,13, 8368-8378.

3. **Karsten Baumgarten and Brian P. Tighe**,
   Normal Stresses, Contraction, and Stiffening in Sheared Elastic Networks,
   Phys. Rev. Lett. 120, 148004 (2018).

4. **Kseniia Khakalo, Karsten Baumgarten, Brian P. Tighe, and Antti Puisto**,
   Coarsening and mechanics in the bubble model for wet foams,
   Phys. Rev. E 98, 012607 (2018).

5. **Karsten Baumgarten, Dion J. Koeze, Zihan Tan, René Pečnik, and Brian P. Tighe**,
   Rigidity in Hypostatic Networks,
   In preparation.

6. **Matthias Merkel, Karsten Baumgarten, Brian P. Tighe, and Lisa Manning**,
   A minimal-length approach unifies rigidity in under-constrained materials,
   Accepted for publication in PNAS.